LASER GENERATED PLASMA TORCH INJECTORS FOR BEAM-DRIVEN PLASMA WAKEFIELD ACCELERATORS

by

DANIEL ULLMANN

A thesis presented for the degree of
Doctor of Philosophy in Physics

University of Strathclyde

Department of Physics

2021

SUPERVISORS:
Bernhard Hidding
Dino Jaroszynski

DECLARATION

This thesis is the result of the author's original research. It has been composed by the author and has not been previously submitted for examination which has led to the award of a degree.

Signed: Daniel Ullmann
Date: April 11, 2021

Did ye aye?

— Scottish patter —

ABSTRACT

The demand for high-quality relativistic electron beams continuously grows due to socio-economic applications, most of which have been enabled by radio-frequency accelerators in the first place. However, further development of this matured technology implies an unsustainably growing footprint of these machines and therefore causes immense costs and limited availability of such facilities. At the same time, conventional accelerators may have reached the ceiling of their capabilities, e.g. in terms of achievable electron beam quality. Novel accelerator schemes are therefore needed.

Beam-driven plasma wakefield accelerators (PWFAs) offer the necessary environment for a conceptual change by providing much stronger and phase-constant acceleration compared to their conventional counterparts. Employing plasma takes advantage of an indestructible medium that offers flexible design via its fundamental property – the plasma density.

While intense R&D has fostered a clearer understanding of plasma wakefields in the past decades, challenges remain to be mastered before PWFAs reach the status of a matured technology that is ready to drive next-generation applications. These typically necessitate electron sources producing high-quality beams in a reliable fashion, which are both attributes that are dominated by the employed mechanism for electron injection. Reshaping the plasma density by hydrodynamic density downramp injectors has been shown to facilitate controlled injection in laser-driven wakefield accelerators, but proves elusive in PWFA.

However, injection is readily achievable with the plasma torch injector, an all-optical density downramp scheme that has enabled controlled injection in PWFA experiments for the first time. It relies on the superposition of laser-generated plasma rather than hydrodynamic reorganisation of gas media and offers the capability for 3D shaping of density distributions. In this context, results from the first experimental implementation of this technique at SLAC FACET are studied by extensive particle-in-cell simulations (PIC) revealing the involved dynamics in addition to strategies for further improving the injector's resilience to operational instabilities.

Combining experimental observations and simulations, a phenomenological model is derived that quantifies the charge of injected electron populations based on the geometry and distribution of the wakefields and plasma torch. This approach opens new perspectives on downramp physics and may facilitate the design and optimisation of downramp injectors while avoiding computationally costly PIC simulations.

Based on the congruence of the experiment, model and numerical investigations, further PIC studies are carried out to examine two extreme cases of plasma torch injection. For

plasma torches wider than the wakefields, conventional downramp physics are recovered and high-quality electron beams are obtained rivalling the state-of-the-art of conventional linear accelerators and even offer the potential to supersede those. In contrast to the various gas density downramp injection schemes, the plasma torch additionally enables injection from density spikes much narrower than the plasma accelerator. This paves the way for new regimes of electron generation, such as counter-oscillating twin-beamlets – structures that have not been observed before in wakefield accelerators. This lays the foundation for novel modalities, which bear particular potential for controlled generation of highly polarised x-rays.

ACKNOWLEDGMENTS

The past four years have been a great experience, which was only possible due to the support I received from many people in different aspects. I have felt very fortunate to meet so many like-minded people at Strathclyde and in Glasgow, all of whom shaped me as a person and as a researcher.

I would like to pay my special regards to Bernhard Hidding for mentoring and supporting me throughout the past years. His creativity was an invaluable contributor boosting my advancement as a scientist, whether in the institute or in the pub.

Many thanks to Dino A. Jaroszynski for his co-supervision and the interesting discussions during vivas.

I wish to show my gratitude to Matt Zepf, who supported my professional development before and after my time in Glasgow.

Special thanks to the Central Laser Facility for funding my course and giving me the opportunity to study at the University of Strathclyde.

I would like to thank Oliver S. Karger and Alexander Knetsch for designing and performing large parts of the E-210 campaign, and for providing the obtained results.

Special thanks to Thomas Heinemann for introducing me to the wonders of PIC simulations and the help in modelling the FACET experiments.

Many thanks to Andrew Beaton for the shared suffering during the E-210 simulation campaign.

Particular thanks to Paul Scherkl for the support on the plasma torch paper and the many lessons on scientific writing.

Thanks also to Andrew Sutherland and A. Fahim Habib for the many discussions during working hours and leisure time.

To all the people I have had the pleasure to meet in Glasgow that are not mentioned by name: Ta!

Finally, I am more grateful than I can possibly say, to Kristina and my family. Your unwavering support during my time abroad and encouragement in all my pursuits was immeasurable. Thank you.

PUBLICATIONS

The author has produced or contributed to the following publications during this study:

[1] R. W. Assmann et al. "EuPRAXIA Conceptual Design Report." In: *The European Physical Journal Special Topics* 229.24 (2020). DOI: 10.1140/epjst/e2020-000127-8.

[2] A. Deng et al. "Generation and acceleration of electron bunches from a plasma photocathode." In: *Nature Physics* (2019). DOI: 10.1038/s41567-019-0610-9.

[3] A. F. Habib et al. "Plasma accelerator-based ultrabright x-ray beams from ultrabright electron beams." In: *Proceedings SPIE* (2019). DOI: 10.1117/12.2530976.

[4] B. Hidding et al. "First measurements of Trojan Horse injection in a plasma wakefield accelerator." In: *Proceedings of IPAC2017* (2017). URL: http://accelconf.web.cern.ch/AccelConf/ipac2017/papers/tuyb1.pdf.

[5] B. Hidding et al. "Fundamentals and Applications of Hybrid LWFA-PWFA." In: *Applied Sciences* (2019). DOI: 10.3390/app9132626.

[6] G. G. Manahan et al. "Advanced schemes for underdense plasma photocathode wakefield accelerators: pathways towards ultrahigh brightness electron beams." In: *Philosophical Transactions of the Royal Society A* (2019). DOI: 10.1098/rsta.2018.0182.

[7] P. Scherkl et al. "Plasma-photonic spatiotemporal synchronization of relativistic electron and laser beams." In: *arXiv:1908.09263* (2019). URL: http://arxiv.org/abs/1908.09263..

[8] M. B. Schwab et al. "Visualization of relativistic laser pulses in underdense plasma." In: *Physical Review Accelerators and Beams* (2020). DOI: 10.1103/PhysRevAccelBeams.23.032801.

[9] D. Ullmann et al. "All-optical density downramp injection in electron-driven plasma wakefield accelerators." In: *arXiv:2007.12634* (2020). URL: https://arxiv.org/abs/2007.12634.

CONTENTS

LIST OF FIGURES

LIST OF TABLES

ACRONYMS

PIC Particle-In-Cell

PWFA particle-driven plasma wakefield accelerator

LWFA laser-driven plasma wakefield accelerator

L2PWFA laser-to-particle-driven plasma wakefield accelerator [75, 115]

SLAC Stanford Linear Accelerator Center

FACET Facilities for Accelerator science and Experimental Test beams [78], SLAC

FACET II Facility for Advanced Accelerator Experimental Tests [191], SLAC

ADK Ammosov-Delone-Krainov [4], cf. Section 3.2

FEL free-electron laser

VSim PIC code based on the VORPAL engine [126]

linac linear accelerator

1 INTRODUCTION

1.1 PARTICLE ACCELERATORS

Particle accelerators are indispensable tools to explore the universe. Since their inception more than 100 years ago, these machines have been driving fundamental research in nuclear and high-energy physics. Highlights include breakthrough discoveries such as the detection of the electron [172], or the Higgs boson [26] and contributes to Nobel prize-winning research every 2.9 years [73]. However, particle accelerators are not limited to fundamental research. In fact, the majority of machines contributes to various fields benefitting society outside the context of fundamental science [55]. Particularly important applications include medical imaging [189], radiation therapy [121], ion implantation in semiconductors and other material sciences [9].

In recent years, there has been growing interest in particle beams as drivers of the fourth-generation light sources such as FELs [51], which allow for production of ultra-short radiation pulses with immense brightness and coherence [185]. These properties unlock observations on unprecedented scales such as molecular dynamics, which fosters the understanding of microscopic processes in chemistry and biology.

However, generating particle beams suitable for such light sources by conventional accelerators reached a ceiling as result of their underlying principles and limitations. For instance, high electric fields generate hot spots that ionise the accelerator hardware and therefore confines the accelerating field strength to the order of 100 MV/m [70]. Obtaining high particle energies hence demands for long acceleration lengths as illustrated by SLACs linear accelerator of 3.2 km length, which is now part of LCLS II [163] and FACET II [191], or the Large Hadron Collider of 27 km circumference at CERN. The size of these devices determines their cost of installation and maintenance, which adds a financial limit to the immense spatial footprint. These restrictions strongly limit the number of high energy particle accelerators, thus limiting the pace of scientific progress. It is therefore vital to satisfy the continuously growing need for particle accelerators in addition to exploring the opportunities arising from the development of new accelerator schemes.

Plasma wakefield accelerators overcome the challenge of material breakdown by utilising plasma to form the accelerator. Taking advantage of the already ionised material unlocks particularly strong acceleration of electrons by harnessing the fields in laser- or beam-driven plasma waves, which provide orders of magnitude stronger electric fields compared to their conventional counterparts. This facilitates dramatically reduced acceleration lengths and paves the way for miniaturisation and democratisation of particle accelerators.

In order to employ plasma waves as electron accelerators, however, particles have to be injected into the wakefield. This process determines the quality of the resulting electron bunches and has therefore been receiving enormous attention in recent R&D. Gasdynamic reorganisation of the plasma has accomplished controlled and localised density downramp injection for laser-driven wakefield accelerators (LWFAs). However, it proves elusive for beam-driven wakefield accelerators (PWFAs).

The present thesis investigates a scheme that readily facilitates injection by replacing hardware modules that are typically used for gasdynamic downramp generation, by plasma. This is achieved by the plasma torch injector, which relies on the controlled superposition of laser-generated plasma components. It allows for 3D shaping of the injector de-coupled from the accelerator component of the PWFA and offers opportunities to manipulate the injected electron bunch in unprecedented ways.

1.2 THESIS OUTLINE

The presented work is divided into four parts. Part I accounts for the multidisciplinary character of wakefield accelerators and covers relevant theoretical foundations of laser and plasma physics and discusses PWFAs as well as established injection mechanisms. A brief introduction of the particle-in-cell method concludes this chapter.

Results from the E-210 experimental campaign at SLAC FACET and corresponding numerical investigations are discussed in Part II, with particular emphasis on the plasma torch injector.

Part III presents a detailed numerical study of plasma torch injection and serves as guidance for the approved E-311 experimental campaign at SLAC FACET II.

This work is summarised and an outlook is given in Part IV.

1.3 ROLE OF THE AUTHOR

The numerical simulations presented in this thesis comprise the long-term development and the numerical understanding acquired by many members of the research group. The author's work and the contribution of others is listed below.

Results presented in Part II relate to the E-210 experimental campaign at SLAC FACET. O. S. Karger and A. Knetsch designed and performed large parts of the experiment and provided the experimental results, which are shown in Fig. 8.7 after further analysis by the author. The author joined the E-210 team after completion of the experiments in October 2016, which marked the initial phase of the PIC modelling of the campaign. T. Heinemann designed the simulation backbone and performed the initial run of the FACET beam through the plasma channel, which is discussed in the beginning of Section 8.6. This simulation was then modified by the author for studying the plasma torch injector, which has been partially integrated in [44]. Figures 8.1 and 8.5 are modified versions from

this publication. The author has made conceptual contributions to the plasma afterglow technique [153].

Simulations in Part III are based on the design by P. Scherkl and A. F. Habib and were further developed by the author to model the plasma torch injector. The contents of this chapter have been published in [175], whereas simulations shown in Figs. 9.2, 9.3 and 9.5 to 9.7 were conducted by P. Scherkl for this publication.

Part I

THEORETICAL FOUNDATIONS

Plasma wakefield accelerators (PWFAs) represent a multidisciplinary branch of science, which comprises laser, plasma and accelerator science. In the following, the theoretical foundations of the most relevant aspects of these research disciplines for plasma wakefield injection and acceleration are presented and discussed.

The first chapter introduces the basic concepts of laser physics. Then, basic principles of plasma physics and optical generation of plasmas are outlined to set the relevant background for this work. The next chapter sketches the most important concepts of charged particle beams, which is vital for characterising both, beams that excite the plasma wave and those that are accelerated by it. Combining the knowledge of these two chapters then allows for studying the basic features of plasma wake excitation and subsequent trapping of particle beams in these wakes. Part I concludes with an overview on methods used in this work.

2

LASER BEAMS

Lasers are tools in countless scientific disciplines, industry and are an integral part in everyday life applications. With the inception of the CHIRPED PULSE AMPLIFICATION (CPA) scheme [105, 164], ever-increasing laser powers became available allowing for ultra-intense field strengths. This technology was an enabling building block for various national and international research facilities and even many university-scale laboratories. The following pages describe basic laser properties relevant for this work following [45, 60, 124, 168, 180].

2.1 PROPAGATION OF LASER PULSES IN VACUUM

The fundamental equations describing electric fields $\vec{E}(\vec{r}, t)$ and magnetic fields $\vec{B}(\vec{r}, t)$ of laser pulses are the MAXWELL EQUATIONS [82]

$$\text{Gauss's law}: \quad \vec{\nabla}\vec{E} = -\frac{\rho}{\epsilon_0}, \tag{2.1}$$

$$\vec{\nabla}\vec{B} = 0, \tag{2.2}$$

$$\text{Faraday's law}: \quad \vec{\nabla} \times \vec{E} = -\frac{\partial \vec{B}}{\partial t}, \tag{2.3}$$

$$\text{Ampere's law}: \quad \vec{\nabla} \times \vec{B} = \mu_0 \vec{j} + \epsilon_0 \mu_0 \frac{\partial \vec{E}}{\partial t}. \tag{2.4}$$

with the electric permittivity ε_0 and the magnetic permeability μ_0 in vacuum, which relate to the vacuum speed of light $c = 1/\sqrt{\varepsilon_0 \mu_0}$. This set of equations further depends on the charge densities $\rho(\vec{r}, t)$ and current densities $\vec{j}(\vec{r}, t)$. In the absence of these source terms, however, $\nabla\times$ Eq. (2.3) and Eq. (2.4) can be combined to obtain the ELECTROMAGNETIC WAVE EQUATION

$$\Delta\vec{E} - \frac{1}{c^2}\frac{\partial^2 \vec{E}}{\partial t^2} = 0. \tag{2.5}$$

Defining the propagation direction in z and the linear polarisation in x-direction, this equation can be simplified by assuming that the electric field is composed of a SLOWLY-VARYING ENVELOPE $u(\vec{r}, t)$ and a plane wave that oscillates with the laser frequency ω_L and the laser's wave vector k_L [180]

$$\vec{E} = E_{L,0}\vec{e}_x u \exp(i\omega_L t - ik_L z). \tag{2.6}$$

Further assuming paraxial propagation [168], i.e. small divergence of the beam $|\partial^2 u/\partial z^2| \ll 2k_L|\partial u/\partial z|$, yields the PARAXIAL HELMHOLTZ EQUATION

$$\frac{\partial^2 u}{\partial x^2} + \frac{\partial^2 u}{\partial y^2} - 2ik_L \frac{\partial u}{\partial z} = 0. \tag{2.7}$$

This equation features solutions for Laguerre and Hermite modes. However, both assume the same fundamental mode that is commonly used to describe Gaussian laser pulses [181]

$$\begin{aligned}\vec{E}_L = E_{L,0}\vec{e}_x \frac{w_0}{w(z)} \exp\left(\frac{-r^2}{w(z)^2}\right) \exp\left(-4\log(2)\frac{(z/c-t)^2}{\tau^2}\right) \times \\ \cos\left(\omega_L t - k_L z - k_L \frac{r^2}{2\Omega(z)} + \varphi_G(z)\right).\end{aligned} \tag{2.8}$$

The first line of Eq. (2.8) characterises the envelope of the pulse. Its longitudinal part incorporates the full width at half maximum (FWHM) pulse duration that converts to the r.m.s. pulse width σ_T as $\tau = 2\sqrt{2\log(2)}\sigma_T$. Note, that the FWHM of the intensity τ_I is another common definition of the pulse duration, which equals $\tau_I = \tau/\sqrt{2}$. The transverse behaviour of the envelope depends on the BEAM WAIST

$$w = w_0\sqrt{1 + \frac{z^2}{z_R^2}}, \tag{2.9}$$

and the RAYLEIGH RANGE

$$z_R = \frac{\pi w_0^2}{\lambda_L}. \tag{2.10}$$

Here, the spot size w_0 denotes the smallest transverse extent of the beam and z_R characterises the propagation distance over which the beam increases its spot size to $\sqrt{2}w_0$. For commonly used Ti:sapphire lasers $\lambda_L \approx 800\,\text{nm}$, for example, focusing to $w_0 = 20\,\mu\text{m}$ results in a Rayleigh range of $z_R \approx 1.6\,\text{mm}$. $w(z)$ and z_R are visualised in Fig. 2.1 a) as black lines and grey shades, respectively. The second line in Eq. (2.8) quantifies the phase of the laser pulse and includes the curvature of the wave fronts $\Omega = z + z_R^2/z$ and the Gouy phase term $\varphi_G = \arctan(z/z_R)$. The full distribution of Eq. (2.8) is shown in Fig. 2.1 a) at three different times t, i.e. illustrating the laser pulse converging at $z \approx -2\,z_R$, in focus at $z = 0$ and diverging at $z \approx 2\,z_R$. The field distribution through Eq. (2.8) at $r = 0$ and the corresponding envelope are further illustrated in Fig. 2.1 b). Approximating laser pulses by their envelope is a common technique to simplify calculations, e.g. in cycle averaged tunnelling rates for ionisation (see Section 3.2), or for reducing computational costs in PIC simulations (see Section 7.1).

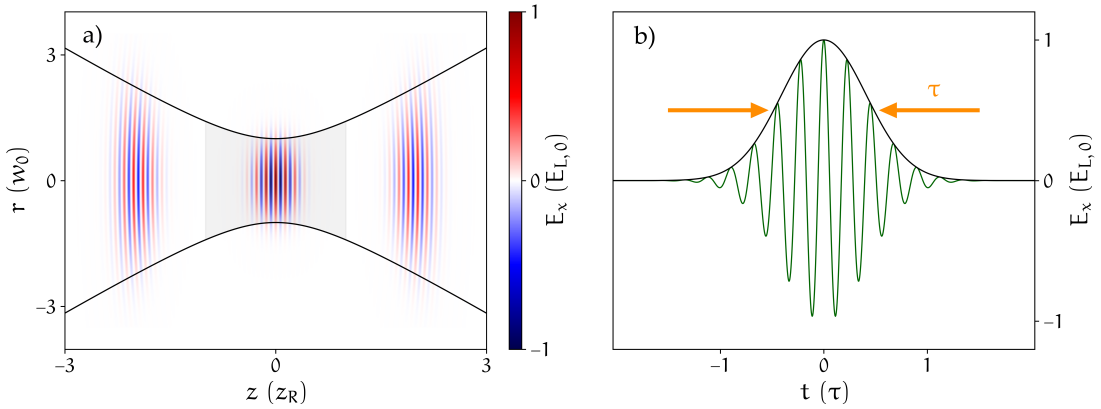

Figure 2.1: Gaussian laser beams. a), Gaussian laser propagation at three different times. The black lines visualise the evolution of the beam waist $w(z)$, whereas grey shades indicate the interval $-z_R \leqslant z \leqslant z_R$. b), temporal profile of the focused Gauss beam shown in a) (green) and its envelope (black). Arrows mark the full width at half maximum pulse duration τ of the electric field.

The electric field of Gaussian laser pulses relates to the laser intensity [124]

$$I_L = \frac{\varepsilon_0 c}{2}|E_L|^2, \tag{2.11}$$

and the total pulse energy [181]

$$\varepsilon_L = (\pi/2)^{3/2}\,\varepsilon_0 c \sigma_T w_0^2 E_{L,0}^2. \tag{2.12}$$

Current high-power laser systems based on Ti:sapphire technology readily achieve $\varepsilon_L \approx 10\,\mathrm{J}$ energies in $\tau \approx 20\,\mathrm{fs}$ providing peak intensities in excess of $10^{19}\,W/cm^2$ [181]. However, this thesis is mainly concerned with moderate laser parameters to achieve the controlled generation of cold plasma via tunnelling ionisation (see Section 3.3). In this case, mJ-class laser pulses with peak intensities of $10^{15}\,W/cm^3$ are desired to achieve low values of the NORMALISED VECTOR POTENTIAL [60]

$$a_0 = \frac{eE_{L,0}}{m_e c \omega_L}. \tag{2.13}$$

For $a_0 \ll 1$ we can write the ponderomotive potential as

$$U_p = m_e c^2 \frac{a_0^2}{4}. \tag{2.14}$$

Equations (2.13) and (2.14) can be derived from the interaction of a classical electron of mass m_e and charge e with a plane wave and characterise the electron's cycle-averaged quiver velocity $v_q = a_0 c$. The normalised vector potential a_0 represents a common figure that quantifies the degree of relativistic effects for laser-matter interactions and can be divided into two regimes. For $a_0 \geqslant 1$, the interactions are highly relativistic, such as

in the bubble regime of laser-driven wakefield accelerators [140]. Conversely, $a_0 \ll 1$ denotes the purely classical interplay of the laser with matter. For instance, this implies negligible momentum transfer to photo electrons in the tunnelling regime, which enables the generation of cold, localised plasma as discussed in Section 3.3.

3

PLASMA PHYSICS

Plasma is a state of matter with spatial scales and temperatures ranging over many orders of magnitude. For instance, it covers enormous spatial scales in solar plasmas and microscopic scales in laser-plasmas which occur on the order of μm. Similarly, plasma temperatures can reach thousands of eV in stellar environments, or few eV, e.g. in plasma generated via tunnelling ionisation. The universality of this branch of physics hence requires some guiding principles, which are discussed in this chapter following [27, 82, 161]. The physical laws are evaluated based on numerical examples shown in Table 3.1, which reflect typical plasma properties from optical field ionisation (see Sections 3.2 and 3.3) as commonly employed in PWFAs.

Table 3.1: Typical plasma properties in PWFAs.

plasma electron density	$n_e \approx 10^{23}\ m^{-3}$
plasma electron temperature	$T_e \approx 10\,eV$

3.1 FUNDAMENTALS OF PLASMA PHYSICS

A plasma is defined as QUASI-NEUTRAL mixture of charged and neutral particles, which exhibit COLLECTIVE behaviour [27]. This is often confused with ionised gas, which is not entirely accurate. For instance, ionised gas is not obliged to be quasi-neutral, which refers to plasma screening and implies that Coulomb interactions of the plasma constituents vanish outside a certain range. This range can be quantified by considering a singly ionised plasma formed of a static ion background of number density $n_i = n_0$ and the density of mobile electrons, which follows a Maxwell-Boltzmann distribution $n_e = -n_0 \exp\left(-\frac{e\phi_D(\vec{r})}{k_B T_e}\right)$. Here,$k_B$, T_e and ϕ_D denote the Boltzmann constant, temperature of the plasma electrons and the electrostatic potential, respectively. Studying the plasma's response to a test electron that is located at the co-ordinate origin with $n_t = \delta(\vec{r})$ yields the Poisson equation [82]

$$-\frac{\epsilon_0}{e}\Delta\phi_D = \underbrace{\delta(\vec{r})}_{\text{electron}} + \underbrace{n_0 - n_0 \exp\left(\frac{e\phi_D(\vec{r})}{k_B T_e}\right)}_{\text{plasma}}. \tag{3.1}$$

Assuming dominance of thermal effects $k_B T_e \gg e\phi_D(\vec{r})$, the solution is $\phi_D(\vec{r}) = \phi_C(\vec{r}) \exp(-|\vec{r}|/\lambda_D)$, which includes the Coulomb potential $\phi_C(\vec{r}) = \frac{-1}{4\pi\epsilon_0}\frac{e}{|\vec{r}|}$ and the DEBYE LENGTH

$$\lambda_D = \sqrt{\frac{\epsilon_0 k_B T_e}{n_0 e^2}}. \tag{3.2}$$

The radial symmetry of ϕ_D suggests introducing a sphere of radius λ_D surrounding the excess charge n_t. This Debye sphere then defines different plasma regions: inside the sphere, Coulomb interactions are the governing processes. In regions $r \approx \lambda_D$, plasma electrons accumulate and shield the potential ϕ_D, such that it vanishes for $r \gg \lambda_D$. The Debye length hence determines the range over which perturbations are shielded in plasmas, such that it appears to be neutral outside of these regions. The numerical example through Table 3.1 yields $\lambda_D \approx 74\,nm$ and indicates shielding on sub-μm scales.

The previous derivation assumed that electrons obey the Maxwell-Boltzmann distribution. In order for this assumption to be valid, the number of plasma constituents must be statistically significant. This is expressed by the PLASMA PARAMETER [27]

$$N_D = \frac{4\pi}{3} n_e \lambda_D^3. \tag{3.3}$$

It approximates the number of electrons which occupy the Debye sphere. Plasma parameters $N_D \gg 1$ satisfy the statistical significance. In physical terms this case describes an IDEAL PLASMA where electrostatic interactions dominate over binary collisions. The numerical example through Table 3.1 yields $N_D \approx 170 \gg 1$, such that collision processes can be neglected in this case.

The COLLECTIVE BEHAVIOUR of plasmas with $N_D \gg 1$ is further characterised by the coupling of the individual particles through electrodynamic forces. Perturbing plasma, e.g. by space charge fields of electron bunches, or electromagnetic fields of laser pulses, expels electrons and ions from their equilibrium positions. The ions respond on time scales much longer than those of the electrons due to their larger mass, which justifies assuming a static ion background for time scales of interest for this discussion. Under this assumption, the perturbation causes a local imbalance of the plasma electron density and thus separates electrons and ions, which induces re-attracting forces that send electrons back towards their initial positions. This results in collective oscillations of all perturbed plasma electrons with the PLASMA FREQUENCY

$$\omega_p = \sqrt{\frac{n_e e^2}{\epsilon_0 m_e}}, \tag{3.4}$$

where cold and un-magnetised plasma with a static ion background was assumed in the linear limit [27]. The plasma frequency ω_p governs numerous dynamics relevant to this work, such as the size and field strength in non-linear blowouts (see Chapter 5). In this case,

however, the plasma oscillations are excited by relativistic electron beams propagating with the group velocity $v_g \approx c$ resulting in plasma waves travelling at the same speed. Then, related quantities such as the plasma wavelength $\lambda_p = 2\pi v_g/\omega_p \approx 2\pi c/\omega_p$, or the plasma wave number $k_p = \omega_p/v_g \approx \omega_p/c$ are introduced and often used for normalisation of equations. Plasma densities typically employed at SLAC FACET (cf. Table 3.1 and Chapter 8) yield $\omega_p \approx 17.9\,\mathrm{THz}$, implying ultra-short time scales $\tau_p = 1/\omega_p \approx 56\,\mathrm{fs}$. The spatial scales of this example amount to $\lambda_p \approx 106\,\mu\mathrm{m}$ and $k_p \approx 6 \times 10^4\,\mathrm{m}^{-1}$.

3.2 OVERVIEW OF IONISATION MECHANISMS

The generation of plasma is fundamental for this work as it sets the foundations for controlled PWFA. The development of laser technology made it possible to study ionisation mechanisms in the first place, and thus paved the way for employing optical schemes as plasma sources. This section summarises basic ionisation concepts and roughly follows [124].

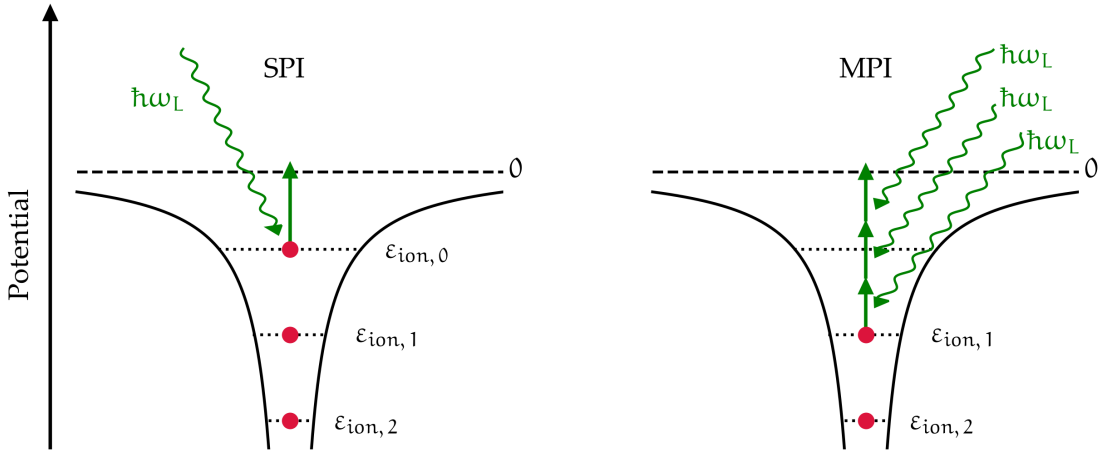

Figure 3.1: Principle of photon ionisation by single photons (SPI) and multiple photons (MPI): Bound electrons (red dots) occupy energy states $\varepsilon_{ion,n}$ in the effective Coulomb potential (solid black lines) of their parent systems. Photons (curly, green arrows) liberate bound electrons by transferring their energy $\hbar\omega_L$.

Ionisation refers to the process of stripping an electron from a bound state within an atom or molecule. Because of their quantum nature these systems are characterized by discrete states with wave functions ψ_n describing the probability density of a particle to occupy certain regions and according energy eigenvalues $\varepsilon_{ion,n}$. Both, ψ_n and $\varepsilon_{ion,n}$ can be obtained by solving the time dependent Schrödinger equation (TDSE), whereas only special cases allow for tractable, analytical solutions. This caused the inception of a variety of ionisation models covering particular scenarios. These can be

categorised with the help of energy scales [124] given by the ionisation potential ε_{ion}, photon energy $\hbar\omega_L$ and the ponderomotive potential U_p introduced in Eq. (2.14). The ponderomotive potential U_p incorporates properties of the field, whereas ε_{ion} and $\hbar\omega_L$ contain information on the material and the photon picture of the incident radiation, respectively. Using these quantities, two overarching regimes can be defined. For low intensities, the photon picture governs the ionisation dynamics. In this case, electrons occupy different energetic states within the effective Coulomb potential $V_{eff} = \frac{-1}{4\pi\epsilon_0}\frac{Ze^2}{|x|}$ of its parent system, where Z denotes the systems state after ionisation. In contrast, for larger intensities the incident field $\vec{E} = E_L\vec{e}_x$ modulates the effective Coulomb potential such that $V_{eff} = \frac{-1}{4\pi\epsilon_0}\frac{Ze^2}{|x|} - eE_Lx$.

Table 3.2: Ionisation properties of gases [138] typically employed in PWFA. ε_{ion} and Z denote the ionisation energy and the charge state after ionisation. λ_{eq} and E_{BSI} correspond to the wavelength required to generate photo electrons via the photoelectric effect and the critical field for BSI ionisation given in Eq. (3.8).

	Li	H	He	He^+
ε_{ion} (eV)	5.4	13.6	24.5	54.4
Z	1	1	1	2
λ_{eq} (nm)	230	91	50	23
E_{BSI} (GV/m)	18.8	75.3	183.0	602.5

The first description of ionisation processes in the photon picture can be traced back to Einstein [48], who discovered the PHOTOELECTRIC EFFECT, or SINGLE PHOTON IONISATION (SPI). It obeys $\hbar\omega_L \geqslant \varepsilon_{ion} \gg U_p$ [124] and is visualised in Fig. 3.1 (left): an incident photon (curly arrow) provides the energy required to lift the bound electron (red dot) beyond regions of the potential's influence, i.e. to $V_{eff} > 0$. Photon energies exceeding the ionisation potential convert to kinetic energy of the electron. For commonly used Ti:sapphire laser systems with $\lambda_L \approx 800\,nm$, however, this mechanism resembles an ineffective means of plasma generation because $\hbar\omega_L \approx 1.5\,eV$ limits the choice of gases that can be ionised and does not suffice to ionise gases typically employed in wakefield accelerators with $\varepsilon_{ion} > 5\,eV$ (cf. Table 3.2). In order to ionise such gases by SPI requires wavelengths of the order of $\lambda_{eq} \approx 100\,nm$ and smaller as displayed in Table 3.2, which is currently not accessible by common laser systems.

For $\varepsilon_{ion} > \hbar\omega_L \gg U_p$, the previous mechanism does no longer allow for ionisation. However, for increased photon flux $F = I_L/\hbar\omega_L$ [45] higher photon densities $n_{phot} \approx F/c \approx N/c\tau w_0$ are achieved. This results in finite probabilities to find N photons interacting with a single bound electron as sketched in Fig. 3.1 (right), such that $N\hbar\omega_L \geqslant \varepsilon_{ion}$. The ionisation probability is then proportional to I_L^N [8] and this process is termed MULTI PHOTON IONISATION (MPI). The involved photon densities can be estimated by assuming a Ti:sapphire laser pulse with $\lambda_L \approx 800\,nm$ and $I_L = 10^9\,W/cm^2$. Such intensities are readily accessible for TW-class laser systems and yield $n_{phot} \approx 10^{17}\,cm^{-3}$.

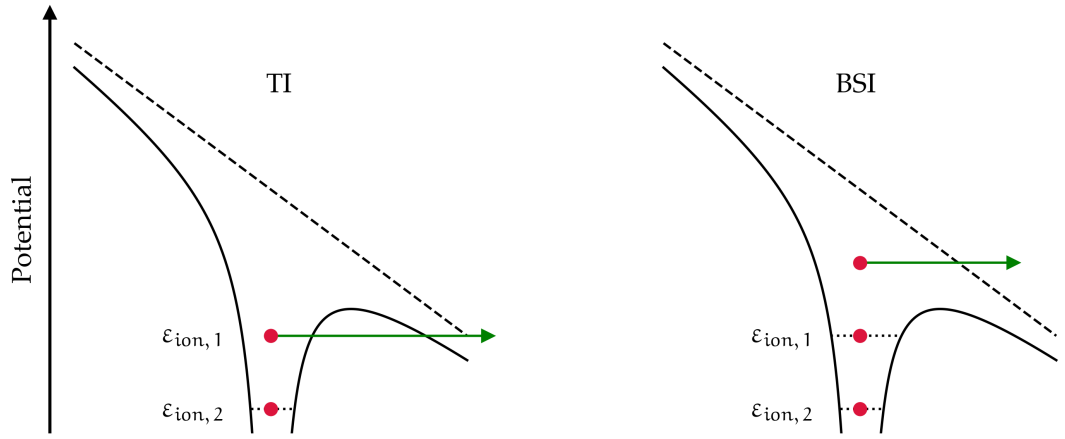

Figure 3.2: Principle of field ionisation in the tunnelling regime (TI) and the barrier suppression regime (BSI): Bound electrons (red dots) occupy energy states $\varepsilon_{ion,n}$ in the effective Coulomb potential (solid black lines), which is modulated by the incident electric field E_L. This allows the electron for tunnelling through the finite potential barrier (TI), or to classically escape its parent system (BSI).

Atomic hydrogen of density $n = 10^{16}\,cm^{-3}$ would therefore interact with roughly ten photons per atom. However, this is a strong simplification and accurate modelling would require a quantum mechanical treatment, which is beyond the scope of this thesis.

For further increased intensities the field nature overcomes the photon picture and interactions between laser pulses and atoms can no longer be described as perturbation. In fact, the strong electric fields modulate the effective Coulomb potential as shown in Fig. 3.2 and allows for additional means to liberate electrons from their binding potential. In all cases outlined in the following, $U_p > \varepsilon_{ion} > \hbar\omega_L$ is fulfilled. This implies that the electron motion due to the electric field overcomes the ionisation potential. Furthermore, the ionisation dynamics are fast compared to one field cycle $1/\omega_L$ as expressed by the Keldysh parameter introduced in Eq. (3.7). Consequently, the laser field does not vary significantly during the ionisation process, such that these models are based on the approximation of quasi-static fields.

Fig. 3.2 (left) shows the scenario, where the electric field distorts the Coulomb potential such that an electron finds itself close to a finite potential barrier. The quantum nature of the electron then allows for tunnelling through this reduced barrier. This process is thus termed TUNNELLING IONISATION (TI). To avoid computationally demanding solutions of the TDSE and to ease embedding this mechanism into simulation codes [16], modelling this process has been comprehensively studied in the past [12, 127, 128, 135, 138]. The ADK theory [4] resembles one renowned approximation of tunnelling rates, which can be cast into the form [28]

$$W_{ADK,av} \approx 57.11 \frac{Z^2}{n_{eff}^{4.5}} \left(10.87 \frac{E_h}{E_L} \frac{Z^3}{n_{eff}^4}\right)^{2n_{eff}-1.5} \exp\left(-\frac{2}{3}\frac{E_h}{E_L}\frac{Z^3}{n_{eff}^3}\right), \tag{3.5}$$

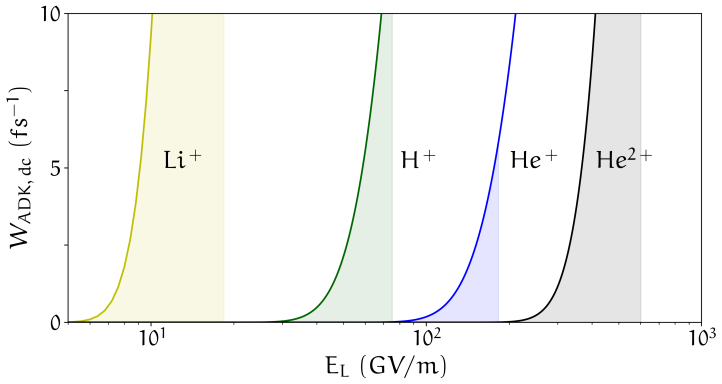

Figure 3.3: Tunnelling rates for various gases. Shown are momentary ADK rates $W_{ADK,dc}$ according to Eq. (3.6) as function of field strength E_L. Shaded regions highlight field values $E_L \leqslant E_{BSI}$ applicable to the ADK model.

where $n_{eff} \approx Z/\sqrt{|\varepsilon_{ion}/13.6\,eV|}$ is the effective principal quantum number, ε_{ion} enters the equation in units of eV and $E_h \approx 0.513\,TV/m$. Equation (3.5) expresses the ionisation rate in units of fs^{-1}. Note, that this representation refers to the cycle-averaged rate applicable for linearly polarised laser pulses in the envelope approximation. This allows for temporal resolution larger than one oscillation period in simulations and therefore enables less costly computation. However, for calculations including oscillating fields, the quasi-static ADK rates may be used [16, 28]

$$W_{ADK,dc} = \left[\frac{\pi E_h}{3E_L}\frac{Z^3}{n_{eff}^3}\right]^{1/2} W_{ADK,av}, \tag{3.6}$$

which is further valid for circularly polarised laser pulses [43, 138].

As an example, computing Eq. (3.6) for atomic hydrogen and $E_L \approx 22\,GV/m$ yields instantaneous tunnelling rates of $W_{ADK,dc} \approx 10^{-3}\,fs^{-1}$. Maintaining this field strength over $\tau = 100\,fs$ would yield the ionisation probability $P_{ADK,dc} \approx 10\,\%$. In contrast, increasing the field strength to $E_L \approx 27\,GV/m$ leads to $P_{ADK,dc} \approx 1$, i.e. full ionisation. TI is therefore very sensitive to the field strength E_L as a result of the exponential behaviour of Eqs. (3.5) and (3.6).

The sensitivity of $W_{ADK,dc}(E_L)$ is visualised in Fig. 3.3 for various gases typically employed in PWFA. The non-linear behaviour of W_{ADK} results in large gaps separating different ionisation levels, which can be harnessed for SELECTIVE IONISATION. For example, using a hydrogen/helium gas mixture and $E_L = 70\,GV/m$ ($I_L \approx 7\times10^{14}\,W/cm^2$) leads to significant ionisation of hydrogen only and leaves helium in its gaseous state. Employing a second laser pulse of higher intensity can then facilitate the generation of additional helium plasma. This resembles an effective means of tailoring flexible plasma sources, which find application in PWFA injectors, such as the plasma photocathode [44, 74] and the all-optical density downramp injection [175, 187, 188] as demonstrated at SLAC FACET.

In certain parameter ranges both, TI and MPI can occur. In this case, both regimes can be distinguished by the KELDYSH PARAMETER [90]

$$\gamma_K = \omega_L T_t = \sqrt{\frac{\varepsilon_{ion}}{2U_p}}. \tag{3.7}$$

It quantifies the ratio of the tunnelling time T_t and one laser cycle $T_L \approx \lambda_L/c$, such that $\gamma_K < 1$ describes TI and $\gamma_K > 1$ corresponds to MPI. However, this quantity should be treated as an estimate particularly for $\gamma_K \approx 1$, where both mechanisms contribute to ionisation. In this case, specialised models lead to more accurate ionisation rates, e.g. the Yudin-Ivanov theory [194], which become increasingly important for laser pulses with short wavelengths, e.g. $\lambda_L \approx 400\,nm$ [61].

Clearer dependencies arise for further increased field strengths. Then, the potential barrier reduces significantly, and the electron finds itself classically freed from the barrier as illustrated in Fig. 3.2 (right). This process is called BARRIER SUPPRESSION IONISATION (BSI) and occurs for electric field values in excess of [11, 16]

$$E_{BSI} = (\sqrt{2}-1)\left|\frac{\varepsilon_{ion}}{27.2eV}\right|^{3/2} E_h, \tag{3.8}$$

which marks the boundary to TI at the same time. BSI is typically triggered in laser wakefield accelerators, where multi-*TW* to *PW*-class lasers combine plasma generation and wake excitation. In these cases, electric fields easily surpass E_{BSI} for a wide range of materials as shown in Table 3.2. Hydrogen, for example, requires $E_L > 75\,GV/m$ or $I_L > 7.5 \times 10^{14}\,W/cm^2$, which is exceeded by laser pulses considered in this work. However, a more thorough investigation outlined in Section 8.3 demonstrates that tunnelling ionisation can be completed on the raising edge of a laser pulse, even if the peak field of the pulse exceeds E_{BSI}. This allows for designing plasma sources based on the tunnelling gaps illustrated in Fig. 3.3, which facilitate selective ionisation as a vital prerequisite for plasma torch PWFA.

3.3 DYNAMICS OF OPTICALLY FIELD-IONISED PLASMA

This work is mainly concerned with plasmas from optical field ionisation (OFI) in the tunnelling regime, as this process governs various aspects relevant to the PWFA presented in later chapters. For instance, the generation of plasma channels that sustain the plasma accelerator, but also the production of density spikes for controlled injection of electrons into the wakefield depend strongly on the involved ionisation dynamics, which ultimately set the initial conditions for the plasma accelerator. However, designing plasma sources for successful and reliable PWFAs additionally requires the consideration of thermal effects as these determine, e.g thermal expansion times, which should be mitigated for maximum control of PWFA experiments at SLAC FACET.

The laser properties of interest are $a_0 \ll 1$, $\tau \approx 100\,\mathrm{fs}$, such that ABOVE THRESHOLD IONISATION (ATI) is the dominating heating mechanism [24, 36], which can be described as a two-step process [98]. First, electrons tunnel through the distorted potential barrier. Second, the liberated, free electrons gain energy through the interaction with the laser pulse until it passed. The second step can be studied in approximation by the motion of a free particle in a plane wave propagating in z-direction. The corresponding potential can be treated in the slowly varying envelope approximation and reads [60]

$$\vec{A}_L(t) = a_0 \frac{m_e c^2}{e} \exp\left(-4\log(2)\frac{t^2}{\tau^2}\right) \begin{pmatrix} \delta\cos(\omega_L t) \\ \sqrt{1-\delta^2}\sin(\omega_L t) \\ 0 \end{pmatrix}, \tag{3.9}$$

where δ denotes arbitrary polarisation of the pulse. Integrating the equations of motion of an electron under the influence of $\vec{A}_L(t)$ then yields constants of motion [60], which can be rewritten to obtain the electron energy after the laser passed [97]

$$\varepsilon_e = \frac{e^2}{2m_e c^2}|\vec{A}_0|^2. \tag{3.10}$$

Here, $\vec{A}_0 = \vec{A}_L(t_0)$ corresponds to the vector potential at the electron's time of birth t_0, which depends on the ionisation probability, i.e. the electric field strength $|\vec{E}_L(t_0)| = |\partial\vec{A}/\partial t|(t_0)/c$. Conversely, the final electron energy ε_e is determined by $|\vec{A}_0|^2$. This has some interesting implications that depend on the laser polarisation δ.

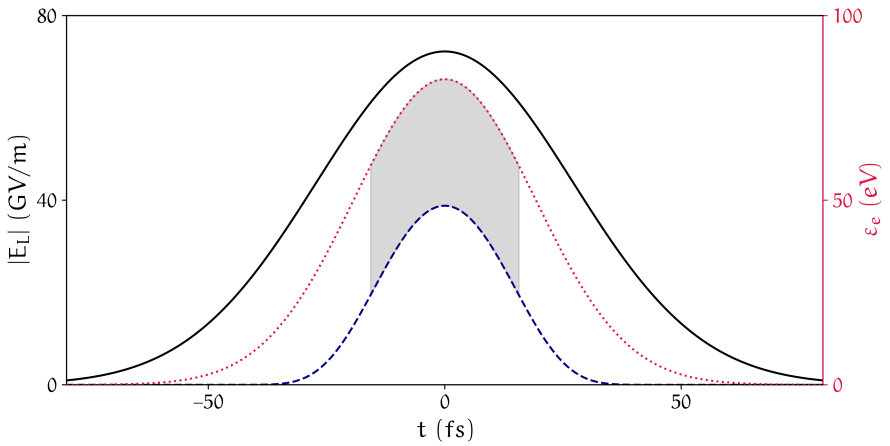

Figure 3.4: Above threshold ionisation for circularly polarised laser pulses. Shown are the absolute value $|\vec{E}_L(t)|$ of the electric field (black, left axis), the corresponding tunnelling rate $W_{ADK,dc}$ (blue) and the energy ε_e of generated photo electrons (red, right axis). Grey shades indicate regions of significant ADK rates concurring with maximum photo electron energies.

For example, circular polarisation $\delta = 1/\sqrt{2}$ yields $|\vec{E}_L| \propto \exp\left(-4\log(2)t^2/\tau^2\right)$ and $|\vec{A}_L| \propto \exp\left(-4\log(2)t^2/\tau^2\right)$, i.e. is a function of the pulse envelope only. This is visualised in Fig. 3.4 for $\lambda_L = 800\,\mathrm{nm}$, $\tau = 64\,\mathrm{fs}$ and $a_0 = 0.036$ ($I_L \approx 7 \times 10^{14}\,\mathrm{W/cm^2}$). Here, the

largest tunnelling rates (blue and grey shades) occur at the same times as the maximum potential, such that photo electrons gain high energies after the interaction with the laser as indicated by ε_e (red). This laser configuration hence produces electron energies in excess of 80 eV and the spectra are expected to be broad and approximately Gaussian shaped [36, 157]. Circular polarisation thus provides an effective tool to generate hot plasma, e.g. to form plasma channels for laser guiding [157].

In contrast, linearly polarised laser pulses $\delta = \pm 1, 0$ feature $|\vec{E}_L|$ and $|\vec{A}_L|$ including rapid laser oscillations. However, the oscillation of $|\vec{E}_L|$ and $|\vec{A}_L|$ are phase shifted by $\pi/2$ due to $\vec{E}_L \propto \partial\vec{A}/\partial t$. Figure 3.5 a) visualises such a pulse for $\lambda_L = 800\,nm$, $\tau = 64\,fs$ and $a_0 = 0.018$ ($I_L \approx 7 \times 10^{14}\,W/cm^2$). The magnified representation in Fig. 3.5 b) highlights the consequence of the phase shift: the largest tunnelling rates (blue) concur with the smallest ε_e (red), such that the majority of photo electrons gain minuscule energies. The resulting spectra of the photo electrons hence drop exponentially with the electron energy [98]. Linearly polarised lasers are thus well suited for producing initially cold plasma [24, 141] with temperatures of the order $T_e \approx 10\,eV$ [97].

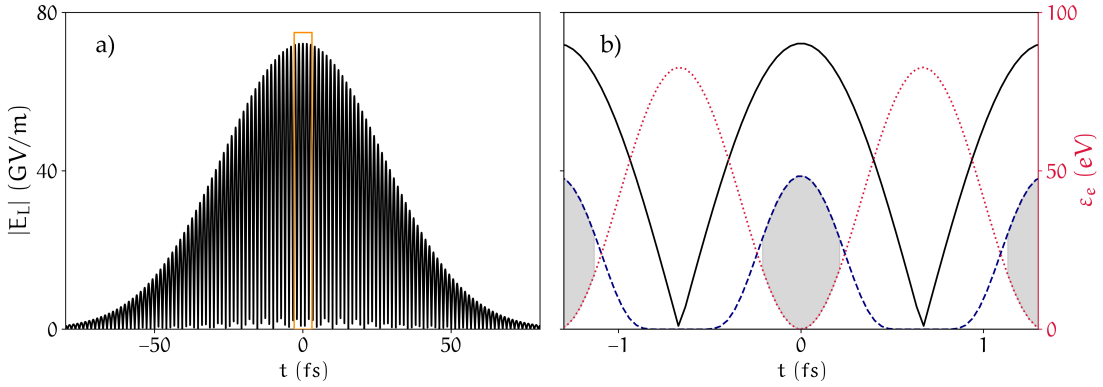

Figure 3.5: Above threshold ionisation for linearly polarised laser pulses. Shown are the absolute value $|\vec{E}_L(t)|$ of the electric field (black, left axis), the corresponding tunnelling rate $W_{ADK,dc}$ (blue) and the energy ε_e of generated photo electrons (red, right axis). b), magnification of region marked orange in a). Grey shades indicate regions of significant ADK rates concurring with minimum photo electron energies.

After the laser left the medium, it leaves behind the newly formed plasma, which is subject to different dynamics. Here, processes involving the electrons occur more rapidly compared to the ions with much larger inertia. For electrons, the characteristic thermalisation time scale is given by the SPITZER SELF-COLLISION TIME [124, 157, 161]

$$\tau_{ee} = \frac{2.8\pi\epsilon_0^2\sqrt{m_e}}{e^4}\frac{(3k_B T_e)^{3/2}}{n_e \log\Lambda}, \tag{3.11}$$

where $\log\Lambda$ denotes the Coulomb logarithm [27] with $\Lambda = 6\,N_D$ and takes into account Debye shielding during interactions. Equation (3.11) characterises the time over which a thermal electron distribution approaches its equilibrium. For typical plasma sources employed in PWFA with $n_e \approx 10^{23}\,m^{-3}$ and $T_e \approx 10\,eV$, the Spitzer self-collision time

amounts to $\tau_{ee} \approx 14\,\mathrm{ps}$. However, additional processes take place for bounded density distributions, e.g. from optical tunnelling ionisation. Here, Sedov-Taylor blast waves can occur due to the energetic difference of the localised plasma versus a cold background medium and leads to shock formations. This process propagates with the speed of sound of the ions $v_i = \sqrt{Zk_B T_e/m_i}$ [31, 159], i.e. over hundreds of ps for plasmas relevant to this work [47, 98]. The plasma dynamics are further complicated by effects such as ambipolar diffusion [13, 27], which occurs on similar time scales [81, 160].

To mitigate thermal dynamics and establish reliable initial conditions for the PWFA, cold plasmas are desired. This suggests employing linearly polarised laser pulses of moderate $a_0 \ll 1$ for controlled generation of photo electrons with minimised residual transverse momentum. Assuming cold plasma for the theoretical and numerical investigations of PWFA in later chapters is therefore justified.

4

RELATIVISTIC PARTICLE BEAMS

Intense particle beams are the drivers of plasma wakefield accelerators. Historically, particle beams are an extreme case of non-neutral plasma, such that plasma terminology can be often used [57] for drive beams that excite plasma waves and for witness beams that form and accelerate in the plasma wake. In general, PWFAs can be driven by positron beams [35], proton beams [2] or electron beams [99, 146]. However, this thesis is concerned with electron beam drivers, which are readily accessible from linear accelerators (linacs), or LWFAs. This chapter introduces important properties of electron beams following [80, 142, 145, 183].

Electron beams constitute ensembles of particles behaving as a collective. Such beams can contain 10^{10} and even more particles, which make their mathematical treatment intricate depending on the level of simplifications. Various formalisms have therefore been developed to describe the dynamics of these ensembles. An analytical treatment is possible by describing particle beams as density distributions n_{6D} in the six-dimensional PHASE SPACE, or the related TRACE SPACE. The phase space is based on the canonical co-ordinates q_i and momenta p_i that characterise the system's Hamiltonian. Conversely, the trace space employs canonical co-ordinates q_i and their slopes with respect to the propagation direction x: $q_i' = dq_i/dx = \dot{q}_i/\dot{x} \approx p_i/p_x$. Benefits of the latter are that the beam divergence q_i' can be measured in experiments, e.g. by scintillating screens, which makes this choice more tractable.

For electron beams that obey Hamiltonian mechanics and for negligible particle loss or generation, the total number of particles N occupying the 6D trace space is constant at all times according to LIOUVILLE'S THEOREM [145]. The total number of particles is given by $N = \iint n_{6D}\, d^3q\, d^3q'$ in trace space, or $N = \iint n_{6D}\, d^3q\, d^3p$ in phase space and relates to the beam's total charge

$$Q_b = eN. \tag{4.1}$$

For instance, typical electron beams at SLAC FACET have a charge of $Q_b \approx 3\,\mathrm{nC}$, i.e. $N \approx 2 \times 10^{10}$. In case of negligible particle loss or generation, Liouville's theorem further states that the 6D volume occupied by particles n_{6D} remains constant. However, its shape may be subject to change. This theorem is valid as long as single particles of the beam interact only weakly with neighbouring particles, i.e. when intra-beam space charge forces as well as collisions are weak. This holds as long as the fields of the overall beam are stronger than particle-particle interactions, which can be quantified by $\lambda_D^3 \gg 1/n_b$ [142], where n_b denotes the beam density. This theorem has far reaching consequences in accelerator science and governs most dynamics relating to electron beams for PWFAs.

It can be further simplified, when assuming that all directions i do not couple. All trace space planes q_i, q_i' can then be separated and treated individually. The following sections discuss transverse and longitudinal properties of electron beam distributions.

4.1 TRANSVERSE PROPERTIES OF GAUSSIAN ELECTRON BEAMS

A common approximation of electron beams follows Maxwellian trace space distributions [145]

$$n_{2D}(y, y') = \frac{1}{2\pi\varepsilon_y} \exp\left(-\frac{\sigma_{y'}^2 y^2 - 2\sigma_{yy'} yy' + \sigma_y^2 y'^2}{2\varepsilon_y^2}\right), \tag{4.2}$$

where yy' denotes one transverse trace space plane as function of on the propagation distance x. Here, $\sigma_y(x)$ and $\sigma_{y'}(x)$ denote the r.m.s. widths of the distribution in y and y', i.e. the envelope and angle spread of the beam. The correlation $\sigma_{yy'}(x)$ accounts for the coupling between y and y' such as the beam's focusing. ε_y represents the R.M.S. TRACE SPACE EMITTANCE. Considering the distribution's contours of constant density, the trace space ellipse can be identified, which is commonly used for illustrating the properties of such beam profiles [145]

$$\sigma_{y'}^2 y^2 - 2\sigma_{yy'} yy' + \sigma_y^2 y'^2 = \varepsilon_y^2. \tag{4.3}$$

This equation describes an ellipse with area $A = \pi\varepsilon_y$. Recalling Liouville's theorem, ε_y can be identified as constant under beam transport, i.e. disregarding energy gain of the beam. Furthermore, the number of particles that is enclosed by the corresponding contour does not change. Figure 4.1 illustrates these effects for two generic bi-Gaussian trace space distributions featuring the same emittance ε_y. Panel a) corresponds to an uncorrelated trace space $\sigma_{yy'} = 0$ as expected at the focus position of a beam after ideal focusing with a thin lens. In this case $\varepsilon_y = \sigma_y \sigma_{y'}$ [145]. In contrast, Fig. 4.1 b) shows the distribution of a diverging beam, e.g. after the focal position of the beam illustrated in a). The correlation through $\sigma_{yy'}$ leaves ε_y unaffected as indicated by the area enclosed by the orange line, but leads to a skewed trace space ellipse. Including the correlation term $\varepsilon_y^2 = \sigma_y^2 \sigma_{y'}^2 - \sigma_{yy'}^2$.

This formalism can further be employed to characterise the evolution of the beam distribution in the presence of various forces, such as a homogeneous ion background, or the self-fields of the beam. In the case of a transversally symmetric Gaussian beam, its envelope $\sigma_y(x)$ obeys the differential equation [6, 151]

$$\frac{d^2\sigma_y}{dx^2} + \frac{k_p^2}{2\gamma_b}\sigma_y - \frac{\varepsilon_y^2}{\sigma_y^3} - \frac{I_p}{2I_0\gamma_b^3\sigma_y} = 0. \tag{4.4}$$

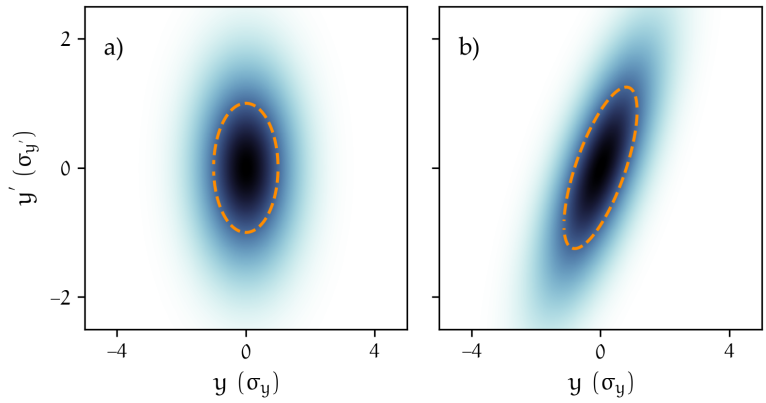

Figure 4.1: Bi-Gaussian trace space distribution of particle beams featuring equal r.m.s. emittance ε_y. Orange lines indicates the trace space ellipse for a), uncorrelated ($\sigma_{yy'} = 0$) and b), correlated ($\sigma_{yy'} \neq 0$) beam distributions.

Here, the second term represents the contribution of the background ions, similar to the PWFA blowout regime discussed in Chapter 5. The evolution of the beam envelope thus depends on the ion density n_i via the focusing through the wave number $k_p = k_p(n_i)$ and the beam's relativistic gamma factor $\gamma_b = 1/\sqrt{1-\beta_b^2}$. The two last terms characterise the beam expansion due to its emittance and space charge. The latter depends on the beam's peak current I_p introduced in Section 4.2 and the characteristic current $I_0 \approx 17\,\mathrm{kA}$. Additional terms may be incorporated [111, 142, 145], but describe effects that are not of interest for the current discussion.

In the absence of plasma $k_p \approx 0$ and for negligible beam currents $I_p \approx 0$, Eq. (4.4) can be integrated and yields an interesting result [125, 142]

$$\sigma_y(x) = \sigma_{y,0}\sqrt{1+\left(\frac{\varepsilon_y x}{\sigma_{y,0}^2}\right)^2}, \tag{4.5}$$

where $\sigma_{y',0} = 0$ has been chosen and x corresponds to the distance from the beam waist $\sigma_{y,0}$. Equation (4.5) equals the envelope equation for Gaussian laser beams outlined in Eq. (2.9) when replacing $\varepsilon_y = \lambda_L/\pi$ [125]. A "Rayleigh length" for particle beams can therefore be defined as $\beta^* = \sigma_{y,0}^2/\varepsilon_y$ analogous to laser beams $z_R = w_0^2/\pi\lambda_L$. Typical laser systems used for wakefield acceleration operate at $\lambda_L \approx 800\,\mathrm{nm}$, whereas linacs can provide r.m.s. trace space emittance values $\varepsilon_y \approx 7\,\mathrm{nm\,rad}$ [163]. For equal focal spot sizes it follows $\beta^*/z_R \approx 360$, i.e. electron beams diverge over orders of magnitude longer distances compared to laser beams. This is particularly beneficial when using electron beams for driving wakefield accelerators, which consequently accelerate over larger distances compared to laser driven wakefield accelerators.

The analogy of Gaussian laser beams and Gaussian particle beams features further implications. For instance, the smallest spot size achievable by focusing with a thin lens scales with the respective Rayleigh length. Electron beams with low emittance values can

therefore reach smaller foci. Of particular interest in this thesis, PWFAs profit from the increased density of strongly focused electron beams, e.g. to excite strong interactions in plasmas.

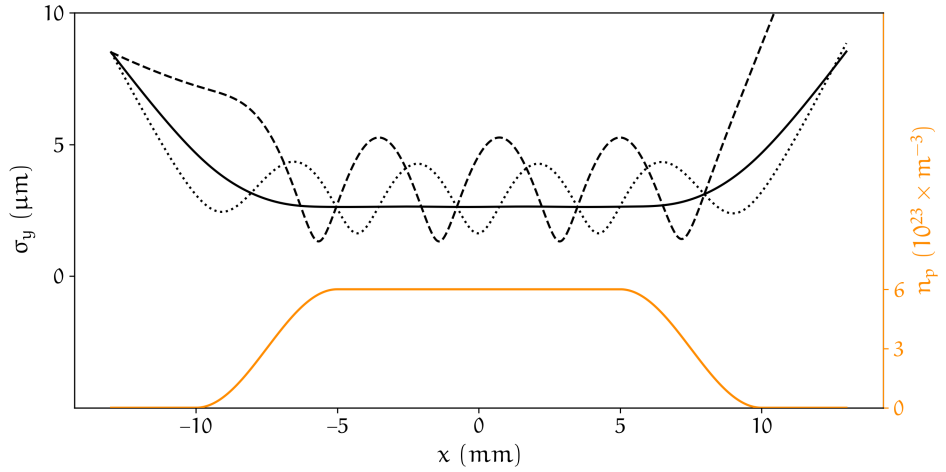

Figure 4.2: Transverse plasma matching of Gaussian electron beams with $\varepsilon_y \approx 5\,\mathrm{nm\,rad}$ ($\varepsilon_{n,y} = 100\,\mu\mathrm{m\,rad}$) and negligible peak current $I_p \approx 0$ propagating from left to right. Numerical evaluation of Eq. (4.4) based on the illustrated plasma density distribution (orange, right axis) and resulting envelope evolution for matched focusing (solid line), under-focusing (dashed line) and over-focusing (dotted line).

Including all terms in Eq. (4.4) complicates the evolution of the beam envelope and does not allow for analytical solutions. However, the strong scaling of the space charge term with $\propto \gamma_b^{-3}$ indicates that this term governs the beam expansion for low beam energies and peak currents I_p of the order of I_0 or larger. For example, this occurs during the injection of high-charge witness beams and may lead to deteriorated emittance values in extreme cases. In contrast, high γ_b suppress the space charge term and expansion is dominated by the emittance contribution in Eq. (4.4), e.g. for the electron beams available at SLAC FACET where $\gamma_b \approx 45000$ [78]. In this case, the form of the second term suggests envelope oscillations with the betatron frequency $\omega_B = \omega_p/\sqrt{2\gamma_b}$. These can be suppressed by initially matching the envelope to the plasma, such that it is guided. This is achieved when the plasma focusing balances the electron beam's expansion, such that $d^2\sigma_y/dx^2 = 0$ and the matched beam waist reads

$$\sigma_{y,m} = \left(\frac{2\gamma_b \varepsilon_y^2}{k_p^2}\right)^{1/4} . \tag{4.6}$$

Transverse beam matching is particularly important for PWFAs, which rely on long interaction distances of the beam and the plasma. Typically, the plasma sources used for wake excitation do not exhibit homogeneous distributions, such that numerical solution of Eq. (4.4) is required to find the initial envelope $\sigma_{y,0}$ and beam divergence $\sigma'_{y,0}$ that match to the plasma. This is visualised in Fig. 4.2 for a density distribution comprised of

a cosine upramp, constant section of $n_p = 6 \times 10^{23}\,\mathrm{m}^{-3}$, followed by a cosine downramp (orange line, right axis). Choosing beam parameters $\varepsilon_y \approx 5\,\mathrm{nm\,rad}$ and $\gamma_b \approx 19569$ available at SLAC FACET II [191], beam matching is studied assuming negligible peak currents $I_p \approx 0$. The black lines in Fig. 4.2 illustrate envelopes (black lines, left axis) of these beams for different initial conditions. The black solid line shows matched focusing, which adapts to the plasma on the density upramp, reaches the matched value on the constant section of the density profile and remains constant until it approaches the density downramp. After that, the beam couples out of the plasma and continues its evolution symmetrically to $x = 0$. The over-focused beam (dotted line) and under-focused beam (dashed line) do not reach the matched radius at the constant section of the density profile and therefore undergo betatron oscillations inside the constant plasma segment. These oscillations cause periodic compression of the electron beam density, which affects, e.g., the excitation of plasma waves and therefore creates varying conditions for electron acceleration.

4.2 LONGITUDINAL PROPERTIES OF GAUSSIAN ELECTRON BEAMS

Similar to the transverse compression of particle beams, a longitudinal property can be derived from Eq. (4.1). Assuming an uncorrelated distribution propagating at constant velocity v_b and transforming into the frame of reference co-moving with the beam $\xi = x - v_b t$ one obtains the beam's CURRENT DISTRIBUTION [133, 186]

$$I_b = \frac{dQ_b}{dt} = v_b \frac{\partial Q_b}{\partial \xi} = \frac{v_b Q_b}{\sqrt{2\pi}\sigma_x} \exp\left(-\frac{\xi^2}{2\sigma_x^2}\right). \tag{4.7}$$

This property quantifies the longitudinal distribution of the beam charge and strongly depends on the peak current $I_p = v_b Q_b / \sqrt{2\pi}\sigma_x$. Large beam currents represent high quality and dense distributions, which is vital for numerous applications, e.g. for exciting strong plasma waves in PWFAs. Here, certain current distributions of the driver beam can alter the accelerating plasma wakefields [29, 107, 184], such that shaping of I_b is a common tool for optimising the energy transfer in PWFAs as discussed in Sections 5.2 and 5.3.

Longitudinal processes further affect transverse properties of the beam as previously indicated in Eq. (4.4). For instance, the emittance ε_y no longer remains constant for electron beams that gain energy. To obtain a commensurable quantity for beams of various energies, the NORMALISED EMITTANCE is defined as [183]

$$\varepsilon_{n,y} = \beta_b \gamma_b \varepsilon_y = \sqrt{\gamma_b^2 - 1}\,\varepsilon_y. \tag{4.8}$$

It is a measure of the beam quality and therefore characterises the accelerator and the beam transport. For plasma wakefield accelerators, the normalised emittance is

ultimately limited by the generation of the particle beam which highlights the importance of controlling the employed injection process. Normalised emittance values which have been produced by plasma wakefield accelerators range from 0.1 to 100 $\mu m\,rad$ [17, 44, 137] and simulations predict even lower values of the order of $10\,nm\,rad$ [74, 108]. These numbers rival the state-of-the-art of conventional accelerators and hence fuel the endeavours to realise these advanced plasma injector schemes.

4.3 REALISTIC BEAM DISTRIBUTIONS AND BEAM QUALITY

So far, only properties of idealised particle beams have been studied by assuming Gaussian distributions. However, in practice electron beams deviate from this description as they are comprised of discrete particles such that Eq. (4.2) no longer holds. This necessitates a statistical definition of the beam's properties to enable the analysis of experimental data and results from particle-in-cell simulations. For instance, the statistical definition of the r.m.s. trace space emittance reads [58]

$$\varepsilon_y = \sqrt{\langle y^2\rangle \langle y'^2\rangle - \langle yy'\rangle^2}, \tag{4.9}$$

where $\langle\rangle$ denotes the moments of the distribution. Previous discussions and physical laws also hold for the statistical formulation of the beam emittance.

Equation (4.9) completes the set of equations to define the ultimate quality indicator by combining both, the transverse and longitudinal properties to form the NORMALISED BRIGHTNESS [142]

$$B_n = \frac{2I_p}{\pi^2 \varepsilon_{n,y}\varepsilon_{n,z}}. \tag{4.10}$$

It depends on the compression of the 4D transverse trace space $\varepsilon_{n,y}$, $\varepsilon_{n,z}$ and the 1D longitudinal compression, which is why B_n is also referred to as 5D-brightness. B_n is a crucial design parameter for numerous applications such as free-electron lasers (FELs) that require enormous brightness values to lase. One state-of-the-art FEL facility is the LCLS-II, which features electron beams of $B_n \approx 3\times 10^{16}\,A/m^2\,rad^2$ [163]. However, conventional technology for producing high-quality electron beams is reaching a saturation point and may become increasingly surpassed by novel plasma-based concepts in the future [74, 107]. These promise to reach ever-higher brightness values while overcoming other limitations of their conventional counterparts as outlined in the following chapter.

5

PWFA

The following section derives the cold, relativistic fluid equations describing the excitation of 1D plasma waves by following the seminal work of Akhiezer and Polovin [3], which has been refined later for electron beam-driven plasma waves by Rosenzweig and co-workers [143, 144, 149]. Different aspects of PWFAs are studied based on this 1D theory. Properties of 3D plasma wakes are discussed in the section concluding this chapter.

5.1 PWFA IN THE 1D COLD FLUID APPROXIMATION

In the cold fluid approximation, the Maxwell equations Eqs. (2.1) to (2.4) govern the behaviour of the plasma, where all charged constituents enter the source terms on the right-hand side. Here, the number densities of plasma electrons n_e, plasma ions n_0 and the electron driver beam n_b form the charge density $\rho = -e(n_e + n_b - n_0)$. Assuming that the ions are immobile ($n_0 = \text{const}$, $\beta_0 = 0$) results in the current density $\vec{j} = -ec(n\vec{\beta} + n_b\vec{\beta}_b)$ with the normalised velocity of the plasma electrons $\vec{\beta}$ and drive beam $\vec{\beta}_b$. These quantities couple to the electric and magnetic fields $\vec{E}$ and $\vec{B}$, which, in turn, determine the change of motion of the plasma elements via the Lorentz force [52]

$$\frac{\partial \vec{p}}{\partial t} + c(\vec{\beta}\vec{\nabla})\vec{p} = -e\left(\vec{E} + c\vec{\beta} \times \vec{B}\right). \tag{5.1}$$

Equation (5.1) includes the convective derivative of the relativistic fluid momentum $\vec{p} = m_e c\gamma\vec{\beta} = m_e c\vec{\beta}/\sqrt{1-\vec{\beta}^2}$ to account for the fluid motion. Defining $\vec{e}_x$ as the propagation axis of the relativistic electron drive beam with velocity v_b, only wave solutions depending on $\xi = \omega_p(t - x/v_b)$ are studied, i.e. solutions in the frame co-moving with the drive beam. In this case, the differential operators acting on a vector field $\vec{V}$ transform according to

$$\vec{\nabla} \times \vec{V} = -\frac{\omega_p}{v_b}\vec{e}_x \times \vec{V}', \quad \vec{\nabla}\vec{V} = -\frac{\omega_p}{v_b}\vec{e}_x\vec{V}', \quad \frac{\partial \vec{V}}{\partial t} = \omega_p\vec{V}', \tag{5.2}$$

where $'$ denotes the new differentiation with respect to ξ. Using this approach significantly simplifies Eqs. (2.1), (2.3), (2.4) and (5.1)

$$E'_\xi = -\frac{e v_b}{\epsilon_0 \omega_p}\left(n_0 - n_e - n_b\right), \tag{5.3}$$

$$\vec{e}_x \times \vec{E}' = v_b \vec{B}', \tag{5.4}$$

$$\vec{e}_x \times \vec{B}' = \frac{\mu_0 v_b e c}{\omega_p}\left(n_e \vec{\beta} + n_b \vec{\beta}_b\right) - \epsilon_0 v_b \vec{E}', \tag{5.5}$$

$$\left(1 - \frac{\beta_x}{\beta_b}\right)\left(\gamma\vec{\beta}\right)' = -\frac{e}{m_e c \omega_p}\left(\vec{E} + \vec{v} \times \vec{B}\right). \tag{5.6}$$

Equation (5.4) can be readily integrated and yields $\vec{e}_x \times \vec{E} = v_b(\vec{B} + \vec{B}_0)$, where $\vec{B}_0$ denotes external magnetic fields. Magnetised plasmas are not of interest for the current discussion, such that $\vec{B}_0 = 0$. In this case, the magnetic field is always directed perpendicularly to the electric field. For this particular choice of co-ordinates follows that $B_x = 0$. Incorporating this in Eq. (5.3) and the x-components of Eq. (5.5) gives Eq. (5.7). Further, $\vec{e}_x \times$Eq. (5.5) and using Eq. (5.4) yields Eq. (5.8).

$$n_e(\vec{\beta}) = \frac{n_0 \beta_b}{\beta_b - \beta_x} \tag{5.7}$$

$$\vec{B}' = \frac{\mu_0 e c^2 \beta_b}{\omega_p} \frac{\vec{e}_x \times \vec{\beta}}{\beta_b^2 - 1} n_e(\vec{\beta}) \tag{5.8}$$

Computing $\vec{e}_x \times$ Eq. (5.6) and $\vec{e}_x$ Eq. (5.6) gives

$$\vec{e}_x \times (\gamma\vec{\beta})' = -\frac{e\beta_b}{m_e \omega_p}\vec{B}, \tag{5.9}$$

$$(\gamma\beta_x)'(1 - \frac{\beta_x}{\beta_b}) = -\frac{e}{m_e \omega_p}(E_\xi + \vec{e}_x(\vec{v} \times \vec{B})). \tag{5.10}$$

The final equation governing the longitudinal motion of the plasma results from inserting Eq. (5.9) into Eq. (5.10), subsequent differentiation and using E'_ξ from Eq. (5.5). One obtains

$$\frac{d}{d\xi}\left[(\beta_b - \beta_x)(\gamma\beta_x)' - \vec{\beta}_\perp(\gamma\vec{\beta}_\perp)'\right] = -\beta_b\left(\frac{n_b}{n_0} + \frac{\beta_x}{\beta_b - \beta_x}\right). \tag{5.11}$$

Despite the 3D ansatz, the results only support self-consistent solutions for pure longitudinal motion $\vec{\beta}_\perp = 0$ [3]. Equation (5.11) further simplifies by assuming ultra-relativistic electron beams $\beta_b \approx 1$ and substituting $\chi = \sqrt{\frac{1-\beta}{1+\beta}}$. This yields [149]

$$\chi'' = \frac{n_b(\xi)}{n_0} + \frac{1}{2\chi^2} - \frac{1}{2}, \tag{5.12}$$

and the solutions link to physical quantities via Eq. (5.7) and [149]

$$\chi' = \frac{eE_\xi}{m_e c \omega_p}, \tag{5.13}$$

$$\chi = 1 + \frac{e\phi}{m_e c^2}, \tag{5.14}$$

where ϕ denotes the electrostatic potential of the wakefield. Comparing Eqs. (5.12) to (5.14), one finds find that E_ξ features a phase shift of $\pi/2$ with respect to ϕ and n_e. Further properties can be obtained by using the initial conditions $E_\xi(0) = 0 \rightarrow \chi'(0) = 0$ and $\beta(0) = 0 \rightarrow \chi(0) = 1$, providing the 1D density distribution of the drive beam, e.g. $n_b(\xi) = n_{b,0} \exp\left(-\xi^2/2\sigma^2\right)$, to numerically integrate Eq. (5.12). Figure 5.1 shows numerical solutions of Eq. (5.12) (black lines) for Gaussian drive beam distributions of r.m.s. length $\sigma = \lambda_p/2\pi$ (grey lines) propagating to the right. a) and b) display results for driver peak densities $n_{b,0} = 0.05\ n_0$ and $n_{b,0} = n_0$, respectively.

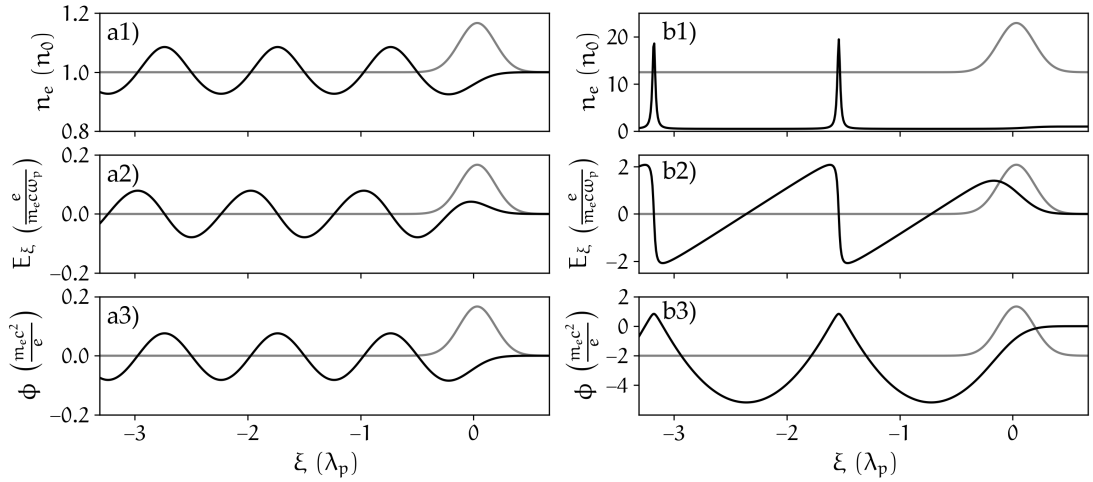

Figure 5.1: 1D wake excitation in the cold fluid approximation. Shown in black are the plasma density (first row), electric field (second row) and electrostatic wake potential (third row) alongside the Gaussian drive beam (grey) of r.m.s. length $\sigma = k_p^{-1}$. a), linear regime with $n_{b,0}/n_0 = 0.05$ and b), non-linear wake excitation with $n_{b,0}/n_0 = 1.0$.

The first case displayed in Fig. 5.1 a) marks the linear, or OVERDENSE regime of PWFA where $n_{b,0} \ll n_0$. Here, the excited wake resembles a mere perturbation which allows for expanding Eq. (5.12) into a Taylor series for non-relativistic plasma velocities $\beta \approx 0$ [118]. This yields $\chi'' + \chi - 1 = n_b/n_0$, i.e. a driven harmonic oscillator with analytical solutions. For example, the accelerating field [65]

$$E_\xi = \frac{\sqrt{2\pi}e}{m_e c \omega_p} \frac{n_{b,0}}{n_0} k_p \sigma \exp\left(-\frac{k_p^2 \sigma^2}{2}\right) \cos\left(k_p \xi\right). \tag{5.15}$$

The solutions are inherently periodic with $\lambda_p = 2\pi/k_p$ and exhibit amplitudes that scale as the perturbation $n_{b,0}/n_0$. Keeping $n_{b,0}/n_0$ and the plasma density n_0 constant,

the strongest plasma waves are excited for $k_p \sigma = 1$, which is commonly referred to as LONGITUDINAL BEAM MATCHING. The plasma density $n_e(\xi)$ is governed by the linear excitation through the drive beam as visualised in Fig. 5.1 a1). Before interacting with the driver at $\xi \geqslant 0.5\,\lambda_p$, the plasma density is still in equilibrium, i.e. $n_e = n_0$. As the driver density increases towards $\xi = 0$, the plasma density responds to the electron beam density and starts balancing the driver density. This leads to a reduction of n_e in the presence of the electron beam. The falling edge of n_b marks the minimum of n_e. Plasma electrons are thus out of equilibrium at phases $\xi \approx -\lambda_p/3$, where the driver influence ceases, which causes plasma oscillations trailing the electron beam.

The second case in Fig. 5.1 b) shows the non-linear, or UNDERDENSE regime of wake excitation, where $n_{b,0}/n_0 \geqslant 1$. Resulting plasma properties are still periodic, but now $\lambda_p = \lambda_p(n_{b,0}/n_0)$ increases for larger non-linearities. Furthermore, n_e, E_ξ and ϕ differ significantly from the linear case. The plasma density illustrated in Fig. 5.1 b1) forms peaks, which increase as non-linear and relativistic effects grow. Also, the wake troughs widen and resemble areas of rarefied plasma. The corresponding electric field adapts a sawtooth shape with approximately linear slope. Its zero-crossing marks the minimum of the electrostatic potential ϕ, which exhibits larger phase areas of negative, "binding" potentials per wake period.

Comparing both cases in Fig. 5.1, it is evident that non-linearly excited plasma wakes offer field strengths E_ξ orders of magnitude larger than for linear wakefields, setting superior conditions for rapid acceleration of particles. Moreover, the field distribution is sinusoidal in case of overdense plasma waves and linear in the underdense regime. The latter implies that particles accelerated at different phases ξ experience similar field gradients leading to linear correlation between trapping position and gained energy. This enables advanced schemes for removing this correlation as discussed in Section 5.3. For linear wakefields, in contrast, this correlation is non-linear. Another advantage of non-linear wakes concerns their wake potentials ϕ, which play a key role in particle trapping. To capture particles inside the PWFA it is crucial to have a wide and deep electrostatic potential well. Comparing Fig. 5.1 a3) and b3) one finds that the non-linear wake exhibits a wider range of negative potentials. This promotes particle trapping into the wakefield as discussed in Section 5.3. Because of their superior properties as accelerators, non-linearly excited plasma wakes have been favoured in theoretical and experimental studies since their inception. The following investigations therefore focus on the underdense regime of wake excitation.

5.2 EFFECTIVE WAKE EXCITATION

The process of wake excitation discussed in the previous section can be seen from another perspective, considering that the plasma fluid conserves the system's energy. This energy is provided by the relativistic drive beam situated in regions where $E_\xi > 0$. Consequently,

the driver decelerates and therefore provides the energy sustaining the wake formation. An important figure of merit describing this energy transfer is the TRANSFORMER RATIO [149]

$$T = \left| \frac{E_{\xi,max}}{E_{\xi,min}} \right|, \tag{5.16}$$

which depends on the maximum electric field experienced by the drive beam $E_{\xi,max}$ and the wakefield minimum $E_{\xi,min}$. For longitudinally symmetric drive beams in the linear regime, the transformer ratio is restricted to values $T \leqslant 2$ [29, 83]. In the non-linear regime or for tailored drive beams, however, T can be further increased [29, 88]. This is illustrated in Fig. 5.2, where Eqs. (5.12) to (5.14) are numerically solved for different drive beam density profiles, while keeping similar wakefield structures. The colour-coding reflects the electric fields experienced by the driver at different ξ. Figure 5.2 a1) shows the wake excited by a symmetric Gaussian driver resulting in a transformer ratio $T \approx 1.7$. One finds that the driver front is only weakly affected by the wakefields (light shades), whereas the second half of the beam is subject to large decelerating fields (dark shades), such that it loses energy at higher rates. This affects the beam's phase space throughout propagation and can ultimately impair the beam's ability to excite non-linear wakefields. This can be overcome by asymmetric driver distributions as depicted in Fig. 5.2 a2). Here, the driver density is comprised of a slow, adiabatic rise that transfers energy gently to the wake, followed by a rapid drop that quickly releases the electron displacement. As indicated by the colour-coding, this beam is subject to weaker, much more homogeneous electric fields, which drives the wake more efficiently and potentially over larger distances. Here, $T \approx 4.2$, about twice the achievable result for symmetric drive beams.

As the driver propagates through the plasma and sustains the wakefield, it loses its energy. The length over which the electron beam spends its full energy budget γ_b is termed DEPLETION LENGTH, which approximates to [88]

$$l_{dep} \approx \frac{\gamma_b m_e c^2}{e E_{\xi,min}}. \tag{5.17}$$

For instance, at SLAC FACET $\gamma_b \approx 4 \times 10^4$ and $E_{\xi,min} \approx 10$ GV/m such that $l_{dep} \approx 2$ m. This represent a remarkable length particularly when compared to the depletion length in LWFAs, which is typically of the order of 1 mm [181]. The underdense regime of PWFA therefore poses excellent conditions for rapid acceleration over, compared to LWFA, long distances – the ideal environment to generate particle beams for application in high-energy physics and as light sources.

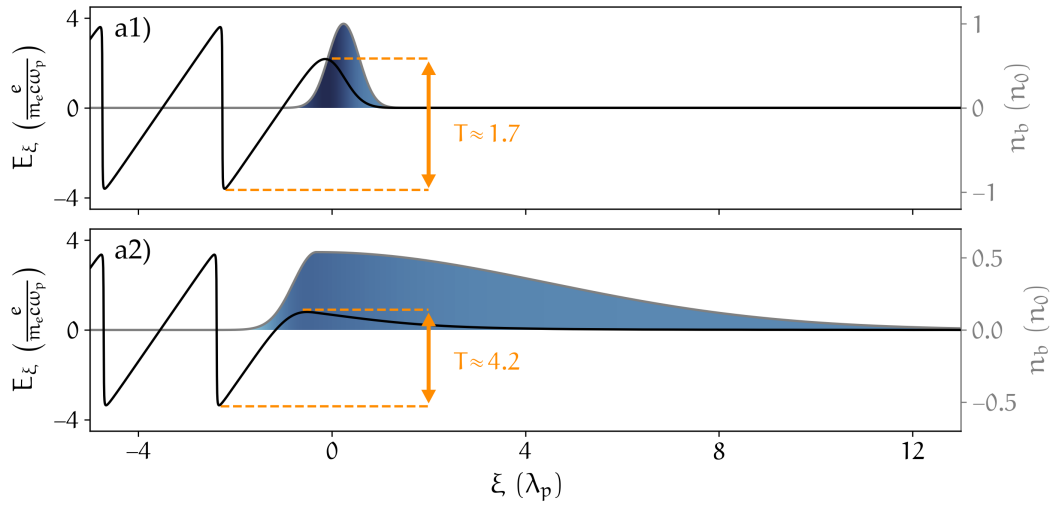

Figure 5.2: Visualisation of the transformer ratio in the 1D fluid approximation. Shown are wakefields (black) excited by different drive beams, which are colour coded blue-black according to the electric fields they sample. a1), Gaussian drive beam with $n_{b,0}/n_0 = 1.00$, $\sigma = 2\,k_p^{-1}$ and a2), double-Gaussian with $n_{b,0}/n_0 = 0.54$, a rising edge $\sigma = 30\,k_p^{-1}$ and falling edge $\sigma = 3\,k_p^{-1}$.

5.3 PARTICLE TRAPPING IN 1D

To harness the plasma wave's strong fields for acceleration, particles have to be placed into phases that support acceleration. Before a detailed discussion of possible injection mechanisms in Chapter 6, the 1D trapping properties of non-linear wakefields are investigated. Therefore, a test particle's motion is studied under the influence of the wake potential $V = -e\phi$. For this, the Hamiltonian formalism is employed in the co-moving co-ordinate system introduced in the previous chapter. In the following, properties of the test electron are denoted with a subscript T. Then, the Hamiltonian takes on the form $\mathcal{H} = \gamma_T m_e c^2(1 - \beta_b \beta_T) - e\phi$ [166]. $\mathcal{H}$ is not explicitly dependent on ξ and therefore describes a constant of motion $\mathcal{H} = \mathcal{H}_0$. Defining $C := (\mathcal{H}_0 + e\phi)/m_e c^2$ the equation can be solved for β_T, such that

$$\beta_T = \frac{\beta_b \pm C\sqrt{\beta_b^2 + C^2 - 1}}{\beta_b^2 + C^2}. \tag{5.18}$$

This equation describes the motion of a test particle with initial energy $\mathcal{H}_0$ in the vicinity of an electrostatic wake potential ϕ and is visualised in Fig. 5.3. Here, a1) shows the potential of a plasma wave driven by an electron bunch. This potential is further used to calculate β_T from Eq. (5.18) for various initial energies $\mathcal{H}_0$ as shown in Fig. 5.3 a2). From this, three distinct sets of trajectories can be identified [18]. Grey trajectories with $\beta_T < 0$ represent electrons that propagate backwards with respect to ξ. On their path they are expelled by the drive beam, partake in the wave formation and are eventually overtaken by the plasma wave. Electrons on grey orbits and $\beta_T > 0$ resemble a motion with higher

energies than the plasma wave, i.e. overtaking the wave from the back. Orange electron paths, on the contrary, describe particles that experience the plasma waves accelerating fields and gain sufficient forward momentum to reach the phase velocity of the wake v_b. These particles remain in the accelerating phase of the wave and are TRAPPED. Trapped and un-trapped trajectories are separated by the SEPARATRIX (black line). Under stable conditions, electrons partaking the plasma wave formation cannot cross the separatrix. However, different techniques have been developed in recent years to facilitate trapping as discussed in Chapter 6.

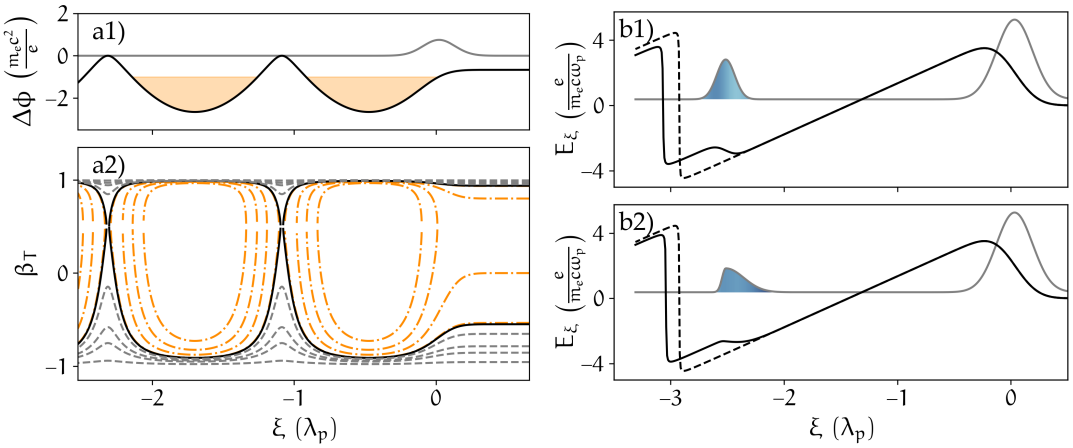

Figure 5.3: Particle trapping and beam loading in the 1D fluid approximation. a1), trapping potential $\Delta\phi$ of the wake (black) excited by a drive beam with $n_{b,0}/n_0 = 0.75$, $\sigma = k_p^{-1}$ (grey). Orange shades visualise regions where the trapping condition Eq. (5.21) for initially resting particles in an ultra-relativistic wake is fulfilled. a2), separatrix (black) corresponding to a1) with free orbits (grey) and trapped orbits (orange). Note that β_T describes the longitudinal velocity component relative to the co-moving frame of reference. b), Un-loaded wakefields (dashed black) are modulated (solid black) due to the presence of a witness beam, which are colour coded blue-black according to the electric fields they sample. The drive beam features $n_{b,0}/n_0 = 2$ and $\sigma = k_p^{-1}$. The witness beam is comprised of a Gaussian with $n_{b,0}/n_0 = 1$, $\sigma = k_p^{-1}/2$ in b1) and a double-Gaussian with $n_{b,0}/n_0 = 0.6$, a rising edge $\sigma = k_p^{-1}$ and falling edge $\sigma = k_p^{-1}/5$ in b2).

The constant of motion $\mathcal{H}_0 = \gamma_T m_e c^2 (1 - \beta_b \beta_T) - e\phi$ offers additional perspectives on particle trapping. Considering the test particle's initial properties $\gamma_{T,i}$, $\beta_{T,i}$ at corresponding ϕ_i and its final values $\gamma_{T,f}$, $\beta_{T,f}$, ϕ_f, the potential difference can be introduced as $\Delta\phi = \phi_f - \phi_i$. In order to achieve trapping, the electron has to catch up with the wake, i.e. $\beta_{T,f} \geqslant \beta_b$ and $\gamma_{T,f} \geqslant \gamma_b$ until it reaches the maximum of the potential $\phi_f = \phi_{max}$. Then, the 1D TRAPPING CONDITION reads [122]

$$\frac{e}{m_e c^2}\Delta\phi \leqslant \frac{1}{\gamma_b} - \gamma_{T,i}\left(1 - \beta_b \beta_{T,i}\right). \tag{5.19}$$

Depending on the particle's initial conditions and the properties of the wakefields, Eq. (5.19) defines the respective TRAPPING REGION. As an example, particles initially at rest $\beta_{T,i} \approx 0$ yield [129]

$$\frac{e}{m_e c^2}\Delta\phi \leqslant \frac{1}{\gamma_b} - 1. \tag{5.20}$$

As expected, trapping occurs more easily for low-energy drive beams $\gamma_b = (1-\beta_b^2)^{-1/2}$, i.e. lower beam velocities β_b and associated phase velocities of the wake. The limit for ultra-relativistic drive beams takes on the form [130]

$$\frac{e}{m_e c^2}\Delta\phi \leqslant -1. \tag{5.21}$$

This trapping condition is visualised in Fig. 5.3 a1) as shaded regions. Electrons that are released in these regions, e.g. by tunnelling ionisation, gain sufficient energy while slipping to the back of the wake to remain within the plasma wake. This example highlights the advantage of employing non-linear plasma waves as particle accelerators, as they feature wide and deep potential wells that promote particle trapping, as opposed to the linearly excited wakefields (cf. Fig. 5.1 a3) and b3)).

These models apply to injection mechanisms that leave the structural integrity of the plasma wave intact, such as ionisation injection and the plasma photocathode (see Section 6.1). Other mechanisms, e.g. the density downramp injector, require a multidimensional treatment including evolving plasma waves as outlined in Section 6.3.

After trapping of particles, they accumulate in the accelerating portion of the wakefield and form the WITNESS BEAM. Such beams can maintain their phase position inside the PWFA once they are relativistic $\gamma \gg 1$ and can gain high energies. For dense beams containing large numbers of particles, however, the beam affects the wakefield formation as evident from Gauss' law in Eq. (2.1) with $n_b \to n_b + n_w$. The impact of the witness beam density n_w on the wakefields is termed BEAM LOADING [174, 184] and is illustrated in Fig. 5.3 b) using the fluid model Eqs. (5.12) to (5.14). This figure outlines this concept for one wake formation loaded by two exemplary witness beam distributions. The field values sampled by the witness beam are colour-coded similar to Fig. 5.2. Panel b1) displays beam loading for a Gaussian witness beam distribution and its effect on the electric field. The wake period extends slightly and a local field maximum forms in the witness beam region. This affects the acceleration of the witness beam: it is subject to stronger acceleration at the front (light shades) compared to reduced accelerating fields at the back (dark shades). Ultimately, this leads to the correlation of energy and phase ξ and is called LONGITUDINAL PHASE SPACE CHIRP [107]. However, such correlation limits the applicability of particle beams, e.g. due to chromatic effects during the beam transport [7] downstream of the plasma stage. Various techniques have therefore been developed to mitigate these effects,

e.g. by controlled loading of the wake [107]. For example, generating a witness beam with adiabatically increasing and subsequent rapid falling density distribution, as illustrated in b2), can flatten the accelerating field experienced by the witness beam to avoid phase space chirps in the first place. This beam may then accelerate homogeneously as can be seen from the approximately constant shade. A similar technique can be used to remove the phase space chirp of a low-density beam by injecting a second, high-density beam [107]. This ESCORT BEAM then locally reverts the field slope in regions of the witness beam and can be used to minimise the energy spread of the witness beam. The controlled generation of multiple witness beam populations by the plasma torch injector is outlined in Section 9.5 and may be employed for tailoring of plasma wakefields in the future.

5.4 WAKE EXCITATION IN 3D AND THE BLOWOUT REGIME

The previous discussions focused on longitudinal wake excitation based on the 1D fluid model. The reality, however, deviates from this simplified treatment as all spatial dimensions have to be taken into account. While basic 1D scales such as the plasma period λ_p still give reasonable approximations, other formalisms have to be found to characterise 3D wakefields. However, fully dimensional theories still prove elusive, such that 3D wakefields are commonly investigated with the help of phenomenological models such as [93, 100, 102, 165, 170] or 3D PIC simulations (cf. Section 7.1). The former provides basic scalings for idealised conditions, whereas the latter offers the advantages to implement arbitrary plasma geometries and asymmetric drive beams. PIC simulations further capture the evolution of the PWFA through the plasma and allow for investigating various injection mechanisms.

Analogous to $n_{b,0}/n_0$ in the 1D treatment outlined in Section 5.1, the NORMALISED BEAM CHARGE can be defined [148]

$$\tilde{Q} = \frac{N_b k_p^3}{n_0}. \tag{5.22}$$

It accounts for 3D effects by comparing the number of beam electrons N_b and plasma electrons that occupy a cubic plasma skin depth and characterises the degree of non-linearity of the beam-plasma interaction. $\tilde{Q} < 1$ describes linear interactions and $\tilde{Q} > 1$ characterises a non-linear plasma response. However, the transverse dimensions in 3D plasma waves additionally facilitate the BLOWOUT REGIME for $\tilde{Q} \gg 1$ [147] as visualised in Fig. 5.4. Here, the drive beam expels all plasma electrons on its path to form a pure ion cavity in its wake. The oscillating electrons then form a dense sheath surrounding the ion cavity and shield the ions to the exterior. This separation of plasma electrons and

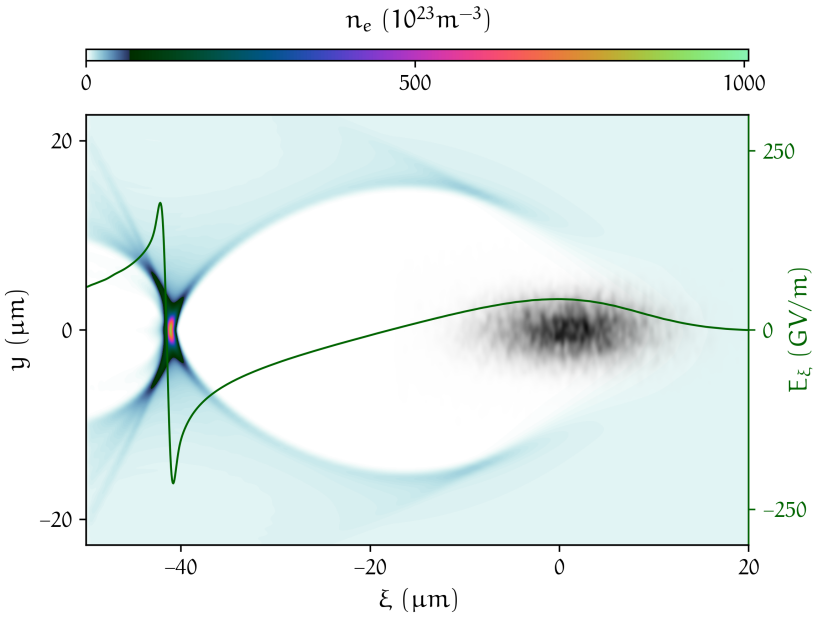

Figure 5.4: 3D PIC simulation of the blowout regime in the frame co-moving with the electron beam $\xi \approx x - ct$. The electron drive beam (black) propagates to the right and fully cavitates the electron plasma density n_e in its wake. The charge separation results in strong accelerating fields E_ξ.

ions generates strong electromagnetic fields. Within the ion cavity, the accelerating fields scale approximately as [102]

$$E_\xi = \frac{m_e \omega_p^2}{2e} \xi, \tag{5.23}$$

for short and ultra-relativistic drive beams. Due to the strong scaling with the plasma frequency, accelerating fields of the order of GV/m are readily available for plasma densities exceeding 10^{21} m^{-3} allowing for rapid energy gain of trapped particles and compact accelerator designs. Remarkably, Eq. (5.23) depends only on the longitudinal co-ordinate, such that all particles occupying the same ξ experience the same energy gain regardless of their transverse distribution. The energy spread of witness beams is therefore decoupled from transverse effects in the blowout regime.

Equation (5.23) directly links to the transverse fields in the blowout via the PANOFSKY–WENZEL THEOREM [131, 145] that relates longitudinal forces F_ξ and focusing forces F_r in isolated cavities

$$\frac{\partial F_\xi}{\partial r} = \frac{\partial F_r}{\partial \xi}. \tag{5.24}$$

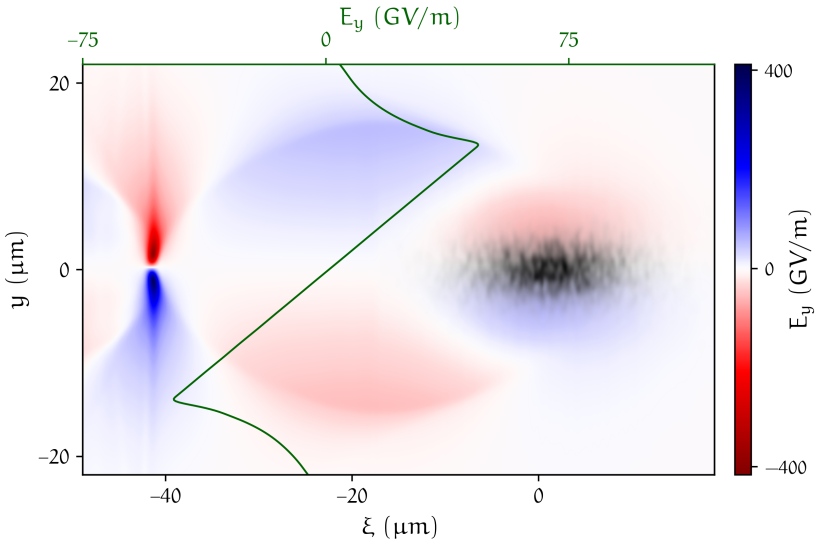

Figure 5.5: 3D PIC simulation of the transverse electric fields in the the blowout regime. Shown are the strongly focusing, approximately linear transverse electric fields E_y.

Combined with Eq. (5.23), this equation implies that focusing forces in the blowout remain constant for varying ξ, i.e. $F_r = m_e\omega_p^2 r/2$ [102]. The radial electric fields inherit the linear scaling

$$E_r = \frac{m_e\omega_p^2}{4e} r, \tag{5.25}$$

as visualised in Fig. 5.5. The linearity of E_r and F_r promotes the focusing and guiding of particles that are trapped in the wakefield. Moreover, it ensures the emittance preservation throughout the acceleration process and thus supports the production and acceleration of high-quality electron beams.

Above considerations assumed a homogeneous plasma to support the wake excitation. However, in experiments this may be violated particularly when elaborate focusing optics and a limited laser energy budget restrict the generation of ideal plasma channels [44, 68]. In this case, the wake excitation is compromised by the plasma channel geometry as discussed in the context of injection experiments at SLAC FACET in Chapter 8.

6 INJECTION MECHANISMS

The previous chapter investigated the excitation of non-linear plasma wakes, which feature excellent conditions for acceleration of high-quality electron beams. However, to utilise these structures as accelerators, a particle population must be trapped in the accelerating phase of the plasma wave to transfer its energy to this WITNESS BEAM. As discussed in Chapter 4, the quality of the produced beams strongly depends on its initial conditions and therefore on the employed mechanism for trapping. In this chapter the most important injection methods for PWFAs are summarised.

6.1 CLASSIFICATION OF INJECTOR CONCEPTS

Particle injection in PWFAs can be achieved by two general approaches. In EXTERNAL INJECTION, a pre-accelerated witness beam originates from a source other than the plasma, e.g. a linac. This scheme has been shown to enable acceleration of beam tails of long drive beams extending into the accelerating phase [14] and for longitudinally spaced double bunches as result from splitting the drive beam in two parts [84, 99, 146]. Utilising a fraction of the driver as witness beam overcomes the issue of synchronising both beams. However, aligning both beam orbits remains challenging due to spatial offsets and pointing variations of the trailing beam. Moreover, the tunability of this approach is limited and relies on external generation of high-quality electron beams, which is a research area in its own right.

The second category for particle trapping in PWFAs facilitates injection of particles that originate from the plasma stage and hence can be summarised as INTERNAL INJECTION. Various techniques have been proposed in the last decades which exploit different mechanisms. One class of injectors utilises gas compositions for selective ionisation as outlined in Section 3.2. Here, a gas with low ionisation threshold, such as hydrogen, provides the plasma for wake excitation. A second component, e.g. helium, serves as reservoir for additional plasma electrons that are liberated by strong electric fields via ionisation. These fields may originate from the drive beam, witness beam, or the plasma wake [5, 113, 129, 176] and therefore strongly depend on the evolution of the PWFA. These mechanisms for ionisation injection are thus hard to control and typically lead to continuous injection over long distances, which produces witness beams of large energy spread. However, the ideal case would include the controlled and LOCALISED injection that is de-coupled from the PWFA.

This can be achieved by the PLASMA PHOTOCATHODE concept [44, 74]. It requires a PWFA free from dark current, i.e. no unwanted trapping by other means, and a strongly

driven wake that fulfils the trapping condition in Eq. (5.21). If this is established, a dedicated laser pulse is focused along the driver orbit into the blowout. Once this laser exceeds the threshold for tunnelling ionisation of the second gas component, electrons are released within the wakefield and trapped. Utilising moderate lasers with $a_0 \ll 1$ ensures negligible initial momenta of the photo electrons (cf. Section 3.3) and allows for producing beams with normalised emittance values as low as tens of $nm\,rad$ [107] for strong focusing. However, experimental realisation of the plasma photocathode is a challenging endeavour as it requires precise spatio-temporal alignment of the injector laser with respect to the driver beam axis. Its first experimental installation has therefore been conducted in 90° geometry, where the injector laser has been focused perpendicularly to the driver beam axis [44]. This first implementation at SLAC FACET additionally gave the opportunity to investigate the plasma torch mechanism, a de-coupled and localised injector that relies on wave breaking.

6.2 WAVE BREAKING AS PARTICLE INJECTOR

Wave breaking commonly refers to different processes that can temporarily harm the structural integrity of the plasma wake. Typically, one distinguishes longitudinal, or 1D wave breaking, and transverse wave breaking, which requires the multi-dimensional description of the plasma. It is important to note, that both processes can occur in 3D plasma waves [34]. Nevertheless, both differ qualitatively and describe separate physical pictures [66, 101]. This is often confused and leads to misconceptions, especially due to the lack of a terminology describing transverse wave breaking. The following section elaborates on important aspects of wave breaking for the localised injection of particles into plasma wakes.

LONGITUDINAL WAVE BREAKING in cold, non-relativistic plasma has already been studied in the 1950s by Dawson [42]. He found that stable plasma oscillations only occur for field amplitudes below the wave breaking limit $E_{WB} = m_e c \omega_p / e$ [143]. When exceeding this value, the 1D oscillations become multi-valued and different charge "sheets" cross. Figure 6.1 a) visualises a regular sinusoidal (solid line) and a multi-valued, incoherent plasma oscillation (dashed line). This limit also applies to plasma waves excited by laser or electron drive beams. In this context, wave breaking compares to the breaking of water waves, or the adiabatic breaking of the wave crest that collapses towards the wave trough as exploited for surfing. For plasma waves, wave breaking implies that the wave crest and wave trough overlap as indicated by Fig. 6.1 a), such that a fraction of electrons located at the crest find themselves in the accelerating phase of the plasma wave. Deliberate triggering of wave breaking can therefore be harnessed for particle injection into plasma wakes.

Akhiezer and Polovin's theory [3] allows for deriving a cold, relativistic expression of the wave breaking limit by solving the homogeneous part of Eq. (5.12) via elliptical integrals. The resulting maximum electric field reads [143]

$$E_{WB,r} = E_{WB}\sqrt{2(\gamma_{max} - 1)}, \tag{6.1}$$

where γ_{max} denotes the maximum gamma factor of the plasma fluid associated with the phase velocity of the wake. Equation (6.1) shows that relativistic plasma waves $\gamma_{max} \gg 1$ can sustain much higher field values before breaking compared to non-relativistic plasma waves.

Based on these early results, investigations have been extended towards non-relativistic warm wave breaking [32] and relativistic, warm plasmas [89, 123, 156]. For instance, ultra-relativistic $\gamma_{max} \gg 1$, thermal plasmas feature reduced wave breaking limits $E_{WB,th} \approx E_{WB}(4m_e c^2/27k_B T)^{1/4}$ [143, 158] due to the thermal distribution of the plasma and the resulting diminished coherence of the plasma waves.

The outlined breaking criteria generally apply to both, laser and electron beam-driven wakefield accelerators. However, each approach implies different environments. For instance, $E_{WB,r}$ depends on γ_{max}, which is determined by the plasma density and the group velocity of the driver. For laser drivers, the group velocity $v_g = c\sqrt{1 - \omega_p^2/\omega_L^2} < c$, whereas typical electron beam drivers exhibit $v_g \approx c$ [76]. Wave breaking therefore occurs more easily in LWFAs. Furthermore, typical lasers employed for LWFA generate hot plasma due to their large normalised vector potential $a_0 \geqslant 1$ (see Section 2.1), which additionally reduces the threshold for wave breaking as indicated by $E_{WB,th}$. Longitudinal wave breaking thus occurs at lower wakefield amplitudes in laser-driven wakes, whereas PWFAs can operate in cold pre-ionised plasma using ultra-relativistic electron beams, such that $E_{WB,r}$ and $E_{WB,th}$ indicate the onset of 1D wave breaking at larger wake amplitudes.

A quantitative theory describing MULTI-DIMENSIONAL WAVE BREAKING derived from first principles still proves elusive, such that Dawson's approach of sheet crossing [42] has been adopted for transverse effects. With the onset of 2D PIC simulations it soon became evident that transverse effects can lead to cold wave breaking at field values below $E_{WB,r}$ as observed by Bulanov [20]. He deduced that the transverse distribution of strong relativistic drivers produce wakefields with phase curvature $1/\rho$ and strong transverse wake amplitudes $\alpha(y_0)$. This may occur due to relativistic mass increase as function of the transverse co-ordinate y, which produces the local plasma frequency $\omega_p = \omega_p(y)$ [22]. This motivated the investigation of transverse driver distributions of width σ_y leading to $\omega_p(y) \approx \omega_p + \Delta\omega_p(y/\sigma_y)^2$, where the wakefield describes a parabolic shape. This results in contours of constant wake phase that obey [21]

$$x = \frac{y_0^2}{2\rho} + \alpha(y_0)\frac{\rho}{\sqrt{\rho^2 + y_0^2}}, \quad y = y_0 - \alpha(y_0)\frac{y_0}{\sqrt{\rho^2 + y_0^2}}, \tag{6.2}$$

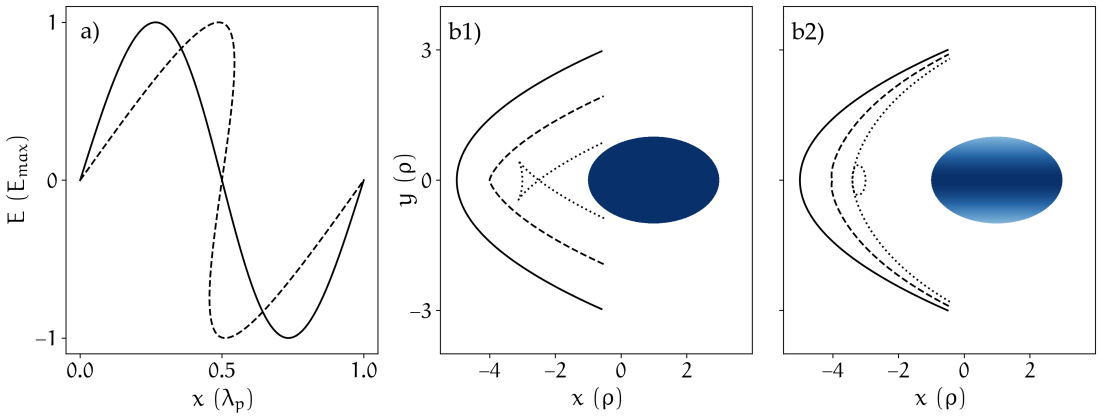

Figure 6.1: Longitudinal and transverse wave breaking. a), normalised field distribution of regular (black line) and multivalued plasma oscillation (dashed line) indicating longitudinal wave breaking. b), lines of constant wake phases for different transverse wake profiles $\alpha(y_0)$ as derived in [21], where transversally multi-valued regions indicate the onset of transverse wave breaking. Blue indicates the position of a generic drive beam. b1), wake phases for uniform driver amplitudes $\alpha = 0, \rho, 2\rho$ visualised as solid, dashed and dotted line, respectively. b2), wake phases for Gaussian wake distribution $\alpha(y_0) = \alpha_0 \exp\left(-y_0^2/4\rho^2\right)$ with $\alpha_0 = 0, \rho, 2\rho$ displayed as solid, dashed and dotted line.

Figure 6.1 b) illustrates Eq. (6.2) for two cases, where an exemplary driver is shown in blue (not to scale) and solid black lines correspond to $\alpha_0 = 0$, i.e. the unperturbed parabolic phase fronts. b1) further includes the wake phase for constant $\alpha(y_0) = \alpha_0 = \rho, 2\rho$ (dashed and dotted line, respectively), whereas the latter substantially changes its appearance forming a SWALLOW TAIL structure, which further develops for $\alpha_0 \gg \rho$. The phase fronts are no longer transversely single-valued and thus indicate the onset of transverse wave breaking originating from strong wake amplitudes. Figure 6.1 b2) further visualises the phase fronts for $\alpha(y_0) = \alpha_0 \exp(-y_0^2/4\rho^2)$ with $\alpha_0 = 1, 2$ (dashed and dotted line, respectively). Here, the multi-valued signatures extent inside the closed phase fronts and form a PHASE LOOP as a result of strong wake amplitudes in addition to its transverse distribution.

To achieve particle trapping into plasma waves, however, wave breaking alone does not suffice. The breaking electron population indicated by the multi-valued regions in Fig. 6.1 a) and b) must additionally be enclosed by the plasma wake and accelerate to its local phase velocity in order to remain within the plasma wave. The combined wave breaking and capturing of electrons can be facilitated by expansion of the plasma wave, which can be achieved in two ways. The first scheme triggers the evolution of the wakefields for constant plasma densities, e.g. due to the evolution of the driver, and is termed SELF-INJECTION [34]. This is a typical injector for LWFAs, where laser-plasma interactions cause strong wake evolution sufficient for wave breaking and injection of electrons. However, the beam evolution in relativistic PWFAs occurs over much longer time scales due to the high group velocity $v_g \approx c$ and renders this mechanism impractical for injection. Wake expansion and injection can also be achieved by longitudinal density

gradients and is named DENSITY DOWNRAMP INJECTION [23, 166]. It allows for controlled and localised electron trapping in laser and particle-beam driven wakefield accelerators alike and is discussed in the following.

6.3 DENSITY DOWNRAMP INJECTION

The density downramp injector has been proposed 20 years ago for LWFA [23] and PWFA [166] and therefore offered one of the first CONTROLLABLE and LOCALISED injection mechanisms in wakefield accelerators. This scheme employs negative gradients of the plasma density, which trigger localised expansion of the wakefield and wave breaking at the same time. The breaking particle population is then enclosed by a newly forming plasma wake and can gain sufficient energy to remain within the plasma wave. The expansion and the interaction of plasma electrons with the dynamic wake formation can be studied similar to [86, 94] and in analogy to the 1D Hamiltonian approach in Section 5.3. Time, space, velocities, electromagnetic fields and potentials are normalised to ω_p^{-1}, k_p^{-1}, c, E_{WB} and $e/m_e c^2$ in the following. Additionally, the Hamiltonian $\mathcal{H} = \sqrt{1+(\vec{P}+\vec{A})^2} - v_b P_x - \phi$ is employed in the co-ordinate system moving with the drive beam $\xi = x - v_b t$. The potentials inside the plasma wake can be obtained from a phenomenological model $A_\xi = -\phi = (\xi^2 + y^2 - R^2)/8$ [93], which approximates the plasma wake as a sphere with radius R. Then, the electric field obeys Eqs. (5.23) and (5.25). To investigate the dynamics on density downramps, expanding wakes $R = R(t)$ are studied, such that the full set of equations of motion for a test particle read [93]

$$\begin{aligned}
\dot{p}_x &= -\frac{1}{4}\left[\xi(1+v_b) - \frac{y p_y}{\gamma} + R\dot{R}\right], \\
\dot{p}_y &= -\frac{1}{4} y (1 + \frac{p_x}{\gamma}), \\
\dot{\xi} &= \frac{p_x}{\gamma} - v_b, \\
\dot{y} &= \frac{p_y}{\gamma},
\end{aligned} \tag{6.3}$$

where $\dot{}$ denotes the differentiation with respect to t and $\dot{R}$ accounts for the expansion of the blowout. Figure 6.2 shows results from numerical integration of Eq. (6.3), where a) illustrates the plasma wave propagating to the right at v_b with $\gamma_b = (1 - v_b^2)^{-1/2} = 20 \times 10^3$ corresponding to approximately 10 GeV as expected at SLAC FACET II [191]. Dashed grey circles indicate the initial radius R_i and the final radius R_f of the linearly expanding wake and the solid black circle represents the blowout boundary at the particular instance in time. The trajectories of test electrons that are initially at rest and positioned at various $y_0 = y(t = 0)$ are computed representing the constituents of the plasma density at these locations. The resulting trajectories are shown in the co-moving frame of reference in black (un-trapped electrons) and green (trapped electrons).

Figure 6.2 a1) visualises one snapshot at $t \approx 2$, i.e. shortly after the plasma wake started expanding. Here, electrons are outside the influence of the wakefield and move towards the rear of the plasma wave. This changes in Fig. 6.2 a2), where two electron trajectories coloured in green cross the expanding boundary and find themselves under the influence of the wakefield. These electrons respond to the fields and accelerate towards the wake centre as can be seen in Fig. 6.2 a3), where the trajectories cross between $\xi \approx -R_i$ and $\xi \approx -R_f$. On their path through the blowout, the trapped test particles rapidly reach relativistic velocities as visualised by v_x in Fig. 6.2 b) and remain within the plasma accelerator. Figure 6.2 b) further visualises the evolution $y(t)$ of one trapped electron trajectory featuring betatron oscillations. These occur naturally for steep downramps due to the injection from the wake sheath in addition to the strong focussing wakefields and hence highlight one prominent application of such beams as radiation source [33].

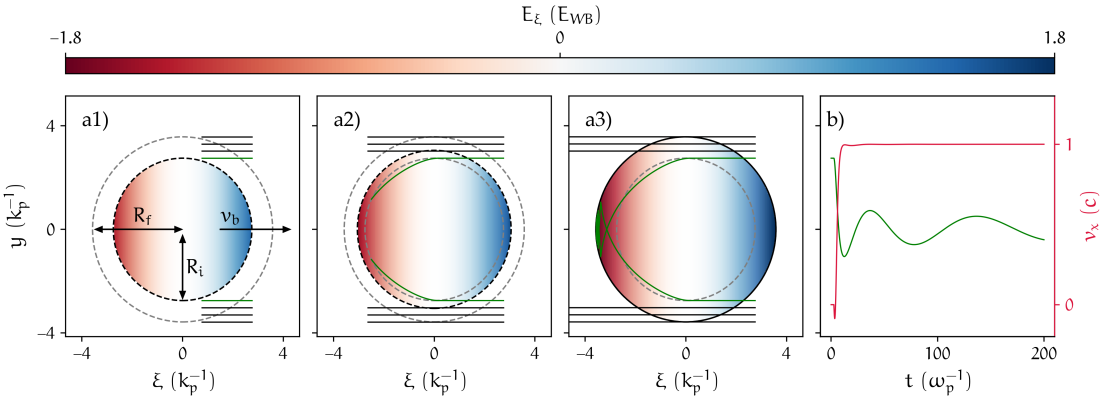

Figure 6.2: 2D particle trapping by an expanding blowout. Shown are the numerical solutions of the equations of motion Eq. (6.3) as proposed in [86, 94] for $\gamma_b = 20 \times 10^3$. a1) to a3), real space visualisation of the temporal evolution of a spherical blowout with initial radius $R_i = 2.75$ (inner dashed circle) and final radius $R_f = 1.3\,R_i$ (outer dashed circle). The solid circle marks the momentary position of the expanding blowout boundary. Un-trapped and trapped trajectories are coloured in black and green, respectively. b), temporal evolution of the transverse co-ordinate $y(t)$ (green, left axis) and the particle's longitudinal velocity v_x (red, right axis) of one particle shown in a).

The crossing point of the trajectories in Fig. 6.2 a) suggest that the length of the generated electron beam scales $\propto R_f - R_i$, which can be controlled by the difference of the density transition. Thompson et al. confirms this scaling [171] and further concludes that the witness beam emittance is proportional to $\lambda_p \propto n_p^{-1/2}$ indicating the generation of high-quality electron beams for increased plasma densities.

The trajectory crossing in Fig. 6.2 a3) further resembles the manifestation of the SWALLOW TAIL structure assumed by the breaking wake phases illustrated in Fig. 6.1 and demonstrates the effect of transverse wave breaking. It further marks the rapid regime of density downramp injection, where a wake fraction collapses transversally while the wake sheath re-forms enclosing the breaking population. This typically occurs for downramps shorter than the plasma period [50]. For long downramps $> \lambda_p$, in contrast,

adiabatic processes govern the particle trajectories and lead to injection at the vertex of the expanding wake, i.e. on the wake axis. Both regimes are studied in more detail in Section 9.1.

First successful density downramp experiments have been implemented in LWFAs. Here, the density transition has been generated by various means. One approach utilises an intense laser pulse to produce hot plasma columns on the path of the plasma wake [15, 30, 54]. This plasma expands and produces a local imbalance of the plasma electrons and ions and hence forms a density transition. Another approach exploits the density downramps inherent to single or multiple gas jets [59, 64, 72]. The current state-of-the-art employs gas shocks created by inserting blades or wires into the flow of a supersonic gas jet [10, 19, 25, 154, 169] and experimental results indicate electron beams of improved transverse quality compared to ionisation injection [10].

Despite extensive theoretical and numerical efforts [67, 114, 190, 195], downramp injection by these hydrodynamic schemes still prove elusive in PWFA experiments. On one hand, this is, compared to LWFA, due to the limited number of available PWFA facilities. On the other hand, the high phase velocity of beam-driven plasma wakes demand for strong density gradients, which remain a technical challenge for the hydrodynamic schemes outlined above. However, the PLASMA TORCH INJECTOR [187, 188] readily meets these criteria and is discussed in the following section.

6.4 THE PLASMA TORCH INJECTOR

The plasma torch scheme benefits from the moderate electric field strengths inherent to particle drivers in PWFA. This allows for employing gas compositions as plasma source to enable SELECTIVE IONISATION, which is outlined in Section 3.2 and requires two or more ionisation states. One component features a low ionisation threshold, such as hydrogen, which is ionised by a dedicated pre-ionisation laser and then serves the dark current free wake excitation by the drive beam. Conversely, the second gas component, e.g. helium, is unaffected by the pre-ionisation and the wakefield. It remains in its initial state for large regions of the PWFA. Only regions where another laser pulse, the TORCH LASER, exceeds the threshold for tunnelling ionisation of this component, are populated by a localised density spike, the PLASMA TORCH [187, 188]. To obtain short density downramps from the non-linear behaviour of the ADK rates, the torch laser can be focused perpendicularly to the drive beam axis.

Figure 6.3 a) illustrates an exemplary longitudinal density profile including the different sections of the plasma torch PWFA, in addition to respective snapshots from 3D PIC simulations in Fig. 6.3 b). The drive beam propagates to the right and is coloured blue. It excites a plasma wave in the blowout regime (green) that is sustained by the plasma channel density n_{ch}. The torch laser exhibits moderate laser properties such as $a_0 \ll 1$ and arrives before the PWFA to generate a cold density spike $n_T(\vec{r}, t)$ (orange)

centred at $x = x_T$. The torch density $n_T(\vec{r}, t)$ adds to the ambient plasma channel density and evolves on time scales much larger than the scales inherent to the PWFA as discussed in Section 3.3. This assures constant conditions for localised injection and sets relaxed timing requirements between the drive beam and the torch laser. After injection, electrons remain phase-locked within the accelerating portion of the wakefield as illustrated in Fig. 6.3 b3) and can gain high energies due to the dephasing-free PWFA.

The plasma torch scheme offers various means to control the properties of the density gradient. For instance, changing the mix of both gas components allows for varying the peak density of the plasma spike $n_{T,0}$. At the same time, the focus position of the torch laser x_T controls the acceleration length and therefore the energy of the produced particle beam. Changing other properties of the torch laser, such as its spot size w_0, or energy ε_L produces different distributions $n_T(\vec{r}, t)$ that affect various aspects of the injection process as discussed in Chapters 8 and 9.

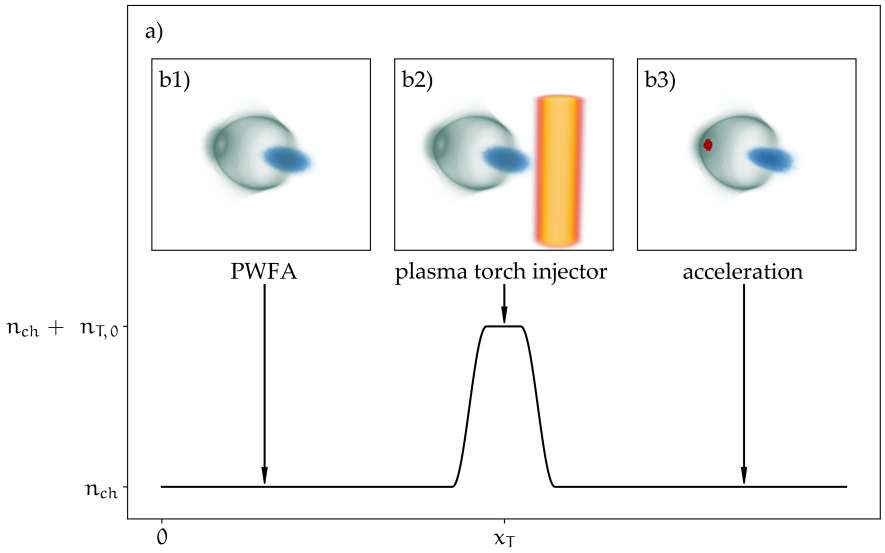

Figure 6.3: Principle of the plasma torch PWFA. a), exemplary longitudinal density profile that scales with the density of the plasma channel n_{ch} and the peak density of the plasma torch $n_{T,0}$. b), visualisation of the main sections of the plasma torch PWFA from 3D PIC simulations. b1), the drive beam (blue) propagates to the right and excites a plasma wave in the blowout regime (green). b2), injector section, where the plasma torch is optically generated (orange) before the arrival of the PWFA. Interaction of the plasma torch and the plasma wake triggers localised injection of electrons. b3), injected electrons are locked in the accelerating phase of the PWFA (red) and gain energy.

Advanced density downramp injectors in LWFA employ shock fronts by obstructing the flow of a gas nozzle [10, 19, 25, 154]. While this scheme can produce density gradients on scales similar to the plasma torch technique, they differ fundamentally in their practical use and conceptual applicability. For instance, the creation of shocks involves intricate secondary effects and hydrodynamic processes that re-arrange gas volumes to deviate from their homogeneous character. These processes are difficult to control and further depend on hardware properties, such as the blade-coverage, nozzle design

and the backing pressure of the nozzle [169, 173]. Here, numerical modelling of the hydrodynamics is inevitable for understanding the resulting density distributions, or even tailor desired profiles [53, 179]. In contrast, tunnelling ionisation by mJ-class lasers is straightforward and benefits from the flexibility of optical systems.

Another aspect concerns the localisation of the injector. Shock-generated gas distributions perturb the entire longitudinal density distribution [169, 173], including the section before the injector and the acceleration section. This COUPLING to the wakefield accelerator limits the flexibility of the injector. On one hand, perturbations upstream of the injection position complicates the matching of the driver to the plasma and therefore affects the wake evolution until the injector. This, in turn, affects the conditions present at the injection position and can vary the injection process dependent on the injector settings. On the other hand, the inhomogeneous plasma density downstream of the injector causes the variation of the wake formation and fields, such that the injector couples to the energy gain of the witness beam. Conversely, the plasma torch simply adds to the plasma channel density and thus resembles a localised perturbation of the PWFA, i.e. leaves up- and downstream sections unaffected.

One conceptual difference regards the involved geometries. On the scale of the wakefield, density downramps generated by shocks feature longitudinal gradients, i.e. are axially symmetric with respect to the driver orbit. On the contrary, the plasma torch scheme provides 4D control over the density profiles governed by the generating laser pulse. In principle, this allows for designing plasma spikes by elaborate focusing, the use of multiple torch lasers, or by exploiting the timing-dependent generation of the plasma spike. This is unique to the plasma torch injector and provides novel opportunities for manipulating the generation of electron beams as investigated in Chapter 9.

7 METHODOLOGY

Most dynamics relevant for the present work rely on the interaction of numerous particles involving non-linear electrodynamic processes. Of these, only few idealised cases are analytically tractable, such that studying injection processes into 3D plasma wakes makes computer simulations indispensable. This is backed by the ever-increasing availability of resources for high-performance computation in combination with established highly parallelised codes and therefore provides the vital tools for bridging the gap between experiments and theory.

7.1 PARTICLE-IN-CELL SIMULATIONS

The most common tool for investigating plasma interactions are particle-in-cell codes (PIC) [56]. Many different manifestations have been developed over the past decades, all of which can be categorised by their dimensionality and the involved set of differential equations. The former includes 2.5D, or quasi-3D, codes, which apply to cylindrically symmetric systems, such as plasma wakes excited by symmetric driver beams. These codes achieve significant speedup over full 3D codes and therefore allow for computationally efficient investigations. However, to model systems that break the radial symmetry, such as the plasma torch injector, 3D codes are inevitable. The number of dimensions determines the complexity of the set of differential equations used for the PIC code, which further specifies physical assumptions. For instance, quasi-static codes solve Poisson's equation, which excludes temporal evolution of the simulated system and allows for efficiently solving electrostatic systems. However, this prohibits investigating dynamic processes, such as downramp injection in wakefield accelerators, which rely on dynamic accelerator structures and thus requires full electromagnetic codes. These codes solve the general form of the Maxwell equations containing all spatio-temporal information. This comes for the price of computational costs, but allows for computing systems of arbitrary geometry. Below, the general concept of 3D electromagnetic PIC codes is presented following [56, 118, 178].

3D PIC algorithms operate in cycles that span over simulation time steps Δt and include several calculations as illustrated in Fig. 7.1. Particles enter the PIC cycle through their 6D phase space $\vec{r}(t)$, $\vec{p}(t)$. To avoid unfeasible computation of 10^{18} or more particles that are typical for PWFAs, N_{ppm} physical particles are bundled to MACRO PARTICLES. These are further treated as Lagrangian elements, i.e. they describe discrete point clouds as function of the simulation time as opposed to distributions that are mapped to a numerical grid. This bears several advantages. For instance, unpopulated phase space

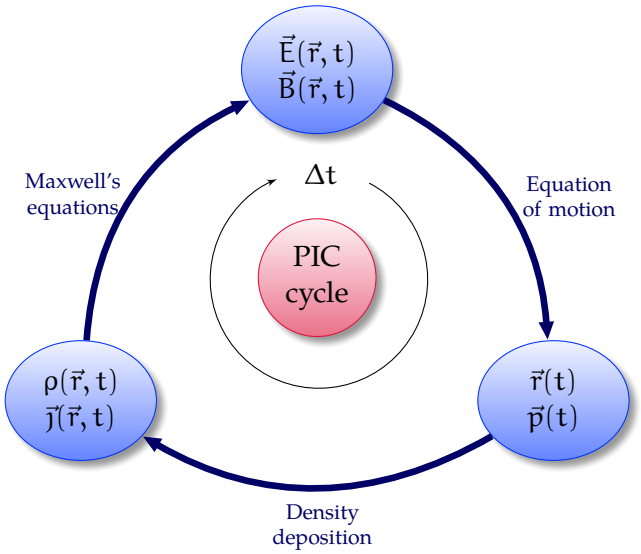

Figure 7.1: Particle-in-cell cycle.

regions occupy no memory and lead to enormous computational speedup. Furthermore, this avoids a six-dimensional phase space grid and allows for handling large numbers of macro particles.

The Lagrangian approach to particles in PIC simulations demands the next step in the PIC cycle, the DENSITY DEPOSITION. During this process, the particle's phase space $\vec{r}(t)$, $\vec{p}(t)$ is interpolated onto the numerical grid to yield the density distribution $\rho(\vec{r},t)$ and the current density distribution $\vec{j}(\vec{r},t)$. This step hence initialises the Eulerian section of the PIC cycle, which is defined on a numerical grid. This grid is commonly formed of the Yee lattice [193], which involves the discretisation of space into cells of length Δx, Δy and Δz. In this scheme, electric fields E_x, E_y, E_z are defined on the edges of these cells as visualised in Fig. 7.2. In contrast, magnetic fields B_x, B_y, B_z and current densities j_x, j_y, j_z are defined on the faces of these cells. This allows for efficient integration of the Maxwell equations using the Leapfrog algorithm and yields the distribution of the (updated) electric field $\vec{E}(\vec{r},t)$ and the magnetic field $\vec{B}(\vec{r},t)$. Resulting fields are typically smoothed before further use to avoid numerical noise and discontinuities.

The next step is the PARTICLE PUSH, which calculates the new particle positions $\vec{r}(t+\Delta t)$ and momenta $\vec{p}(t+\Delta t)$ based on the integration of the equation of motion via the Leapfrog algorithm. Due to the high number of macro particles this step typically consumes most resources in the PIC cycle. During this step boundary conditions as absorption and particle loading are applied, followed by optional Monte-Carlo interactions, such as collisions or ionisation routines, which concludes the PIC cycle.

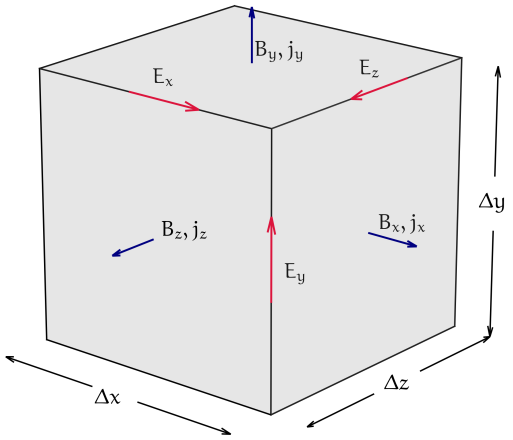

Figure 7.2: Visualisation of one cell of the Yee grid with lengths Δx, Δy and Δz. The electric field values are defined at the cell edges (red arrows), whereas magnetic field values are defined on the cell faces (blue arrows).

7.2 STABILITY AND RESOLUTION OF PIC CODES

The concatenation of numerical tasks makes PIC codes complex programmes. Each step and its specific implementation therefore imposes requirements that need to be fulfilled in order to sufficiently sample the involved physical effects and to provide numerical stability of the code.

One important resolution key figure for the Lagrangian section of the PIC cycle involves the number of PARTICLES PER CELL N_{ppc}, which determines the number of particles that are initialised in a single cell and thus governs the sampling of density distributions at their initialisation. Together with the cell dimensions Δx, Δy and Δz, the number of particles per cell N_{ppc} defines the number of particles per macro particle N_{ppm}, which is typically conserved throughout the simulation. Therefore, it has to be chosen appropriately in order to describe collective effects, such as the formation of plasma waves, or the evolution of particle beams.

Another key figure for resolution concerns the Eulerian section of the PIC cycle, namely the discretisation of physical quantities through the grid parameters Δx, Δy and Δz. The choice of the grid size should be guided by the smallest physical structures of relevance in the simulation. For instance, in PWFAs the minimum of the accelerating field at the vertex of the blowout requires $\Delta x < k_p^{-1}$ in order to sufficiently map the non-linear behaviour of the wakefields. Similar rules apply to the choice of Δy and Δz in order to sufficiently sample the distribution of sheath electrons.

The final key figure regards the stability of PIC cycles. It poses restrictions on the time step Δt as can be found by the Van Neumann stability analysis of Yee grids [178]. The result of this analysis is often termed COURANT CONDITION and reads [178, 193]

$$(c\Delta t)^2 \leqslant \left(\frac{1}{\Delta x^2} + \frac{1}{\Delta y^2} + \frac{1}{\Delta z^2} \right)^{-1} . \tag{7.1}$$

Equation (7.1) ensures the convergence of the Leapfrog algorithm employed for the temporal integration of the PIC cycle. Moreover, it couples the time step Δt to the resolution of the spatial grid. Higher spatial resolution thus demands smaller time steps resulting in increased number of PIC cycles per simulated time.

Related to the previously discussed criteria is another numerical phenomenon termed NUMERICAL CHERENKOV RADIATION [62]. Its origin lies in the unphysical dispersion relation caused by the Yee grid, which only allows for resolving frequencies below the cutoff frequency $\omega_c \propto \pi/\Delta t$ [69, 118]. As a consequence, frequencies close to ω_c propagate slower than the speed of light and can couple to particles of similar phase velocities. This results in artificially distorted phase spaces of these particles and can lead to numerical emittance growth in plasma wakefield simulations [96]. However, high resolution and the implementation of modified field solvers can suppress such effects [39].

Naturally, sufficient sampling of physical phenomena requires high resolution, i.e. small Δx, Δy, Δz, Δt and large N_{ppc}, N_{ppm}. At the same time, an economical choice has to be made to keep computational costs at a minimum. This poses a challenge in plasma wakefield simulations, which feature various scales of relevance [139]. On one hand, small features such as laser oscillations demand spatial resolutions $\ll \lambda_L$. On the other hand, plasma wavelengths $\lambda_p \approx 10\,\mu m$ to $100\,\mu m$. Moreover, particle acceleration typically occurs over mm to metre scales. Sufficiently sampling all three scales in simulations is often unfeasible, such that various strategies have been developed to avoid some of these. For instance, in many cases, laser pulses can be approximated by their envelope [38] and therefore relax the need for ultra-high resolution. This is widely used in LWFA simulations and schemes that rely on the laser-generation of cold plasma, such as the plasma torch injector.

7.3 MODELLING PWFA IN VSIM

All simulations presented in this thesis employ the 3D PIC code VSim based on the Vorpal computational engine [126]. This code is widely established for 3D simulation of various physics problems including PWFAs and offers high-performance computation that is optimised for large numbers of processors.

For efficient parallelisation of the code, the spatial grid is divided into groups of cells, or PIC domains. This decomposition is separately applied to all spatial dimensions

and depends on the total number of processors N_{cores}. Per default, VSim calculates the number of domains per dimension $N_{DC,x}$, $N_{DC,y}$ and $N_{DC,z}$ as factorisation $N_{cores} = N_{DC,x} \times N_{DC,y} \times N_{DC,z}$. Efficient parallelisation of VSim is achieved for approximately 20 to 40 cells per domain [37]. Smaller values do not increase the performance as communication between processors increasingly leads to slowdown.

To reduce the simulation costs, VSim offers to restrict the simulation to the frame co-moving with the PWFA. This avoids the computation of unnecessary regions upstream, or downstream of the drive beam's momentary position. Particle distributions are then loaded into the simulation at the leading edge of the simulation window. For this, VSim provides a modular approach, where various particle species can be incorporated separately. For instance, modelling the plasma torch PWFA as outlined in Chapters 8 and 9 requires a species for wake excitation and a torch species localised in a small region of the simulation. Limiting the torch species to this region avoids its particle push upstream of the injector and therefore saves computational resources.

The modular structure of VSim allows for adding further functionality. For instance, the implemented ADK routine evaluates tunnelling rates during the simulation and generates particles accordingly. Including this effect proved especially valuable for simulating timing-dependent plasma torch injection in Section 8.7. These simulations further profited from the available PARTICLE HISTORIES, which record information of tagged particles and allows for reconstructing the trajectories of involved electrons – a powerful tool for investigating PWFA injectors.

Part II

PLASMA TORCH INJECTION AT SLAC FACET

The findings presented in this chapter relate to the E-210 campaign at the Facility for Advanced Accelerator Experimental Tests (FACET) – a part of the SLAC National Accelerator Laboratory. In the course of this experiment, different milestones were achieved. This includes the development and implementation of a spatio-temporal alignment technique for laser and electron beams that is termed the plasma afterglow technique [152, 153]. Another major achievement was the generation of the plasma channel by selective laser-ionisation, which allowed for pursuing the main goals of this programme, i.e. the realisation of localised injection mechanisms in PWFA. This resulted in the very first successful downramp injection in beam-driven wakefield accelerators enabled by the plasma torch scheme [175] and the first realisation of the plasma photocathode in 90 degree geometry [44]. These results are incorporated in various PhD theses [1, 87, 152], whereas this thesis focuses on the PIC modelling of the plasma torch injector.

Throughout the following sections, essential components and diagnostics of the FACET experiments are introduced. This lays the foundations to study the design and properties of the plasma torch injection process in more detail. The main part of this chapter then investigates the plasma torch injector at SLAC FACET and concludes with strategies for experimental improvement of the stability and performance.

8

PLASMA TORCH INJECTION AT SLAC FACET

The E-210 experimental campaign at SLAC FACET pushed the state-of-the-art with the development on various fields, such as the plasma source, the synchronisation between electron and laser beams, or the plasma wakefield accelerator itself. Before studying the plasma torch injector in this context, the basic building blocks of the experimental setup and the procedures that enabled successful implementation of this experiment have to be introduced. For more details on other experimental results [1, 87, 152] are highly commended.

8.1 EXPERIMENTAL SETUP AT SLAC FACET

Figure 8.1 displays the layout of the experiments at SLAC FACET, where the linac provided electron beams as indicated in green at the top left of the figure. These beams were aligned along the x-direction and typically featured beam charges $Q_D \approx 3.2\,\mathrm{nC}$, r.m.s. length $\sigma_x \approx 25 - 40\,\mu\mathrm{m}$, r.m.s. width $\sigma_y \approx 15 - 30\,\mu\mathrm{m}$, $\sigma_z \approx 20 - 30\,\mu\mathrm{m}$ and energy $W_D \approx 20\,\mathrm{GeV}$. Variation of the beam extent were natural products of drifts in linac components that particularly changed throughout different experimental shifts. The electron beam was focused into the metre-long experimental chamber, which held homogeneously distributed, neutral hydrogen and helium gas. Both gases were pre-mixed to a ratio 1 : 1 at pressures of approximately $5.2\,\mathrm{mbar}$. The choice of these gases allowed for exploiting the ionisation gaps visualised in Fig. 3.3 to selectively ionise hydrogen, while leaving helium in its gaseous state. Other gas mixtures were impractical to use at FACET, or exhibit similar ionisation states. The latter would lead to the undesired coupling of the plasma components, which then results in reduced flexibility and control of the injector. For all injection experiments during the E-210 campaign, hydrogen facilitated the generation of the plasma channel, which was employed for exciting the plasma wake. Helium, in contrast, was the gas reservoir for creating additional localised plasma, e.g. for generating the plasma torch.

The pre-ionisation laser was focused into the experimental chamber by a holographic axilens [41, 68], which was optimised for creating metre-long line foci while omitting field values leading to tunnel ionisation of helium. This selectively ionised hydrogen formed the plasma channel. Ionisation of helium thus set an upper limit for the intensity of the pre-ionisation laser. The axilens-focusing of the pre-ionisation laser produced an intensity profile that strongly varied with the longitudinal position x. Particularly the transverse intensity distribution altered as function of x, such that the generated plasma channel formed the tapering bead chain formation coloured blue in the centre of Fig. 8.1.

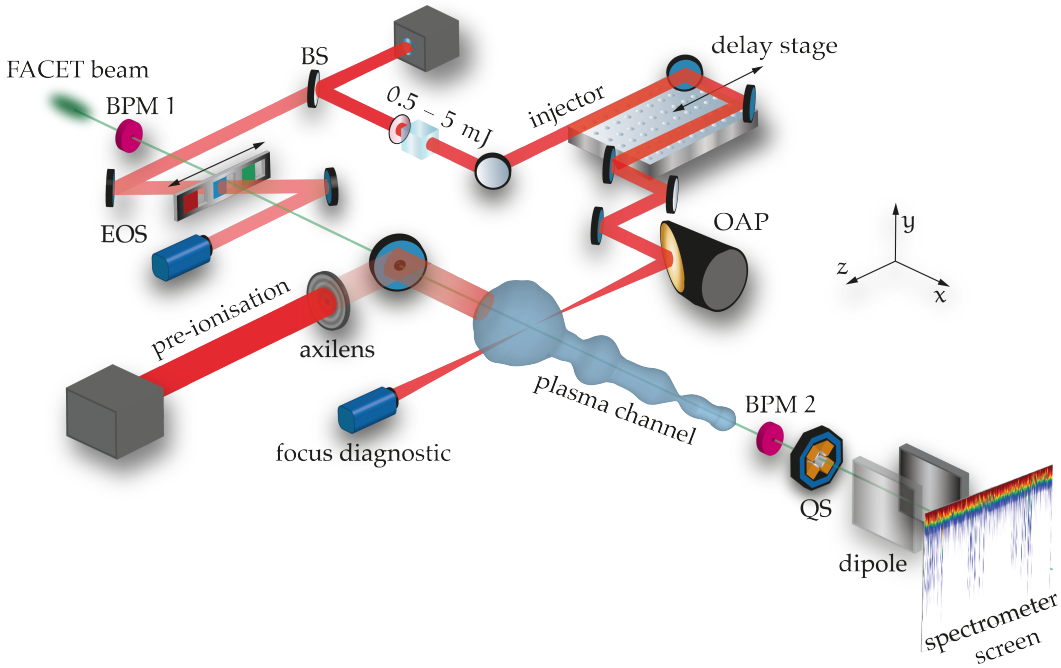

Figure 8.1: Experimental setup for injection studies at SLAC FACET. The electron beam provided by the FACET linac (green, top left) propagates along its orbit marked as green line. The pre-ionisation laser is focused by a holographic axilens setup and generates the plasma channel (blue) from ambient hydrogen. A separate laser chain operates the EOS timing diagnostic. A fraction of this laser is split off serving as injector laser and traverses an energy attenuator, optical delay stage and is focused by an f/22 off-axis parabola (OAP) to the interaction point $x \approx 0$. Here, the injector laser generates plasma from neutral helium that superimposes the plasma channel. This image is a modified version of the illustration in [44].

The finite transverse extent of this distribution consequently defined the lower limit of the hydrogen gas density, as the channel had to fully enclose the excited blowout formation. A hydrogen density $n_H \approx 1.3 \times 10^{23}\ m^{-3}$ met these requirements. However, this choice in addition to the focusing geometry caused numerous experimental challenges as well as opportunities as addressed later in Section 8.9.

A fraction of the pre-ionisation laser arm was split off and separately compressed. The resulting pulse was split once more to serve as probe beam and injector beam, respectively. The latter traversed an energy attenuator that allowed for tuning its energy, followed by an optical delay stage as shown in the top half of Fig. 8.1. This pulse was then focused in z-direction to the interaction point $x \approx 0$ by an f/22 off-axis parabola (OAP). Table 8.1 summarises the properties of the injector laser, which reached vacuum peak intensities ranging from 1.2×10^{15} to $1.2 \times 10^{16}\ W/cm^2$ in its focus position, when assuming ideal Gaussian focusing (see Section 2.1). These intensities ionised the gas mix to varying degrees, as discussed in detail in Section 8.4, thus laying the foundations for studying plasma torch injection at SLAC FACET.

Table 8.1: Properties of the injector laser at SLAC FACET.

wavelength	$\lambda_L = 800\,nm$
pulse energy range	$\varepsilon_L = 0.5 \ldots 5\,mJ$
FWHM pulse duration	$\tau_L = 64\,fs$
spot size ($1/e^2$ of intensity)	$w_0 = 20\,\mu m$

Beam position monitors (BPMs) up- and downstream of the experimental chamber measured the electron beam charges. Both were calibrated to yield 0-difference for the FACET electron driver beam without injection and acceleration of additional charge captured from the plasma. In case of injection and acceleration of charge in the PWFA, however, the excess charge was quantified by the difference of the BPM signals. Spectra of the electron beams were recorded using an imaging spectrometer set to a focusing energy of 1.7 GeV further downstream [1].

The relative timing between the driver beam and injector laser and in particular the time-of-arrival at the interaction point $x \approx 0$ were vital for the injection studies in the experimental campaigns. Therefore, the electro-optic sampling technique [192] was implemented. This method is based on the action of a birefringent crystal on the linearly polarised probe pulse. The polarisation of this pulse rotates as it traverses the EOS crystal. A polariser between the crystal and the EOS camera was crossed to the probe's resulting polarisation. The probe pulse did not reach the EOS camera in this configuration. In the presence of the strong electric fields of the electron drive beam, however, the birefringence of the crystal was modulated. Consequently, a fraction of the probe pulse traversed the polariser and encoded the relative time-of-arrival (TOA) between drive beam and probe pulse, which was then recorded at the probe camera. At FACET, the EOS allowed for assigning TOAs for each measurement with an accuracy of $25.8 \pm 2.5\,fs$ [153] and therefore improved the timestamping of $109 \pm 12\,fs$ usually available at FACET. Since the probe pulse and the injector laser originated from the same laser chain, both were inherently synchronised, which allowed for inferring the TOA between the injector laser and the electron beam at the position of the EOS, when taking into account the optical delay stage.

8.2 THE ENHANCED PLASMA AFTERGLOW

As an important stepping stone for the injection experiments at SLAC FACET, a novel technique for spatio-temporal alignment between electron beams and laser pulses directly at their interaction point was developed and tested. This was crucial for both, plasma torch injection and the plasma photocathode injector, which required spatio-temporal coordination of the injector laser and the driver beam. The underlying concept

of this technique is outlined in the following section. For more details [152, 153] are recommended.

The enhanced plasma afterglow utilises the setup as shown in Fig. 8.1 with the pre-ionisation laser switched off. It relies on the generation of plasma filaments with the injector laser and the associated radiation from the plasma recombination – the plasma afterglow. The experiments concluded that heating the plasma filament with the intense electron beams available at SLAC FACET in the overdense regime enhances the intensity of the afterglow. Following PIC studies revealed that minuscule fractions of the electron beam energy, i.e. $\approx 0.001\,\%$, is transferred via its unipolar electric fields to the plasma electrons [153]. This interaction leads to separation of plasma electrons and ions, which causes electron oscillations outside the plasma filament with energies ranging from eV to keV [152]. Such energies coincide with cross sections for impact ionisation of hydrogen and helium [116], i.e. electron energies exceed the ionisation potential of ambient gas. This triggers the production of secondary electrons, which can gain energy in the present fields and lead to further plasma production via impact ionisation. These secondary effects increase the number of plasma electrons and enhance the plasma afterglow. Resulting radiation can be imaged by a camera integrating over tens of ms and thus converts fs interactions to observables of less demanding time scales.

Interestingly for diagnostics purposes, the generation of plasma afterglow is sensitive to the spatio-temporal distribution of the plasma filament. For example, if the injector laser generates the plasma filament after the electron beam passed the interaction point, the afterglow is the sole result of the laser-produced glow. For TOAs where the injector laser and electron beam coincide at the interaction point, the plasma filament is halfway formed. The afterglow signal increases compared to the previous timing case. However, the maximum afterglow signal is expected for the fully formed plasma filament, i.e. the injector laser passed the interaction point before the arrival of the electron beam. Similar considerations apply to the case of an injector laser that is transversely misaligned with respect to the orbit of the FACET beam. Here, optimum alignment coincides with the most intense afterglow signal [153]. The enhanced plasma afterglow can therefore be harnessed for diagnosing spatio-temporal alignment of laser and intense electron beams directly at their interaction point. Further, it only consumes a minute fraction of the electron beams energy and is therefore minimally intrusive. The synergy of the enhanced plasma afterglow and the plasma torch injector together with their experimental feasibility render both schemes ideal for investigations in other laboratories.

8.3 APPLICABILITY OF THE ADK MODEL

Before modelling the optical generation of plasma filaments via the tunnelling rates in Eq. (3.5), it has to be validated that the ADK formalism applies to the parameter range of the injector laser shown in Table 8.1. Corresponding peak electric fields range from

$E_{L,0} \approx 95\,\mathrm{GV/m}$ to $301\,\mathrm{GV/m}$. Therefore, $U_p \approx 72$ to $720\,eV$ and $\hbar\omega_L \approx 1.5\,eV$. For typical gases employed in PWFA (cf. Table 3.2), the tunnelling conditions $U_p > \varepsilon_{ion} > \hbar\omega_L$ and $\gamma_K < 1$ are met and thus guarantee the validity of the ADK model. Yet, recalling the upper limit through E_{BSI} as visualised in Fig. 3.3, it becomes apparent that $E_{L,0} > E_{BSI}$ for the gas mixture used at SLAC FACET. This would be problematic for temporal flat-top profiles of the laser pulse together with the energy range in Table 8.1. However, full tunnelling ionisation can be achieved for laser envelopes with slowly increasing field slopes $E_L(t)$ before $E_L(t) = E_{BSI}$, such that the ADK model remains valid. This is studied in further detail by considering the local ionisation probability for varying electric fields $E_L(\vec{r}, t)$

$$P_{ADK,av} = 1 - \exp\left(-\int W_{ADK,av}(E_L)\,dt\right). \tag{8.1}$$

Similar to [91], the integration can be performed at a constant position when assuming a laser with linear envelope $E_L = E_0(1 - t/\tau)$, $t \in [0, \tau]$ and $E_0 > E_{BSI}$ as illustrated in Fig. 8.2 a). The time t_{BSI} is then defined as $E_L(t_{BSI}) = E_{BSI}$, which allows for studying the integrated ionisation rate in the field interval $[0,\ E_{BSI}]$

$$\begin{aligned}\int_{t_{BSI}}^{\tau} W_{ADK,av}\,dt &= \int_{E_{BSI}}^{0} \frac{W_{ADK,av}}{\dot{E}_L}\,dE_L \\ &= 38.07\,\frac{E_h}{E_0}\,\frac{\tau Z^5}{n_{eff}^{2n_{eff}+6}}\,\exp\left[2.79(2n_{eff} - 1.5)\right]\,\Gamma(2n_{eff} - 2.5,\ 4.55),\end{aligned} \tag{8.2}$$

where Γ denotes the upper incomplete gamma function and τ enters the equation in units of fs. Equation (8.1) implies that the ADK model remains valid if full ionisation $P_{ADK,av} \approx 1$ is reached on the pulse slope as indicated by grey shades in Fig. 8.2 a). This is achieved for large values of Eq. (8.2), i.e. for long pulse durations τ and low peak fields E_0. As an example, evaluating Eq. (8.2) for hydrogen yields approximately $0.1 \times \tau\, E_h/E_0$, such that the available field strength of the injector laser $E_0 \approx 300\,\mathrm{GV/m}$ requires $\tau \gg 10\,fs$. The second ionisation level of helium, in contrast, yields $4 \times \tau\, E_h/E_0$ and allows for tunnelling ionisation by shorter laser pulses. Figure 8.2 b) displays the numerical evaluation of Eqs. (8.1) and (8.2) for hydrogen and both states of helium as function of the peak field strength E_0 and the corresponding laser energy $\varepsilon_L(E_0)$ for the laser parameters shown in Table 8.1. In the linear approximation of the laser envelope and with the laser properties as shown in Table 8.1, one finds that the ADK formalism is violated for $E_0 > 500\,\mathrm{GV/m}$, or $\varepsilon_L > 15\,mJ$ in case of single ionisation of hydrogen and helium. Here, the pulse front leaves neutral gas behind, which is then subject to other ionisation processes such as BSI (cf. Section 3.2). The second helium level, however, supports tunnelling ionisation at much higher intensities. This analysis shows that tunnelling ionisation may be applicable for long laser pulses, despite exceeding the threshold E_{BSI}. For the injector laser parameters available at SLAC FACET, it is found that

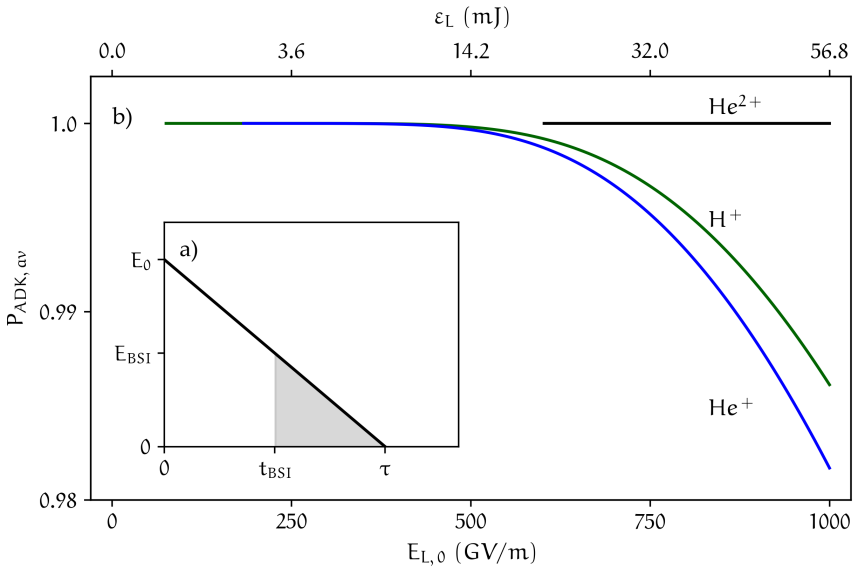

Figure 8.2: Applicability of the ADK model at SLAC FACET. a), modelling of a linear laser envelope with peak electric field $E_0 > E_{BSI} = E_L(t_{BSI})$. Grey shades indicate the time interval where $E_L < E_{BSI}$. b), ionisation probability $P_{ADK,av}$ on the slope of a laser pulse in linear approximation with peak electric field $E_{L,0} > E_{BSI}$ (lower axis) and respective laser pulse energy $\varepsilon_L(E_{L,0})$ (upper axis, other laser parameters according to Table 8.1).

the gas mix is ionised on the rising edge of the laser pulse justifying the use of the ADK model. In fact, Eq. (8.2) indicates a large safety margin that in principle allows for even doubling the injector laser energy.

8.4 OPTICAL GENERATION OF COLD PLASMA FILAMENTS AT SLAC FACET

After introducing the experimental setup on the previous pages and assuring the validity of our theoretical approach, the optical generation of plasma spikes is addressed in the following. In principle, the plasma torch injector allows for generation and application of arbitrary plasma torch density distributions. It benefits from the flexibility and the opportunities arising from the use of lasers, e.g. Gaussian laser pulses produce localised plasma spikes and elaborate focusing allows for shaping of 3D density distributions.

At SLAC FACET, the injector laser was dedicated to creating the plasma torch from neutral helium to superimpose the plasma channel that was pre-formed from hydrogen gas. Nevertheless, the injector laser additionally ionised neutral hydrogen outside and at the boundaries of the plasma channel, which affects the injection process in some cases (see Section 8.9). The plasma torch generation from all gas components is therefore considered, whereas atomic hydrogen with an ionisation energy of 13.6 eV was assumed.

The injector laser was linearly polarised in x-direction with the propagation direction parallel to z and modelled as Gaussian pulse in the envelope approximation according to Eq. (2.8). Despite the fact that the laser fields exceed the critical value for tunnelling

ionisation, the formalism still holds for these long pulses as discussed in Section 8.3. As further shown in Fig. 8.2 b), the assumptions of the ADK model are only violated for laser energies in excess of approximately 15 mJ. These considerations give us the confidence to model the generation of the plasma torch utilising the ADK formalism.

The ionisation probability $P_{ADK,av}(r,z)$ is obtained by integrating the rates in Eq. (8.1), which depend on the spatio-temporally varying injector laser. Multiplying $P_{ADK,av}$ with the maximum available plasma density $n_{T,0}$ from this ionisation state gives the spatial plasma electron distribution. The total distribution of the plasma torch then results from adding the density components of hydrogen and both helium states. This approach has been verified against ionisation routines in VSim with excellent agreement.

As a result of the Gaussian laser focusing, the resulting density distributions adopt the laser's radial symmetry. This radial symmetry is one unique feature of the plasma torch injector and therefore contrasts to hydrodynamic approaches of generating density spikes as discussed in Section 6.4.

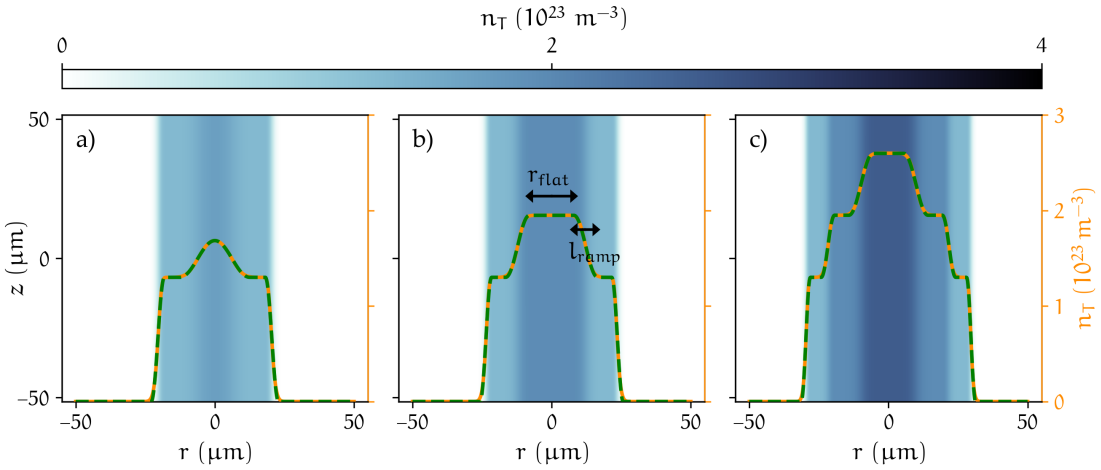

Figure 8.3: Optically generated plasma spikes at SLAC FACET. Shown are density distributions generated from hydrogen and helium that are calculated from ADK rates of the injector laser at FACET. a), b) and c) correspond to pulse energies $\varepsilon_L = 0.5$, 1.0 and 5.0 mJ resulting in varying degrees of ionisation (blue shades encoding H^+, He^+ and He^{2+} plasma). Dashed orange and dashed green lines correspond to density profiles through $z = 0$ (right axis) and its approximation through Eq. (8.3) (right axis).

Figure 8.3 a), b) and c) illustrate plasma density distributions computed from the parameters in Table 8.1 with the laser energies $\varepsilon_L \approx 0.5$ mJ, 1.0 mJ and 5.0 mJ, respectively. Profiles through $z = 0$ are shown in orange and have density values according to the right y-axis. For all shown cases, the fields required to free electrons from hydrogen gas are exceeded by far. This results in radial plateaus as illustrated by density lines approaching the full hydrogen density $n_T = 1.3 \times 10^{23}$ m^{-3}. However, the contributions to the plasma spikes generated from helium ionisation differ substantially in all cases. The injector energy $\varepsilon_L \approx 0.5$ mJ achieves ionisation of only 60% from helium and forms a single peak with gradients of $l_{ramp} \approx 12.5$ µm length. Doubling the energy of the

torch laser results in full depletion of He and now involves another plateau region of full ionisation with radius $r_{flat} \approx 16.1\,\mu m$. The laser focusing and the exponential behaviour of tunnelling ionisation both lead to shorter density gradients $l_{ramp} \approx 8.5\,\mu m$ compared to the previous case. The highest pulse energy available at SLAC FACET $\varepsilon_L \approx 5\,mJ$ further liberates electrons from ionisation of He^+ ions. The total peak density of hydrogen and helium hence amounts to $2.6 \times 10^{23}\,m^{-3}$ and causes further steepened density gradients.

To implement these results in PIC simulations and introduce a terminology describing these shapes, the parameters r_{flat} and l_{ramp} are introduced to describe radial torch distributions resulting from ADK calculations:

$$\frac{n_T(r)}{n_{T,0}} = \begin{cases} 1 & : r < r_{flat} \\ \cos^2\left(\frac{\pi}{2}\frac{r-r_{flat}}{l_{ramp}}\right) & : r_{flat} \leqslant r < r_{flat} + l_{ramp} \\ 0 & : r_{flat} + l_{ramp} < r, \end{cases} \tag{8.3}$$

where $r = \sqrt{x^2 + y^2}$. Equation (8.3) describes the profile resulting from ionisation of one gas component and $n_{T,0}$ denotes its peak density including the degree of ionisation. Choosing cosine shaped ramps has numerical advantage over, e.g. Gaussian shaped ramps, that $n_T(r = r_{flat} + l_{ramp}) = 0$ and hence requires no artificial cuts at the interface of the ramp and background plasma. The parametric approximation of the radial profile is visualised in Fig. 8.3 as green lines and agrees well with the ADK calculations.

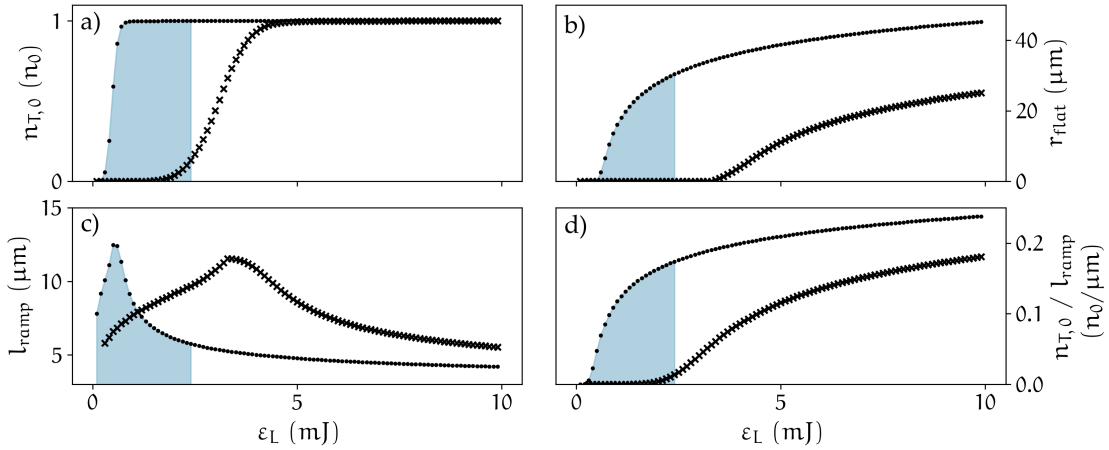

Figure 8.4: Parametric dependency of the plasma torch profile on the injector energy ranging up to $\varepsilon_L = 10\,mJ$. Shown are the first (black dots) and second state of helium (black crosses). Shaded areas mark regions without significant ionisation of the second helium level, i.e. $n_{T,0} < 0.2$. a), degree of ionisation, b), flat top length, c), ramp length and d), torch gradient as function of ε_L.

The parametrisation through Eq. (8.3) allows for investigating the scaling of the plasma torch profile as function of the laser and gas properties. For instance, Fig. 8.4 shows the torch parameters as function of the laser energy ranging from $\varepsilon_L = 0.1\,mJ$ to $\varepsilon_L = 10\,mJ$ for the first (black dots) and the second (black crosses) ionisation level of helium. Panel a)

quantifies the resulting degree of ionisation and repeats an observation already made in Fig. 8.3. For these laser parameters, helium is fully ionised for low laser energies already, whereas He^+ ions are fully freed from their electrons for $\varepsilon_L > 4\,mJ$. In principle, this defines an energetic range where only He can be ionised without significant He^+ contributions to the density as indicated by the shaded regions. After the onset of full ionisation the radius of the plateau region r_{flat} grows with the laser energy as depicted in b). This increases the cross section of the density spike and defines different injector regimes as discussed in Chapter 9. Resulting ramp lengths l_{ramp} are shown in c). This plot highlights that gradients of few μm length can be generated. This is vital for successful implementation of density spikes as injectors. A related quantity is the ratio $n_{T,0}/l_{ramp}$, which is proportional to the gradient of the density distribution. While the laser properties determine the ramp length, $n_{T,0}$ can be varied by adapting the gas mixture. This allows for tuning the density gradient of the plasma spike and gives additional control over the gradient $n_{T,0}/l_{ramp}$.

8.5 PHENOMENOLOGICAL TRAPPING MODEL

The plasma torch is capable of producing steep and short density gradients of the order of μm, which is shorter than typical plasma wavelengths $\lambda_p \approx 10$ to $100\,\mu m$ in PWFAs. As discussed in Section 6.3, this enables the rapid regime of density downramp injection, where electron populations break from the wake sheath and experience the fields inside the blowout before reaching the wake vertex. Given that electrons experience the accelerating fields E_ξ sufficiently long, they gain enough forward momentum to remain inside the plasma wave. Here, E_ξ is the accelerating wakefield component in the quasi-static approximation [162], i.e. the unperturbed, static field. Although evolving wakefields violate the quasi-static approximation in principle, it is commonly used to approximate wakefield accelerators and the dynamics during downramp injection [114]. The accelerating field E_ξ relates to the 3D wake potential Ψ as $cE_\xi = -\frac{\partial \Psi}{\partial \xi}$ [112] and can be rewritten to

$$\Psi(\xi', y, z) = \frac{1}{\lambda_p}\Big[\Psi(\xi, y, z) * \delta(\xi, y, z)\Big](\xi'). \tag{8.4}$$

Here, δ denotes the Dirac delta function and $*$ is the convolution operator with respect to the propagation direction ξ defined as [77]

$$\Psi * \delta = \int \Psi(\xi, y, z)\delta(\xi - \xi', y, z)\,d\xi, \tag{8.5}$$

where ξ' is the convolution variable and $\lambda_p^{-1} = \lambda_p^{-1}(n_{ch})$ accounts for the periodicity of the plasma wake that is sustained by the plasma channel density n_{ch}. Treating the highly localised plasma torch as perturbation allows for making the transition from

a single test particle to a function of the plasma torch density distribution $\eta(n_T)$ via $\delta(\xi, y, z) \rightarrow \eta(n_T(\xi, y, z))$. Then, the torch potential reads

$$\Psi_T(\xi' y, z) = \frac{1}{\lambda_p}\Psi(\xi, y, z) * \eta(n_T). \tag{8.6}$$

The corresponding accelerating field $E_{\xi,T} = \lambda_p^{-1} E_\xi * \eta$ is used in Gauss's law and one obtains

$$Q_M(\xi') = -\frac{\varepsilon_0}{\lambda_p}\iint E_\xi * \eta(n_T)\,dy\,dz, \tag{8.7}$$

which yields the unit of charge. The convolution variable ξ' accounts for the motion of the wakefield through the density distribution and can further parametrise $\eta(n_T)$, e.g. in the case of a timing-dependent generation of the torch distribution from a propagating injector laser. Notably, Eq. (8.7) depends on the transverse extent of the torch distribution through integration over y and z. This reflects the control over injected charge via the transverse extent of n_T and is studied in Chapter 9. The minimum $Q_M(\xi')|_{min}$ characterises the strongest overlap of the torch distribution and the accelerating field and is found to scale with the trapped charge in plasma torch injectors.

The core process in density downramp injection is the expansion of the plasma wave, which is characterised by the relative change of the plasma period

$$\frac{\Delta\lambda_p}{\lambda_p} = \frac{\lambda_p(n_{ch}) - \lambda_p(n_{ch} + n_T)}{\lambda_p(n_{ch})} = 1 - \frac{1}{\sqrt{1 + n_T/n_{ch}}}. \tag{8.8}$$

The distribution function $n_T(\xi, y, z)$ determines this quantity, i.e. regions beyond the plasma torch yield $\Delta\lambda_p/\lambda_p = 0$, whereas in the vicinity of the density spike $\Delta\lambda_p/\lambda_p > 0$. In first order approximation, the wake volume scales as $\propto (\Delta\lambda_p/\lambda_p)^3$. To account for the expanding wake volume, $\eta = \mathcal{C}(\Delta\lambda_p/\lambda_p)^3$ is incorporated into the model function, where $\mathcal{C}$ is a constant. Then, the resulting model equation reads

$$Q_M = -\frac{\varepsilon_0 \mathcal{C}}{\lambda_p}\left[\iint E_\xi * \left(\frac{\Delta\lambda_p}{\lambda_p}\right)^3 dy\,dz\right]_{\min\xi'}. \tag{8.9}$$

The convolution term can be understood as moving the effect of the plasma torch through the accelerating field distribution, whereas $\Delta\lambda_p/\lambda_p$ filters out field values that are outside the plasma torch volume. The best agreement between simulations and experiments is found for $\mathcal{C} = 565$, which is used throughout this thesis.

In principle, E_ξ can be obtained from models such as [63, 102], or those outlined in Eq. (6.3), which allows for efficient computation of Eq. (8.9) in combination with the torch parametrisation in Eq. (8.3). However, to consistently include effects of the wake evolution and other subtleties prior to injection, Eq. (8.9) is evaluated using one snapshot of the field distribution from PIC simulations before the plasma torch.

8.6 FULLY FORMED PLASMA TORCH INJECTORS

The experimentally realised plasma torch distributions for $\varepsilon_L = 0.5$, 1 and 5 mJ laser energy (see Fig. 8.3) are now employed as plasma torch injector located at the interaction point $x \approx 0$. First, the case is considered where the plasma torch is already fully produced by the torch laser at the arrival of the driver beam. For this, the experimental conditions at SLAC FACET are recaptured in 3D PIC simulations using VSim [126]. Cubic cells of 2 µm length are used and the distribution of the plasma channel, as visualised in Fig. 8.5, is loaded into the simulation and sampled by 8 PPC. The FACET electron beam is initialised with 16 PPC and the parameters shown in Table 8.2.

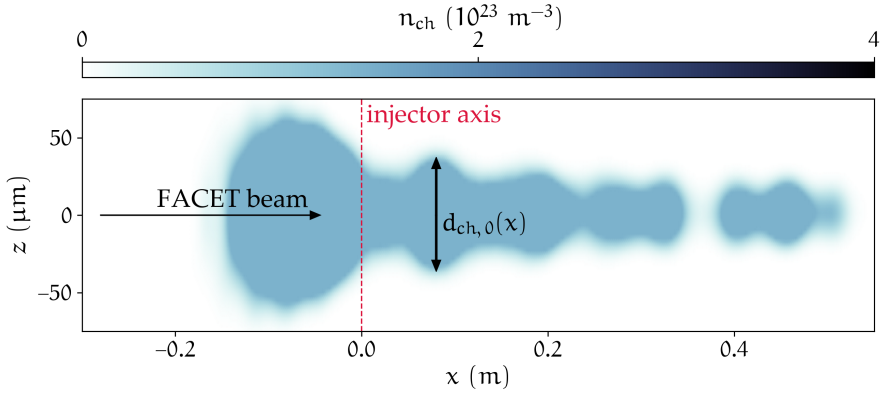

Figure 8.5: Plasma channel at SLAC FACET. Density distribution of the plasma channel of varying width $d_{ch,0}(x)$ facilitating wake excitation at the experiment. The injector laser propagates along the dashed line and intersects the path of the driver beam at $x \approx z \approx 0$. The density distribution is adapted from [44].

After initialisation, the electron driver beam propagates through the pre-ionised plasma profile until the interaction point $x \approx 0$. In this section, the beam is substantially shaped by the interplay with the plasma channel. For instance, after the upramp of the plasma density at $x \approx -0.12$ m (cf. Fig. 8.5), the blowout fully forms behind the drive beam. At this position, however, the drive beam length exceeds the length of the first plasma period leading to the separation of ≈ 5 pC driver particles within the second wake period, where it potentially remains throughout the PWFA due to their high energy. The drive beam subsequently undergoes envelope oscillations due to its transverse mismatching with respect to the plasma density $\sigma_m \approx 0.5\,\mu m \ll \sigma_y, \sigma_z$ (see Eq. (4.6)), such that it develops a scalloping pattern [14, 99]. Additionally, the varying transverse channel extent influences the wake excitation and the driver therefore experiences changing forces dependent on its position x. All these effects cause a substantially re-arranged density profile of the driver beam at the interaction point $x \approx 0$. Here, it is described by $\sigma_x \approx 39.0\,\mu m$, $\sigma_y \approx 8.5\,\mu m$, $\sigma_z \approx 12.5\,\mu m$, $\varepsilon_{n,y} \approx 524$ mm mrad and $\varepsilon_{n,z} \approx 781$ mm mrad (cf. Fig. 8.6). Further simulation of the drive beam through the plasma channel without injector indicate that only the first period of the wakefield supports acceleration throughout the

narrowing plasma channel. Injection into subsequent wake buckets may therefore occur, but acceleration of these beams is unlikely due to the evolution of the wakefields in the narrowing plasma channel (cf. [44] suppl. Fig. 2 b)). The following investigations thus focus on beams injected into the first wake period. The pre-lensing simulation outlined

Table 8.2: Driver beam properties at SLAC FACET.

Beam charge	$Q_D = 3.0\,nC$
r.m.s. length	$\sigma_x = 40.0\,\mu m$
r.m.s. width	$\sigma_y = 15.0\,\mu m$
	$\sigma_z = 25.0\,\mu m$
Beam energy	$W_D = 23.0\,GeV$
Energy spread	$\Delta W/W_D = 0.02$
Normalised emittance	$\varepsilon_{n,y} = \varepsilon_{n,z} = 2.25\,mm\,mrad$

above serve as starting point for different injection studies, such as these displayed in Fig. 8.6. Here, the plasma torch is formed ahead of the driver beam arrival, which allows for avoiding the implementation of computationally demanding laser pulses by loading the torch density distribution through Eq. (8.3) into the simulation. Figure 8.6 a), b) and c) correspond to simulations with torch laser energies $\varepsilon_L = 0.5, 1.0$ and $5.0\,mJ$, i.e. the plasma distributions shown in Fig. 8.3. The left, centre and right column panels illustrate the trapping process at simulation times $0.0\,ps$ (before injection), $0.5\,ps$ (during injection) and $12.5\,ps$ (after injection). A selection of electron trajectories in the frame of reference moving with the drive beam is shown as black lines in all cases.

For $\varepsilon_L = 0.5\,mJ$, the plasma torch represents only a small density elevation and gentle gradients, such that its interaction with the wake is weak. This causes a small modulation of the blowout as shown in Fig. 8.6 a2). In this case, electrons forming the plasma wake at the downramp cross the wake sheath approximately at the centre of the blowout. The plasma electron population on wave breaking trajectories therefore experience the fields within the ion cavity only for a short time, cannot gain relativistic energies and leaves the blowout at the wake vertex – no trapping occurs. Doubling the torch laser energy as visualised in Fig. 8.6 b) increases the density gradient by means of a shorter ramp and higher peak density compared to the previous case. This leads to trajectory crossing at phases closer to the blowout centre and electrons gain sufficient forward momentum to remain inside the first wake period. The charge of the witness beam amounts to $Q \approx 94\,pC$, which accelerates to kinetic energies $\overline{W} \approx 105\,MeV$ over the first $3.7\,mm$ of the subsequent acceleration process. Further increasing the torch laser energy to $\varepsilon_L \approx 5\,mJ$ additionally unlocks the second ionisation level of helium and the peak plasma density amounts to $2.6 \times 10^{23}\,m^{-3}$, which further steepens the density gradient. This promotes the deformation of the wake as shown in Fig. 8.6 c) leading to trajectory crossing of a larger number of electrons, closer to the driver beam compared

to the previous case. Consequently, a high charge $Q \approx 498\,\mathrm{pC}$ is injected. In fact, this charge significantly loads the wakefield and hence lengthens the blowout structure (cf. Section 5.3). The witness beam's space charge furthermore diminishes the accelerating wakefields and the beam accelerates to $\overline{W} \approx 75\,\mathrm{MeV}$ corresponding to 71 % of the energy reached by the 1 mJ plasma torch case shown in Fig. 8.6 b).

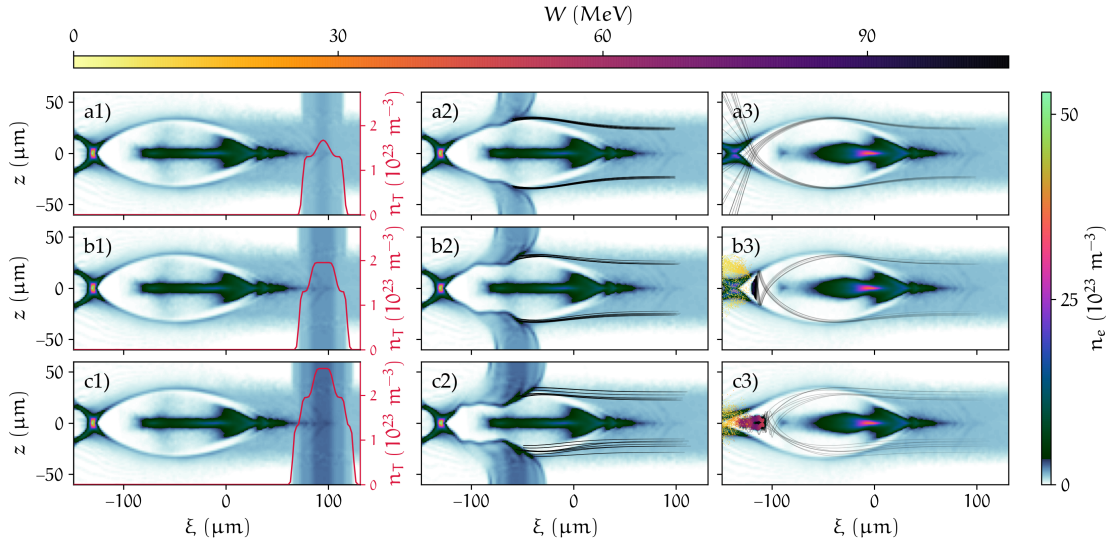

Figure 8.6: PIC study of plasma torch injection at SLAC FACET. The driver beam (green-black) has been significantly shaped due to its interaction with the plasma (pre-lensing) and propagates to the right. It excites a plasma wave in the blowout regime (colour coded white-blue-green). Shown is the trapping process for injector laser energies $\varepsilon_L = 0.5$, 1.0 and 5.0 mJ in a), b) and c) corresponding to the plasma torch distributions displayed in Fig. 8.3. The first, second and third column correspond to snapshots at simulation times $t_{sim} \approx 0.0\,\mathrm{ps}$ (before injection), 0.5 ps (during injection) and 12.5 ps (after injection). Black lines visualise a selection of electron trajectories in the co-moving frame at respective t_{sim}.

The fully formed torch injector is additionally studied via the phenomenological model derived in Section 8.5. For this, the accelerating wakefield component is extracted from PIC simulations shown in Fig. 8.6 and the distribution of the plasma torch is obtained from ADK calculations and the torch parametrisation in Eq. (8.3). The model charge Q_M for injector energies $\varepsilon_L = 1.0$ and 5 mJ amounts to 105 pC and 493 pC and is in good agreement with simulation results (94 pC and 498 pC, respectively). The low energy case $\varepsilon_L = 0.5\,\mathrm{mJ}$ yields $Q_M \approx 6\,\mathrm{pC}$ and thus contrasts with simulation results, which show no trapping. This difference may originate from the fact that the 0.5 mJ case is borderline for injection and requires further investigation.

These simulations indicate the large tunability that is offered by the plasma torch injector. It not only provides density gradients sufficient for trapping in PWFA, but allows for controllable generation of witness beam charges ranging over hundreds of pC by changing the energy of the injector laser.

A modified version of the simulation shown in Fig. 8.6 c) has been provided in [44] to explain experimental observations at SLAC FACET and the role of the plasma torch as

entry point for the Trojan Horse plasma photocathode injector [74]. It accounted for an astigmatic injector laser during these particular experimental shifts, which was incapable of ionising He^+. The second ionisation level of helium was therefore disregarded in these simulations, effectively reducing the density gradient. Compared to the case presented in this section in Fig. 8.6 c), the injected witness charge reduced by approximately 16 % in good agreement with the experimental data set in [44] and hence confirmed the validity of the numerical approach.

8.7 TIMING-DEPENDENT PLASMA TORCH INJECTORS

After establishing the injection dynamics of the plasma torch generated by varying laser energies in the last section, this section describes the impact of the relative time of arrival (TOA) for constant $\varepsilon_L = 5\,\mathrm{mJ}$. At SLAC FACET, the TOA controlled the arrival of the injector laser with respect to the electron drive beam at the interaction point $x \approx 0$ and was varied within a 5 ps timing window by an optical delay stage. Throughout this thesis, $\mathrm{TOA} \ll 0$ is defined as the timings where the injector laser arrives earlier than the driver. In contrast, $\mathrm{TOA} \gg 0$ denotes scenarios where the injector arrives after the driver passed. The timing $\mathrm{TOA} \approx 0$ corresponds to coinciding drive beam and injector pulse. Accordingly, these timings describe plasma torches, which are generated before driver beam arrival (similar to Section 8.6), after driver beam arrival, and during the driver beam arrival. Timings $\mathrm{TOA} \approx 0$ thus imply a density spike which only partially formed when the drive beam approaches $x \approx 0$ and hence differs substantially from the scenarios examined in Section 8.6. The partial formation is particularly pronounced due to the exponentially increasing tunnelling ionisation rates in combination with the long pulse duration τ_L, such that the injector laser's ionisation front is much smaller than τ_L . This is confirmed by ADK calculations for both helium ionisation levels yielding ionisation fronts of approximately 2 µm and 4 µm FWHM length, in contrast to the pulse length of $c\tau_L \approx 19\,\mu\mathrm{m}$, such that the TOA-dependent plasma torch approximately describes a longitudinal step function.

To investigate the time-dependent plasma torch injector for $\varepsilon_L = 5\,\mathrm{mJ}$, the experimental simulations shown in Fig. 8.6 c) have been expanded to include the torch laser in the envelope approximation. This is illustrated in Fig. 8.7 a) for $\mathrm{TOA} \approx -0.2\,\mathrm{ps}$, where the ionisation front of the torch laser coincides with the front of the driver beam. Consequently, the plasma spike is only partially formed such that the torch laser continues to ionise as the PWFA passes. At such timings, witness charge contributions from the plasma photocathode mechanism are expected in addition to injection from wave breaking. For $\mathrm{TOA} \approx 0$, the laser coincides with the driver beam centre (orange cross in Fig. 8.7 a)). Therefore, electrons are released inside the blowout and the plasma photocathode is the dominating effect [44]. Further increasing the timing to $\mathrm{TOA} \approx 0.35\,\mathrm{ps}$ as indicated in Fig. 8.7 a) leads to coincidence of the torch laser and the wake vertex. Positions behind

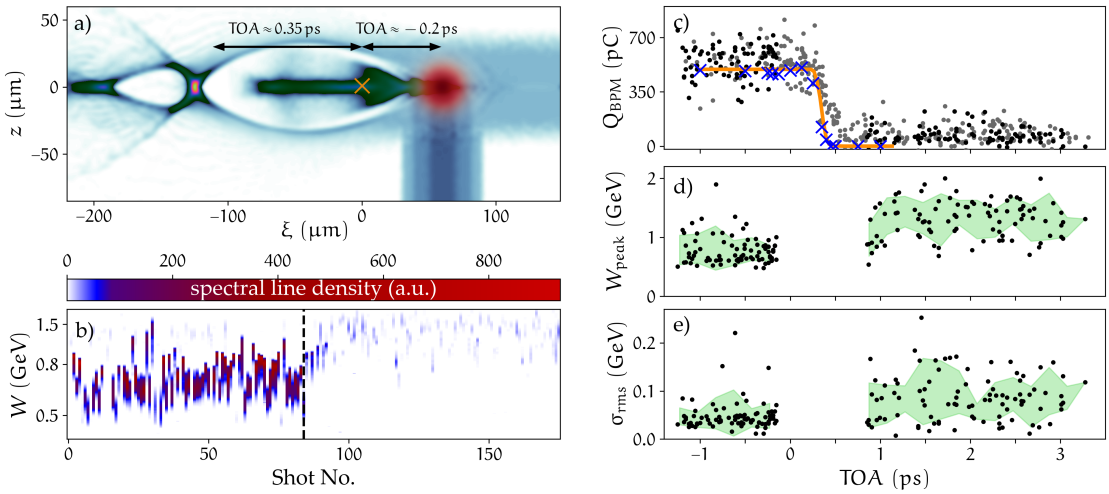

Figure 8.7: Injection from timing-dependent plasma torches at SLAC FACET. a), PIC snapshot illustrating the spatio-temporally dependent torch generation by the injector laser (red) with TOA ≈ -0.2 ps. b), experimentally measured spectral line densities of electron beams injected in torch mode (left of dashed line) and dark current mode (right of dashed line). c), trapped witness beam charge from PIC simulations (blue crosses), the phenomenological model Eq. (8.9) and measured on BPMs at FACET (dots) as function of the TOA. Black dots correspond to the selection in b). d), e), peak energies and r.m.s. spectral width dependent on the TOA for measurements in b). Green regions mark standard deviations around the average values in bins of 0.2 ps.

the vertex do not allow for trapping and hence only 124 pC of charge is trapped, which originates from ionisation at the rear of the wake. For TOA $\gg 0.35$ ps the injector laser does not generate plasma electrons within the first wake period. As discussed above and elaborated in [44], electrons potentially produced in subsequent wake periods are lost throughout acceleration due to the evolution of the wakefields in the narrowing plasma channel. A detailed analysis of the electron beams from the first wake period in the context of the timing transition can be found in Section 8.8.

Injection from timing-dependent plasma torches has been investigated in experiments at SLAC FACET for $\varepsilon_L \approx 5$ mJ and is presented in Fig. 8.7. Figure 8.7 c) shows the injected witness charge as function of the TOA from PIC simulations (blue crosses) and BPM measurements (dots). Since the EOS time stamping yields relative timing values, the simulation results have been used to find the constant timing offset and align simulations and experimental results. Both yield two charge plateaus connected by an approximately linear transition. For the laser-late mode TOA $\geqslant 0.9$ ps, simulations predict no charge, whereas the experimental data exhibits significant charges. This charge shows no correlation with the TOA such that it is not triggered by the torch laser, i.e. it is dark current. In principle, the plasma torch mechanism can be operated dark current free [106]. However, experimental boundary conditions at SLAC FACET caused the production of dark current (see Section 8.9), which represents an unreliable means of witness beam generation. This is further reflected by the measured average charge and

respective standard deviation of $52 \pm 73\,\mathrm{pC}$ and the corresponding relative charge jitter of $73\,\mathrm{pC}/52\,\mathrm{pC} \approx 140\,\%$.

The other plateau region $\mathrm{TOA} \leqslant -0.2\,\mathrm{ps}$ in Fig. 8.7 c) represents the plasma torch mode. Here, injected charges amount to $543 \pm 97\,\mathrm{pC}$ in the experiment and $490\,\mathrm{pC}$ in simulations. The difference of both values suggests that dark current is present in torch shots as well, which is confirmed by the low-charge and high-energy populations in the integrated line spectra in Fig. 8.7 b). This implies that charge fluctuations in this mode of operation partially originate from varying dark current contributions. Despite these adverse influences, the ratio of the standard deviation and the average charge amounts to $97\,\mathrm{pC}/543\,\mathrm{pC} \approx 18\%$, which highlights its reproducibility compared to the former mode of injection and exceeds the charge stability of $33\,\%$ from state-of-the-art downramp injection in LWFA [182]. Further improved charge stability is expected for mitigated dark current injection.

The timing-dependent torch injector is additionally studied via the phenomenological model derived in Section 8.5. For this, the accelerating wakefield component is extracted from PIC simulations shown in Fig. 8.7 and the distribution of the plasma torch is modelled as $n_T(\xi, y, z)\,\Theta[z - c(t - \mathrm{TOA})]$. Here, n_T is computed based on the ADK model and the torch parametrisation in Eq. (8.3) and Θ denotes the Heaviside step function, which approximates the TOA-dependent generation by the injector laser with negligible ionisation front. The model function Q_M is evaluated for the experimental timing range and Fig. 8.7 c) displays the results as orange line alongside the experimental values. It reproduces both plateau regions, the transition and agrees well with the observed charge levels.

Both modes of injection in Fig. 8.7 are further analysed at the electron spectrometer. Fully imaged witness beams are marked black in Fig. 8.7 c) and corresponding integrated line spectra are shown in Fig. 8.7 b) for injection in torch mode (left of dashed line) and dark current mode (right of dashed line). The spectral line densities reflect observations from Fig. 8.7 c) and display spectral peak densities approximately 5 times larger in torch mode. These spectra are further analysed as illustrated in Fig. 8.7 d) and e), which present results from approximating the line spectra as Gaussian distributions. Figure 8.7 d) visualises obtained peak energies of the electron beams, which feature $\overline{W}_T \approx 0.78 \pm 0.23\,\mathrm{GeV}$ in torch mode and $\overline{W}_{DC} \approx 1.29 \pm 0.32\,\mathrm{GeV}$ in dark current mode. Witness beams from torch injection thus exhibit $\overline{W}_T/\overline{W}_{DC} \approx 60\,\%$ lower peak energies. Such differences may arise from different acceleration lengths and/or trapping of the witness beams into different phases of the wake and/or beam loading due to the high charges injected in torch mode. The latter seems to be the dominating effect, which is supported by the simulation with significant load in Fig. 8.6 c3) and the simulation with low load in Fig. 8.6 b3). In these simulations, the relative energy difference amounts to $71\,\%$, a value similar to $\overline{W}_T/\overline{W}_{DC}$ in the experiment. However, Fig. 8.6 b3) yields higher witness beam charges than dark current injected during the experiment. Therefore, the beam load most

likely modifies the accelerating fields differently. The presence of dark current in the line spectra of the torch mode further suggests that dark current is trapped upstream of the interaction point, as injection is otherwise prohibited by the strong space charge forces of the torch-injected beam. The r.m.s. width of the electron spectra is visualised in Fig. 8.7 e), where $\sigma_{DC} \approx 0.09 \pm 0.05\,GeV$ and $\sigma_T \approx 0.05 \pm 0.03\,GeV$. These results follow the previous discussion for peak energies. The larger energy spread in dark current mode may further be attributed to less localised injection compared to the torch mode. The corresponding relative energy spread amounts to $\sigma_T/\overline{W}_T \approx 6\,\%$ in torch mode and $\sigma_{DC}/\overline{W}_{DC} \approx 7\,\%$ in dark current mode and is therefore similar in both cases. However, dark current spectra exhibit peak energies closer to the spectrometer's imaging energy of 1.7 GeV [1]. The measurement hence overestimates σ_T stronger than σ_{DC}, such that torch-injected beams are expected to have narrower spectra.

While dark current would be eliminated for applications, here the dark current offered an advantage for analysis. It allowed for comparing both modes of beam production and highlighted the superior reproducibility of beams generated by the plasma torch injector. In future experiments it might even be profitable to further exploit the injection of dark current for probing the evolution of the torch generated beam component. However, for reliable and controlled injection, dark current must be avoided, such that the witness beam distribution is fully generated and determined by the plasma torch. This necessitates an improved plasma channel and driver matching in addition to further stabilisation of the injector as discussed in Section 8.9.

8.8 INJECTOR MODES ON THE TIMING TRANSITION

The transition in Fig. 8.7 c) resembles a complex overlay of different injection mechanisms and understanding its formation requires further elaboration. For instance, the timing window given by the approximately linear increase in charge can be estimated by considering two injection extrema. First, the TOA mapping to the high-charge level occurs for direct laser-generation of electrons approximately at the zero-crossing of the wakefield (see Fig. 8.7 a), c) and [44]). This point is located at the centre of the blowout, i.e. at $\xi_1 \approx \lambda_p/2$. Second, the TOA on the low-charge plateau corresponds to ceasing injection on the transition, which occurs when the injector laser misses the blowout vertex at $\xi_2 \approx \lambda_p$. The timing range is thus given by $\Delta TOA \approx (\xi_2 - \xi_1)/c \approx \lambda_p/2c \approx 0.2\,ps$ in good agreement with Fig. 8.7 c) and [44]. This further implies $\Delta TOA \propto 1/\sqrt{n_{ch}}$ such that ΔTOA can be changed by adapting the density of the plasma channel. This may be beneficial for designing plasma torch injectors with long transitions such that the TOA precisely controls the injected charge and the produced witness beam structure.

It is further possible to disentangle different injection dynamics occurring on the timing transition by investigating the PIC simulations shown in Fig. 8.7 c) in greater detail. For this, the initial positions of all trapped particles are extracted from the simulation.

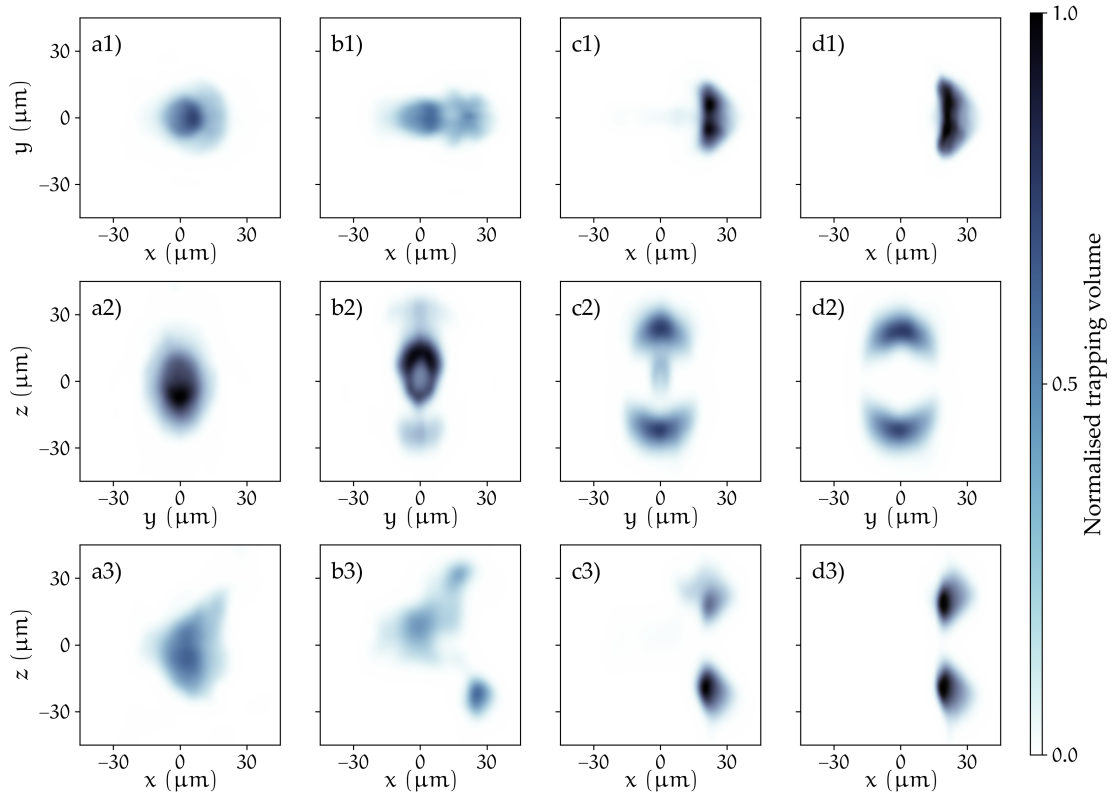

Figure 8.8: Timing transition of the trapping volume from the plasma photocathode towards plasma torch mode. a) to d) represent results from PIC simulations with TOA $= 0.18, -0.1, -0.2$ and -0.3 ps shown in Fig. 8.7 c). Visualised are the initial witness densities projected along the torch symmetry axis (top row), along the PWFA propagation direction (centre row) and the direction perpendicular to both (bottom row).

Projecting these positions along one axis and calculating the planar particle density using a kernel density estimation algorithm [132] then yields the TRAPPING VOLUME n_{trap}. It takes on various forms characteristic to the injection process. Figure 8.8 illustrates n_{trap} for different TOAs. Here, different rows correspond to the initial witness positions projected along the torch symmetry axis (top row), along the PWFA propagation direction (centre row) and the direction perpendicular to both (bottom row).

Figure 8.8 a) visualises n_{trap} for TOA $= 0.18$ ps, which is located just at the beginning of the high charge plateau in Fig. 8.7 c). For this timing, injected charge clearly originates from positions around the driver orbit $y = z = 0$. Consequently, the witness charge of 496 pC is solely formed of electrons generated from ionisation inside the blowout, i.e. the plasma photocathode mechanism [74]. Small asymmetries occur in Figure 8.8 a3), the plane parallel to the propagation direction of the torch laser and most likely originates from the wake's motion during injection. The trapping volume changes its appearance when reducing the TOA, i.e. further approaching the plasma torch mode. For instance at TOA $= -0.10$ ps, crescent satellites form in the head-on view visualised in Fig. 8.8 b2), and more generally the spherical symmetry of the trapping volume is broken. However,

the majority of charge still injects from central positions, but is re-distributed. In this case, the witness charge amounts to 472 pC, which includes 17 % of electrons originating from the plasma channel. This indicates the onset of wave breaking with signatures around $z \approx -25\,\mu m$ in Fig. 8.8 b2) and b3). The crescent satellites continue to develop for later timings as shown in Fig. 8.8 c) for $TOA = -0.2\,ps$. Injection from the driver axis contributes only small fractions of the 466 pC, which is now dominated by 64 % charge stemming from the plasma channel. The last case illustrated in Fig. 8.8 c) matches $TOA = -0.3\,pC$ and represents a regime of pure plasma torch injection similar to the fully formed injectors in Fig. 8.6. Here, 82 % of the 479 pC witness charge originate from the pre-ionised plasma channel. The yz-plane of this trapping volume exhibits a ring shape characteristic for injection triggered by transverse wave breaking [46, 49, 114], where no charge originates from the driver orbit.

As established by Fig. 8.8, the trapping volume n_{trap} allows for distinguishing plasma torch and plasma photocathode injection, which seamlessly transition in the 90 degree laser geometry. However, the transition in Fig. 8.7 c) does not mark the transition of both injector modes. It rather relates to the ceasing effect of the plasma photocathode, i.e. marks the transition from ionising into the first wake period to ionisation when the first wake period passed already as discussed in context of Fig. 8.7 a). This mode of injection then transitions to plasma torch injection at the first part of the high-charge plateau. Remarkably, both modes of injection yield similar amounts of trapped charge. This is likely due to the fact that the blowout cannot sustain larger numbers of electrons. This is confirmed by [66, 103] that estimates the maximum charge the blowout can sustain $Q_{max} \simeq e k_p^2 R^3/30\, r_e \approx 500\,pC$, where r_e and R are the classical electron radius and the blowout radius, respectively.

Further investigations in Chapter 9 reveal that the trapping volume n_{trap} contains information about the geometry of the plasma torch and the blowout, such that its appearance encodes the witness beam's initial conditions. Controlling n_{trap} therefore allows for manipulating the trapped electron population.

8.9 STABILITY OF THE PLASMA TORCH INJECTOR

As outlined in Section 8.7, injection in plasma torch mode can be decoupled from shot-to-shot fluctuations of TOA, when ensuring that $-10\,ps < TOA < 0\,ps$, i.e. when operating in the fully formed regime without expansion processes (see Section 3.3). Nevertheless, such timings show significant charge fluctuations in the experimental data shown in Fig. 8.7 b) - e). On the one hand, these fluctuations originate from additional dark current, i.e. charge injected by other means. On the other hand, experimental jitters can directly affect the plasma torch injection.

Dark current may originate from ionisation of neutral helium gas by wakefield or driver hot spots [106]. The former occurs at the wake vertex, where the accelerating fields are

maximum. In principle, this is promoted by wide plasma regions. However, simulations suggest that electrons produced in these regions do not accelerate quick enough and most likely escape the first wake period. The vacuum fields of the initial driver beam are per se too low to ionise helium. Yet, the simulation through the full channel indicates that strong interactions between plasma channel and the FACET beam lead to envelope oscillations and hence increased beam densities, which enhances tunnelling probabilities inside the blowout. This particularly occurs at positions x where the channel becomes narrower, e.g. before the interaction point. The drive beam distribution and its associated electric fields develop during the beam's propagation through centimetres of the plasma channel as already discussed at the beginning of Section 8.6. Therefore, they are susceptible to the initial beam parameters and the distribution of the plasma channel. Fluctuations of either the initial beam or the channel distribution hence result in varying plasma dynamics and alter the production of dark current.

The experimental charge fluctuations directly affecting the torch injector can be categorised into parameter jitters and alignment jitters. The former includes variations in extent, charge and focusing of the driver as well as energy and focusing instabilities of the pre-ionisation and torch laser pulses. These fluctuations usually result from linac or laser drifts and lead to variations on time scales comparable to those of the data acquisition. The shot-to-shot fluctuations in the TOA scan in Fig. 8.7 therefore originate from other effects. A more likely source are alignment jitters, which cover the misalignment of the pre-ionisation laser with respect to the driver orbit and focusing of the torch laser deviating from the beam orbit and occur from shot-to-shot. Such jitters may arise from pointing variations, which are transported over long beam paths, such that ultimately deviations from the ideal laser/electron beam axis may occur. These deviations may cause poor alignment with laser/electron beam optics.

For instance, a fluctuating pre-ionisation laser would alter the distribution of the plasma channel displayed in Fig. 8.5 and particularly affects the channels width $d_{ch}(x) \neq d_{ch,0}(x)$. Varying channel diameters $d_{ch}(x)$ have an impact on different aspects of the PWFA. First of all, it influences the evolution of the driver beam upstream of the injector. Second, the injection process itself depends on the plasma channel geometry. Finally, $d_{ch}(x)$ affects the evolution of the wakefields downstream of the interaction point and therefore alters the transport and acceleration of the generated electron beam. To study these effects, the PIC simulations shown in Fig. 8.6 c) are modified to include variations of the plasma channel's width $d_{ch}(x) = \kappa \times d_{ch,0}$ differing from the experimental baseline case $d_{ch,0}$ shown in Fig. 8.5. Narrower channel formations $\kappa < 1$ and wider channels with $\kappa > 1$ are studied. To avoid the computationally costly beam transport from $x = -0.2\,\mathrm{m}$ to the interaction point, simulations from Fig. 8.6 c) have been restarted approximately $1\,\mathrm{mm}$ upstream of $x \approx 0$. Then, the plasma channel radius was linearly varied until $d_{ch}(x) = \kappa \times d_{ch,0}(x)$, such that the new wake formation established before the injection position $x \approx 0$.

Figure 8.9 a1) visualises the wake formation after injection for $\kappa = 0.6$, which features a significantly different appearance compared to Fig. 8.6 c3). In the present case, the drive beam expels plasma electrons into regions which are free from plasma ions. Restoring forces acting on plasma electrons are thus diminished and result in elongated blowout formations. This further reduces the accelerating fields similar to a reduced plasma channel density. Plasma torch injection into such compromised blowouts differs compared to previously discussed cases in two ways. First, the increased cavity size resembles a changed charge capacity [66, 103]. Second, and as indicated in Fig. 8.6 and Fig. 8.8, trapped electrons originate from radii close to the maximum blowout radius. For $\kappa \leqslant 1$ these regions are occupied by additional hydrogen plasma, which has been ionised by the injector laser. In this configuration, wave breaking occurs due to hydrogen and helium plasma, i.e. has a larger effect compared to the experimental baseline case $\kappa = 1$.

For $\kappa > 1$ the blowout is increasingly enclosed by the plasma channel as visualised in Fig. 8.9 a2) for $\kappa = 3$. Consequently, the wake narrows, reduces its period and forms according to typical wake excitation. This amplifies the electric field strength compared to the narrow channels with $\kappa \leqslant 1$. As the wake is fully enclosed by the hydrogen plasma channel, the injector laser generates only helium plasma on the path of the PWFA. As a result, only additional helium triggers wave breaking and injection is less efficient compared to the experimental baseline case $\kappa = 1$.

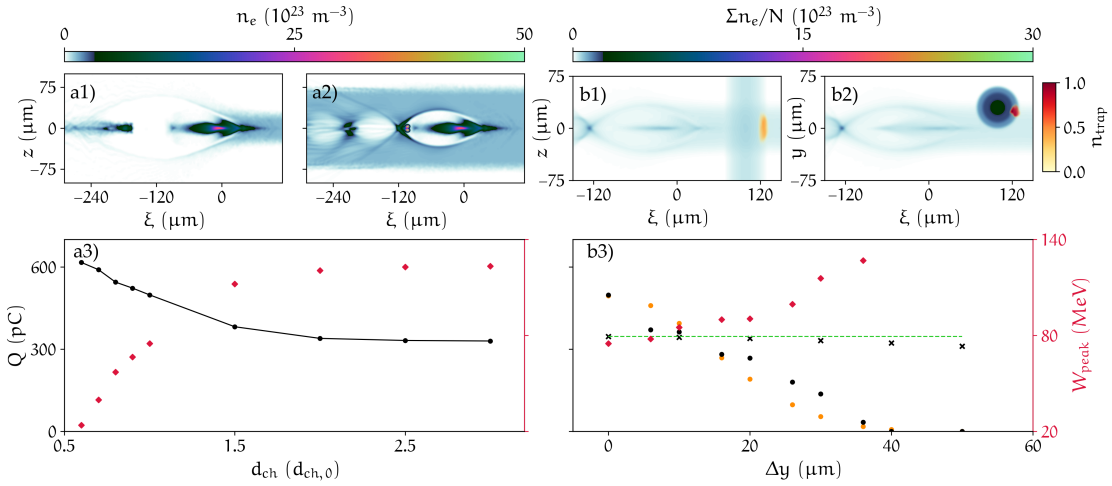

Figure 8.9: PIC study of experimental fluctuations at SLAC FACET. a), jitters related to the plasma channel width $d_{ch} = \kappa \times d_{ch,0}$. a1) and a2), snapshots of PIC simulations employing a narrow ($\kappa = 0.6$) and wide ($\kappa = 3.0$) plasma channel. a3), charge Q (black dots, left axis) and peak energies (red diamonds, right axis) of injected witness beams as function of the channel width. b), jitters originating from relative misalignment between injector laser and the beam orbit. b1) and b2), average projected slice density from PIC simulations with a plasma torch misaligned by $\Delta y = 30\,\mu m$ alongside the corresponding trapping volume n_{trap}. b3) charge Q (black dots, left axis) and peak energy (red dots, right axis) of injected witness beams from PIC simulations dependent on the relative misalignment Δy. Corresponding evaluation of the phenomenological model Eq. (8.9) is displayed as orange dots. Injected charge from a wide plasma torch generated by $\varepsilon_L = 100\,mJ$, $w_0 = 150\,\mu m$ (black crosses, left axis) and expected behaviour of a transversally infinite plasma slab (dashed green line, left axis).

The full scan of injected witness charge as function of the plasma channel width $d_{ch}(x) = \kappa \times d_{ch,0}(x)$ is displayed in Fig. 8.9 a3). As discussed above, narrow plasma channels increase the injection efficacy and yield larger witness charges. For example, $\kappa = 0.6$ generates 616 pC and therefore enhances injection by approximately 24 % compared to the design case $\kappa = 1$. For increased $\kappa \geqslant 2$, in contrast, injected charge reduces by 34 % and saturates at approximately 330 pC. For narrow plasma channels, the injection process strongly couples to the channel distribution, which offers to produce witness beams of larger charge, but suffers from fluctuations of the pre-ionisation laser. To achieve maximum injection reproducibility, plasma channels much wider than the blowout radius are required, such that injection remains stable even under varying channel diameters d_{ch}.

After injection, the channel formation further affects the acceleration process. Wide channels boost the accelerating fields as opposed to narrow channels, which lead to reduced field strengths. Due to the channel's bead-chain geometry, the fields further vary with the laboratory co-ordinate x, which is particularly pronounced for narrow plasma channels $\kappa < 1$. These effects are reflected by the peak kinetic energies of injected electron beams as shown in Fig. 8.9 a3) (red diamonds). This behaviour is dominated by stronger beam loading for high witness charges in combination with weaker blowouts from narrow channels. Again, these values saturate for $\kappa \geqslant 2$, which implies that operating with wide channels decouples both, injection and acceleration from small variations in channel generation. To achieve reliable injection in experiments, wide plasma channels are inevitable. In case of high control over the pre-ionisation laser, however, these effects may be exploited for increased electron yield.

Similar to the focusing of the pre-ionisation laser, the injector laser may be subject to parametric jitters leading to varying density distributions of the plasma torch. This is investigated by applying the ADK formalism outlined in Section 8.4 to a range of laser parameters $\varepsilon_L = 5.0 \pm 0.5$ mJ and $\sigma_L = 20 \pm 2\,\mu$m. Singly ionising helium is found to be stable under these variations and yield deviations of r_{flat} and l_{ramp} in sub-µm range and no change in the degree of ionisation $n_T/n_{T,0}$. This stability can be attributed to the full depletion of this state and therefore resembles negligible jitter contributions in this case. However, the second level of helium, which is responsible for significantly increased injection as visualised in the energy scan in Fig. 8.6, displays stronger dependencies on the laser parameters, which are shown in Table 8.3. These results indicate that fluctuating laser parameters and focusing affect the generation of the plasma torch. Particularly a varying density gradient through Δl_{ramp} strongly impacts the whole torch injector as discussed in Chapter 9. The phenomenological trapping model derived in Section 8.5 is employed for the full plasma torch distributions resulting from the jittering laser parameters and the charge variation ΔQ_M is shown in Table 8.3. Charge variations as large as 13 % are found, whereas reduced torch gradients lead to increased charge and vice versa. Stable generation of the plasma torch thus necessitates precise control over

the laser parameters per shot, or designing the ionisation such that all ionisation levels are depleted by far. The latter is limited by plasma heating and expansion processes as discussed in Section 3.3. However, these estimates are based on perfect Gaussian focusing and deviations under experimental conditions may further originate from other sources, e.g. from astigmatic laser beams.

Table 8.3: Variation of the plasma torch distribution due to injector laser jitter. Shown are the relative change of the core radius Δr_{flat}, ramp length Δl_{ramp} and peak density $\Delta n_T/n_{T,0}$ for the He^{2+} component resulting from 10 % variation in injector pulse energy ε_L and spot size w_0. The relative charge variation ΔQ_M is calculated for the full plasma torch distribution with the phenomenological trapping model in Eq. (8.9).

	Δr_{flat}	Δl_{ramp}	$\Delta n_T/n_{T,0}$	ΔQ_M
$\varepsilon_L = 5 \pm 0.5$ mJ	$+23\,\%$ $-30\,\%$	$-10\,\%$ $+12\,\%$	$+0\,\%$ $-1\,\%$	$+9\,\%$ $-13\,\%$
$w_0 = 20 \pm 2\,\mu m$	$-50\,\%$ $+33\,\%$	$+35\,\%$ $-25\,\%$	$-4\,\%$ $+0\,\%$	$-13\,\%$ $+5\,\%$

Another jitter source relates to the injector laser's spatial alignment with respect to the driver orbit. This may result from the pointing instability of the torch laser, which has been quantified as r.m.s. fluctuations of approximately 8 µm [87]. On a shot-to-shot basis, this results in plasma spikes that are transversely shifted by Δy. The misalignment Δy is implemented in the PIC simulations shown in Fig. 8.9 b). Figure 8.9 b1) and b2) visualise the average projected slice densities $\sum n_e/N$, where N denotes the total number of slices and the summation accounts for the projection in y or z-direction. Shown is the case $\Delta y = 30\,\mu m$ before injection. The finite extent of the plasma torch implies that misalignments significantly change the injection cross section. In this example, the plasma torch extends to regions $0 < y < 60\,\mu m$ and consequently triggers wave breaking only in these regions. Trapped electrons thus originate solely from $y > 0$ as further indicated by the trapping volume in Fig. 8.9 b2). This has some interesting implications, as witness electrons enter the plasma accelerator via one half of the blowout. The resulting witness beam hence breaks the axial symmetry inherent to typical downramp injected electron beams and performs betatron oscillations triggered by the misalignment. A more detailed study may reveal correlations between Δy and the resulting betatron amplitude and could be interesting for controlled x-ray generation [33].

The fact that Δy varies the intersecting volumes of n_T and E_ξ further supports the approach of the phenomenological model in Eq. (8.9), which is evaluated as function of the misalignment Δy. Figure 8.9 b3) displays the results as orange dots alongside the charge values from PIC simulations (black dots). Both show the same trend of diminished trapping as Δy increases, which ceases completely for misalignments approaching the nominal extent of the torch plus the maximum blowout radius. For the injector jitter of approximately 8 µm present at SLAC FACET [87], a charge fluctuation of 130 pC can be determined from the simulations corresponding to relative variations of $\approx 26\,\%$. The

simulation results further feature regions $\Delta y = 6\,\mu m$ to $10\,\mu m$ and $\Delta y = 16\,\mu m$ to $20\,\mu m$ with small reduction of charge. This may be attributed to the vanishing impact of different ionisation levels, which exhibit $r_{flat} \approx 19.4\,\mu m$ for helium and $r_{flat} \approx 5.6\,\mu m$ for He^{2+}.

The acceleration of witness beams from misaligned plasma torches then depends on the varying amount of trapped charge. This is reflected by the peak energies of the witness beams shown as red diamonds in Fig. 8.9 b3). However, to stabilise injection and acceleration against misalignments of the plasma spike, an approach similar to the channel width helps. Another misalignment scan is therefore conducted including an injector laser with $\varepsilon_L = 100\,mJ$ and $w_0 = 150\,\mu m$ and other parameters as before. This results in approximately five times lower peak intensities compared to the previous case and thus readily satisfies the ADK requirements discussed in Section 8.3. These laser parameters cause full depletion of hydrogen and helium such that $r_{flat,H^+} \approx 180.9\,\mu m$, $l_{ramp,H^+} \approx 27.8\,\mu m$ and $r_{flat,He^+} \approx 98.5\,\mu m$, $l_{ramp,He^+} \approx 47.8\,\mu m$, but generate only $2\,\%$ of He^{2+}, which is therefore negligible. Employing these fully ionised torch components further relaxes the potential parametric jitter of the injector laser as discussed before. Implementing this wide plasma torch in PIC simulations in addition to a wide plasma channel with $d_{ch} = 3 \times d_{ch,0}$, another misalignment scan is conducted and shown in Fig. 8.9 b3) (black crosses, left axis). Contrary to the previous case, this configuration yields reduced witness charges due to the negligible He^{2+} component of the injector. Here however, Q is almost unaffected by misalignments. For instance, $\Delta y = 20\,\mu m$ only results in approximately $6.5\,pC$ ($\widehat{=}2\,\%$) reduction of witness charge. This exemplary plasma torch configuration is therefore resilient against parametric fluctuations of the pre-ionisation and injector lasers as well as the misalignment of the injector laser, which stabilises both, the injector and the acceleration section of the PWFA.

8.10 SUMMARY

This chapter investigated different aspects of the plasma torch PWFA at SLAC FACET. The tunable generation of plasma spikes via tunnelling ionisation was considered and a parametric description through Eq. (8.3) was introduced, which finds further application in the systematic simulation study in the next chapter.

A phenomenological model, which quantifies torch-injected charge, was derived and verified against PIC simulations and experimental measurements. It yields good agreement for fully formed, timing-dependent and misaligned torch injection in Sections 8.6, 8.7 and 8.9 and represents a new perspective on density downramp injection: the interaction cross section of the wakefield and the density transition, or trapping volume n_{trap}, plays a major role in the injection process. It can be manipulated by the torch injector, e.g. by transversely shifting the density spike, resulting in injection that is restricted to one half of the wakefield. Further development of the phenomenological model may predict

n_{trap} or other witness beam properties, such as the beam length. Moreover, Eq. (8.9) may allow for modelling injection from the plasma photocathode as indicated by the mixed regime on the timing transition.

Furthermore, the plasma torch injection at SLAC FACET has been studied comprehensively by PIC simulations. The injector's tunability with varying injector energy and TOA has been established. An analysis of various jitter sources reveals the impact of experimental limitations encountered during the proof of concept experiments at SLAC FACET. The channel formation and the misalignment of the injector laser were found to bear the largest potential for improvement. Fluctuations of these components can lead to varying witness charges by hundreds of pC and influences the witness beam energy significantly as observed in the experiment. These jitter sources can be eliminated by wider plasma channels and wider plasma torches, both of which can be readily achieved by altering the respective focusing configuration. In case of precise control over the experimental setup, however, these boundary conditions may be exploited for tuning the witness beam properties in a large range. As indicated above, this offers the opportunity for shaping the trapping volume, enabling the generation and exploration of novel beam modalities, which are further investigated in the following chapter.

Part III

NOVEL MODALITIES FROM PLASMA TORCH INJECTORS

After establishing the fundamental laws of plasma torch injection in the context of the proof of concept experiments at SLAC FACET, the following pages are dedicated to new opportunities arising from this scheme. Results of this chapter represent the outcome of studies that were published in [175].

The following investigations assume ideal conditions, e.g. a wide plasma channel as well as a matched driver beam, and focus on unique modalities that can be created by the plasma torch injector. They further serve as guidance for the E-311 experimental campaign at SLAC FACET II and therefore employ the baseline parameters of the FACET II electron driver beam. In this context, pathways towards new beam modalities and high beam quality are demonstrated. It is shown that conventional, gas-based density downramps are a subset of the capabilities of the all-optical plasma torch technique. While conventional downramps represent 1D longitudinal density distributions, the plasma torch enables 4D control of density profiles. This relates to a particular class of trapping volumes, which correspond to unique properties of the resulting electron beams.

9 NOVEL MODALITIES FROM PLASMA TORCH INJECTORS

The phenomenological model, PIC simulations and the proof of concept experiments at SLAC FACET are a consistent foundation for exploring the capabilities of the plasma torch injector further. The restrictive experimental boundary conditions encountered at FACET, such as plasma channel constraints and spatio-temporal laser and beam fluctuations can be overcome, or substantially reduced by state-of-the-art facilities, such as the upcoming FACET II facility. In the following, the newly developed trapping model and PIC simulations are used to examine realistic scenarios that could be implemented in the near future.

In all simulations, the pre-ionised plasma channel fully encloses the plasma wave, which could be achieved by increasing the focal length of the axicon system and operation at higher pre-ionisation laser powers. An increased plasma channel density $n_{ch} = 6\times10^{23}$ m^{-3} is employed, such that $\lambda_p \approx 40\,\mu m$. This enables higher accelerating fields and reduces the expected witness beam emittance, which scales approximately as $\propto \lambda_p$ [171]. At such elevated plasma densities, the wakefields are strong enough for tunnel ionising the first ionisation level of helium, which can inject dark current [106]. To avoid such effects, the plasma channel is formed of fully ionised hydrogen and the first level of helium. The remaining helium ions constitute the medium for plasma torch generation and do not lead to dark current injection due to the large ionisation potential $\varepsilon_{ion} = 54.4\,eV$ and $Z = 2$. Below, the distribution of the plasma torch is no longer calculated from ionisation rates, but parametrically varied through Eq. (8.3). This allows for systematically examining the impact of the torch geometry on the injection process. To reduce the computational cost and for the sake of better comparability with the previous chapter, only beams are studied that are trapped into the first wake period.

The design parameters for electron beams available at SLAC FACET II [191] serve as a guideline for the driver properties of the following study and are adapted to avoid dark current production. At initialisation, the drive beam forms a Gaussian distribution with the parameters shown in Table 9.1.

Table 9.1: Driver beam properties based on the design parameters at SLAC FACET II [191].

Beam charge	$Q_D = 0.6\,nC$
r.m.s. length	$\sigma_x = 7.5\,\mu m$
r.m.s. width	$\sigma_y = \sigma_z = 3\,\mu m$
Beam energy	$W_D = 10\,GeV$
Energy spread	$\Delta W/W_D = 0.02$
Normalised emittance	$\varepsilon_{n,y} = \varepsilon_{n,z} = 100\,mm\,mrad$

The beam width is matched to the plasma channel density as outlined in Eq. (4.6) to avoid transverse envelope oscillations, which results in the blowout with maximum radius $r_b \approx 15\,\mu m$. Furthermore, the resolution of the numerical grid is improved to $0.25\,\mu m$ and $0.5\,\mu m$ in longitudinal and transverse direction, respectively, and a modified Yee solver suppressing numerical Cherenkov radiation is implemented [39]. The electron drive beam and plasma channel are formed of 16 PPC and 8 PPC, whereas the plasma distribution is sampled by 16 PPC in the region of the plasma torch, which is located at $x_T = 1\,mm$, i.e. $1\,mm$ downstream of the initialisation point of the simulation. This simulation setup sets the foundations for the systematic investigation of the plasma torch scheme outlined in this chapter.

First, the impact of the ramp length l_{ramp} on the injection process is addressed, while keeping the peak density of the plasma torch constant at $n_{T,0} = 0.5 \times n_{ch}$. Here, two extreme cases are of particular interest, namely torches with wide core $r_{flat} > r_b$ and torches with narrow core $r_{flat} < r_b$ compared to the maximum blowout radius r_b.

9.1 WIDE PLASMA TORCHES

The first scenario employs torch density distributions with $r_{flat} = 40\,\mu m > r_b \approx 15\,\mu m$, i.e. wider than the blowout and hence contrasts with the scenarios found at SLAC FACET.

Figure 9.1 a) illustrates this configuration for one snapshot of the electron densities from 3D PIC simulations along with their central slices shown at the bottom. The drive beam (black) excites a blowout (green) and approaches the plasma torch (orange). Here, the torch distribution exceeds the size of the plasma wake in both the longitudinal and the transverse dimensions and induces wave breaking across the full cross section of the wakefield. Furthermore, the transverse extent of the wake is small compared to the plasma torch radius of curvature, such that injection occurs approximately symmetric in the transverse plane of the PWFA, which is confirmed later on.

The ramp length is varied from $l_{ramp} = 10\,\mu m$, which is shown in Fig. 9.1 a), to $l_{ramp} = 400\,\mu m$. Depending on l_{ramp}, different regimes of wave breaking occur similar to Fig. 6.1. The corresponding injection mechanisms have already been observed by Bulanov for gentle ramps in LWFA [23] and by Suk for short ramps in PWFA [166]. Ekerfelt et al. identified both regimes for LWFA downramp injectors [50], which are confirmed below for PWFAs.

For long ramps $l_{ramp} > \lambda_p$, injection occurs adiabatically at the rear of the expanding blowout as shown by the trajectories in Fig. 9.1 b1). Such electrons experience weak focusing fields and therefore inherit small transverse momenta during injection. Simulations reveal that this gentle injection leads to a linear mapping between initial position in the laboratory frame x and resulting trapping position. They further indicate the onset of witness beam hosing [119] starting at the downstream end of the injector resulting in beam centroid shifts as displayed in Fig. 9.1 b1) for $l_{ramp} = 200\,\mu m$. Hosing can occur

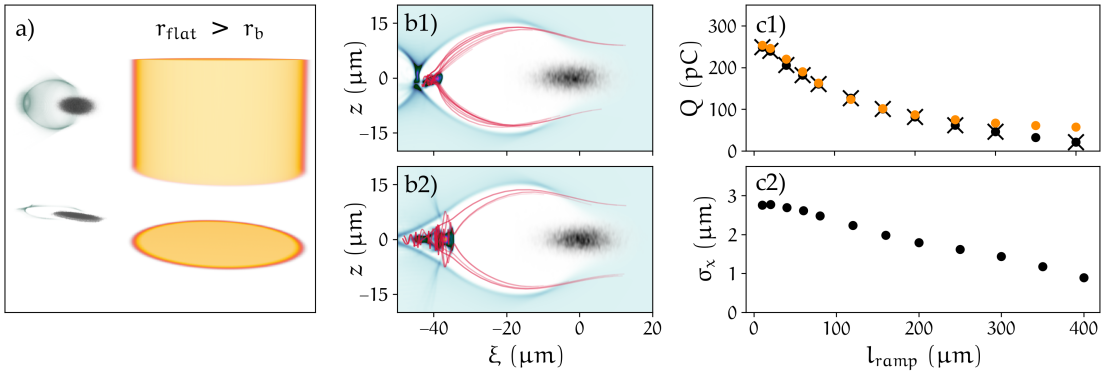

Figure 9.1: Injector employing wide plasma torches $r_{flat} = 40\,\mu m > r_b$. a), 3D visualisation of electron densities from PIC simulations before injection along with central slices projected to the bottom. The electron drive beam (black) excites a blowout (green) and approaches the plasma torch (orange). b), trajectories of witness electrons (red) for b1) $l_{ramp} = 200\,\mu m$ and b2) $l_{ramp} = 10\,\mu m$. c1), injected witness charge Q as function of l_{ramp} for cylindric plasma torches (cf. Eq. (8.3)) from PIC simulations (black dots), phenomenological model Eq. (8.9) (orange dots) and simulation results for plasma slabs (cf.Eq. (9.1), black crosses). c2), r.m.s. length σ_x of witness beams from cylindric plasma torches dependent on l_{ramp}.

due to initial transverse asymmetries of particle beams [118], such that this may be the ramification of the irregularly distributed trapping volume, which is addressed in context of Fig. 9.2.

For short ramps $l_{ramp} < \lambda_p$, the blowout collapses off-axis providing electrons for trapping, while the expanding blowout forms around them. These electrons then experience the strong, focusing wakefields, such that they quickly accelerate towards the drive beam axis and overshoot. The resulting witness beams typically inherit larger transverse momenta and consequently perform betatron oscillations with larger amplitude than the previous case. The trajectories in Fig. 9.1 b2) support this argument and further feature deflections of the witness electrons as they approach the driver axis for the first time. This may be attributed to space charge forces of initially trapped electrons that repel subsequent particles, which are then trapped closer to the wake vertex. The generated witness beam exhibits large charge densities and therefore causes an elongation of the blowout due to its space charge. This regime of wave breaking resembles a rapid and violent process which can enable localised injection of immense numbers of electrons. The ultra-short and controllable density gradients provided by the plasma torch scheme are therefore particularly well suited for injection in PWFAs driven by low-current electron beams, as recently shown by Knetsch et al. [92].

In the cases studied so far, the plasma torch adopts the radial symmetry of the Gaussian injector laser propagating in z-direction, which produces a plasma cylinder. In contrast, conventional downramp techniques produce approximately axially symmetric density

profiles in x-direction. To compare injection from both geometries, the plasma slab distribution

$$\frac{n_{Slab}}{n_{Slab,0}}(x,y,z) = \begin{cases} 1 & : |x| < r_{flat} \\ \cos^2\left(\frac{\pi}{2}\frac{|x|-r_{flat}}{l_{ramp}}\right) & : r_{flat} \leqslant |x| < r_{flat} + l_{ramp} \\ 0 & : r_{flat} + l_{ramp} < |x|. \end{cases} \tag{9.1}$$

is implemented in PIC simulations. Equation (9.1) approximates hydrodynamically generated, conventional density downramps to some extent and could also be produced in all-optical fashion by focusing a laser pulse with cylindrical optics. The same ramp scan is performed with n_{Slab} and similar injection dynamics are found compared to cylindrical plasma torches. Figure 9.1 c1) illustrates the witness charge injected from the plasma torch (black dots) and the plasma slab (black crosses) as function of l_{ramp}. The results equal, which suggests that the plasma torch can mimic conventional downramp injectors for $r_{flat} > r_b$. In this case, the effect of the radius of curvature of the plasma torch on the injected charge is therefore negligible. Figure 9.1 c1) further reflects typical behaviour of density downramp injection, where gentle gradients inject comparatively low witness charges and steep gradients maximise trapped charge [167]. The same trend is obtained from the phenomenological trapping model for cylindrical plasma torches (orange dots) and plasma slabs (not shown) as shown in Fig. 9.1 c1), which agrees well with the simulations. Yet, larger $l_{ramp} > 200\,\mu m$ systematically overestimate the charge values, which may occur due to the transition to the adiabatic regime of injection. Here, electrons no longer break transversally into the blowout and experience the accelerating fields close to the centre of the blowout, but enter the accelerator at the wake vertex. Another common downramp scaling can be observed in these simulations as visualised in Fig. 9.1 c2). It is found that longer ramps correlate to smaller witness beam r.m.s. lengths σ_x [117]. This may be the result of two effects. Firstly and as further discussed in Fig. 9.2, short density gradients induce trapping throughout the full downramp length, i.e. trapping starts in the plateau region of the density spike. At this position, the blowout has not yet expanded, such that the front of the witness beam forms at the vertex of the plasma wave determined by the peak density $n_{ch} + n_{T,0}$. Conversely, long density ramps may only trigger injection at positions where the gradient of the cosine ramps is sufficient, i.e. further downstream (cf. trapping volumes Fig. 9.2 a1) and Fig. 9.2 b1)). The witness beam thus begins to form at lower densities corresponding to an expanded blowout. This causes smaller σ_x in agreement with [117]. Secondly, injection of high charges induces strong space charge forces during injection, such that the blowout elongates and therefore creates capacity for more trailing electrons. This effect is exploited in Section 9.5 for designing injection from multiple plasma torches.

The different trapping dynamics illustrated in Fig. 9.1 are further reflected by unlike trapping volumes n_{trap}. These are calculated analogously to Section 8.8 and are visualised

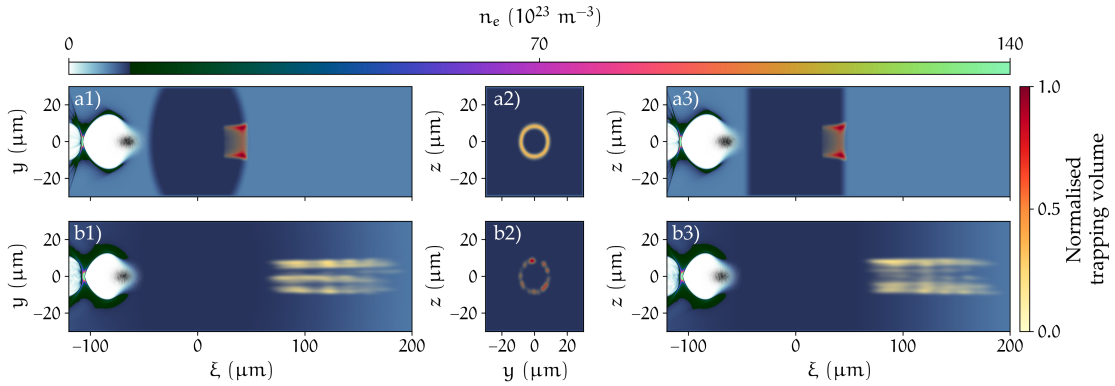

Figure 9.2: Trapping volumes n_{trap} for wide plasma torches with $r_{flat} = 40\,\mu m > r_b$ and symmetric driver. a) and b) correspond to $l_{ramp} = 10\,\mu m$ and $l_{ramp} = 200\,\mu m$, respectively. Illustrated are slices of electron densities n_e for $z = 0$ (left column), $\xi = 0$ (centre column) and $y = 0$ (right column). The trapping volume is normalised in each column. This figure is adapted from [175].

in Fig. 9.2. Figure 9.2 a) and b) illustrate the cases $l_{ramp} = 10\,\mu m$ and $l_{ramp} = 200\,\mu m$, respectively, with normalised trapping volumes in each column. The columns further display plasma densities in the central planes of the simulations. The drive beam (black) propagates to the right and the electron densities are colour coded white-blue.

For short ramps, Fig. 9.2 a1) and a3) indicate that witness particles are trapped within a longitudinal range of $30\,\mu m > l_{ramp}$ beginning upstream of the downramp. The ξy and ξz planes result in similar trapping volumes, which further supports that the curvature of the plasma torch has negligible impact on injection in this case. Furthermore, the radial expansion of the blowout on the density downramp leads to symmetric widening of the trapping volume dependent on ξ. This radial symmetry is particularly visible in the yz-plane as shown in Fig. 9.2 a2). It highlights that electrons are injected exclusively from positions close to the maximum blowout radius as observed before by trajectories (cf. Fig. 8.6 and Fig. 9.1 b)), such that the trapping volume forms a ring in this plane.

In contrast, the trapping volume changes in the gentle downramp regime as illustrated in Fig. 9.2 b). Here, injection occurs within a fraction of the downramp over approximately $137\,\mu m < l_{ramp}$ and from an irregular volume. It is composed of filaments and suggest that particle trapping is restricted to regions exceeding the trapping threshold, i.e. it is sensitive to small variations of the wakefield. The transverse irregularity of this trapping volume produces transversely asymmetric witness beams that can be prone to the hosing instability [119] as visualised in Fig. 9.1 b1). Repeating this simulation with increased resolution leaves the appearance of the filaments intact, which may suggest the presence of physical effects as supported by similar observations in LWFA self-injection [46]. However, further investigations are required to fully exclude artificial sources of beam asymmetries.

Witness beams originating from the wide plasma torch with $l_{ramp} = 10\,\mu m$ and $l_{ramp} = 200\,\mu m$ further exhibit high quality as illustrated in Fig. 9.3. Here, the injected

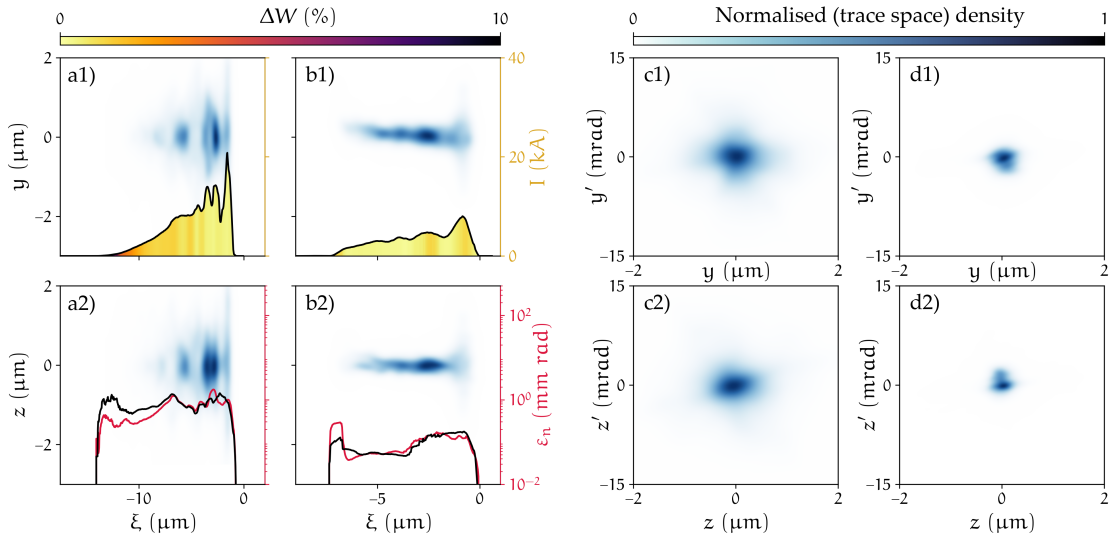

Figure 9.3: Properties of electron beams generated by wide plasma torches with $r_{flat} = 40\,\mu m > r_b$. Shown are the cases of $l_{ramp} = 10\,\mu m$ and $l_{ramp} = 200\,\mu m$, respectively. Both beams are extracted from the simulation after reaching an average kinetic energy of 100 MeV. Due to different beam loading, this energy is reached after the acceleration distance of $\approx 1.8\,mm$ ($l_{ramp} = 10\,\mu m$) and $\approx 1.3\,mm$ ($l_{ramp} = 200\,\mu m$). a) and b), normalised densities of the real space distributions for $l_{ramp} = 10\,\mu m$ and $l_{ramp} = 200\,\mu m$, respectively, with colours according to the top right colour bar. a1) and b1), slice current values of respective beams (right axis) coloured according to their relative energy spread ΔW. a2) and b2), slice normalised emittance values ε_n in y (red) and z (black). c) and d), normalised densities of the transverse trace space of a) and b). This figure is adapted from [175].

beams are shown after they gained average energies exceeding 100 MeV. Figure 9.3 a) and c) correspond to the real space and the trace space of the witness beam injected on the short gradient. It is formed of 256 pC within the r.m.s. length $\sigma_x \approx 2.6\,\mu m$ and sampled by more than 4.8×10^5 macro particles. Fig. 9.3 b) and d) shows the real space and trace space distributions of the electron beam injected by the torch with gentle gradient, which contains 82 pC in $\sigma_x \approx 1.8\,\mu m$ (1.7×10^5 macro particles). For a) and b), both distributions are sorted into longitudinal bins of 30 nm length and smoothed afterwards to obtain the beams slice properties as indicated by the right axis.

The real space distributions in Fig. 9.3 reflect the different dynamics occurring in the two different injection regimes. The breaking with steep ramps as shown in Fig. 9.3 a) spreads charge over a large transverse range, whereas gentle, on-axis breaking as in Fig. 9.3 b) produces a narrow distribution of the electrons. The beam injected on the short ramp exceeds the length of the one generated by the long ramp by a factor of approximately two. As discussed earlier, this may be attributed to space charge effects and may be an intrinsic property of the rapid injection process. This affects the slice currents of the formed beams as shown in Fig. 9.3 a1) and b1) and displays particularly large peak values of approximately 20 kA for the beam produced on the short ramp. Although the rapidly injected beam exhibits a larger σ_x, it features current values larger by a factor of two compared to the beam produced on the gentle gradient. The colour

coding in Fig. 9.3 illustrates slice values of the relative energy spread, which are for both cases of the order of $\sim 1\%$ over a large longitudinal subset of the witness beam.

Figure 9.3 c) and d) visualise the trace spaces of the beams and shows their excellent transverse properties. Both are characterised by single distributions of dense cores and indicate low emittance values particularly for the beam injected on the gentle ramp. This is quantified by the slice normalised emittance values in Fig. 9.3 a2) and b2), where $\varepsilon_{n,y}$ is shown in red and $\varepsilon_{n,z}$ in black. Since the electron population in a) results from breaking of the blowout before the wake vertex, these electrons initially experience the strong focusing fields inherent to the positions close to the sheath. Such electrons obtain comparably large transverse momenta, which is reflected by the total projected emittance $\varepsilon_n \approx 1.5\,\mathrm{mm\,mrad}$ of the beam and the moderately small trace space area in Fig. 9.3 c). The dynamics in Fig. 9.3 b), however, initiate the witness population approximately on-axis, where the transverse fields are small. Thus, the total projected emittance in this case reduces to $\varepsilon_n \approx 0.4\,\mathrm{mm\,mrad}$, i.e. smaller by a factor of approximately 4 compared to a). The slices $-7\,\mu\mathrm{m} < \xi < -3\,\mu\mathrm{m}$ feature 34 % of the beam charge and exceptionally low emittance values of $\leqslant 60\,\mathrm{nm\,rad}$, which contribute to ultra-high slice brightness values $B \approx 10^{18}\,\mathrm{A/m^2\,rad^2}$. This range hence qualifies for demanding high-brightness applications such as next-generation light sources [75].

9.2 NARROW PLASMA TORCHES AND ASYMMETRIC INTERACTIONS

Below, plasma torch injectors with narrow cores $r_{flat} = 2.5\,\mu\mathrm{m} < r_b$ are investigated. Figure 9.4 a) visualises this configuration for the exemplary case $l_{ramp} = 10\,\mu\mathrm{m}$. It indicates that the reduced interaction cross section alters the injection dynamics comparable to misaligned torches (cf. Section 8.9), or temporally incomplete torches (cf. Section 8.7). As in the previous section, the ramp length is varied in the range $l_{ramp} = 10$ to $400\,\mu\mathrm{m}$ and the regimes of adiabatic and rapid injection are identified similar to Fig. 9.1 b). Figure 9.4 b1) displays trajectories from an injector with $l_{ramp} = 200\,\mu\mathrm{m}$, which resemble those of the wide plasma torch in Fig. 9.1 b1). This can be attributed to the fact that in both cases $l_{ramp} \gg r_{flat}$ and $r_{flat} + l_{ramp} \gg r_b$, i.e. the nominal extent of the plasma torch in one plane exceeds that of the blowout by far and the ramps comprise the larger part of the distribution. Consequently, the blowout traverses similar downramp distributions in Figure 9.4 b1) and Fig. 9.1 b1) triggering comparable injection dynamics. This is further confirmed by the amount of injected charge, which is larger for the wide configuration by less than 1 pC. However, trajectories for narrow torches and $l_{ramp} = 10\,\mu\mathrm{m}$ differ from their wide counterparts as illustrated in Fig. 9.4 b2). Here, the electron deflections observed in Fig. 9.1 b2) do not occur, which most likely arises from reduced space charge forces during the trapping process. These trajectories overshoot the driver axis before trapping. The resulting electron paths perfectly describe the swallow

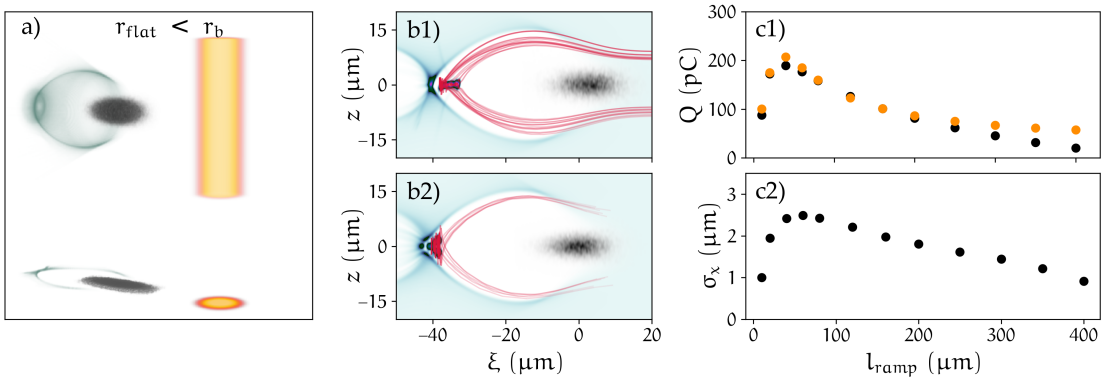

Figure 9.4: Injector employing narrow plasma torches $r_{flat} = 2.5\,\mu m < r_b$: a), 3D visualisation of electron densities from PIC simulations before injection along with central slices projected to the bottom. The electron drive beam (black) excites a blowout (green) and approaches the plasma torch (orange). b), trajectories of witness electrons (red) for b1) $l_{ramp} = 10\,\mu m$ and b2) $l_{ramp} = 200\,\mu m$. c1), injected witness charge Q as function of l_{ramp} for plasma torch injectors from PIC simulations (black dots) and the phenomenological model Eq. (8.9) (orange dots). c2), r.m.s. length σ_x of witness beams dependent on l_{ramp}.

tail formation found by Bulanov [21] (cf. Fig. 6.1) and therefore provides a textbook example of transverse wave breaking.

Figure 9.4 c1) displays injected witness charge as function of the torch ramp length for $r_{flat} = 2.5\,\mu m$. For ramp lengths larger than $40\,\mu m$, $Q(l_{ramp})$ converges towards the behaviour of the wide plasma torch visualised in Fig. 9.1 c1) and becomes identical for ramp lengths much larger than the blowout radius. However, for $l_{ramp} < 40\,\mu m$, the injected charge $Q(l_{ramp})$ clearly differs from Fig. 9.1 c1) and suggests dynamics beyond conventional downramp physics. These can be attributed to longitudinal and transverse effects. The former becomes apparent when recapitulating the trajectories in Fig. 9.4 b), which originate from radii of approximately r_b. For small l_{ramp}, the extent of the plasma spike in y-direction is smaller than r_b causing reduced wave breaking in the xy-plane. However, the plasma torch extends over the whole blowout in z providing density in the xz-plane for wave breaking and injection. This leads to a transversely cropped trapping cross section as visualised by n_{trap} in Fig. 9.5 a) and hence reduces the injected charge. This is further visualised by the trapping volume shown in Fig. 9.5 a2), which no longer describes a ring, but a cropped version of the trapping volume of the wide plasma torch with short gradient as shown in Fig. 9.2 a2). Figure 9.5 a1) and a2) additionally indicate longitudinal effects. While the wide torch with $r_{flat} = 40\,\mu m$ and $l_{ramp} = 10\,\mu m$ triggers injection over a longitudinal distance of $30\,\mu m > l_{ramp}$, the narrow configuration yields $\approx 8\,\mu m < l_{ramp}$. The small volume through $r_{flat} = 2.5\,\mu m$ therefore constitutes a limited charge reservoir and reduces the trapped charge additionally to the transverse cropping. The full ramp scan illustrated in Fig. 9.4 c1) can be reproduced by the phenomenological model through Eq. (8.9) as

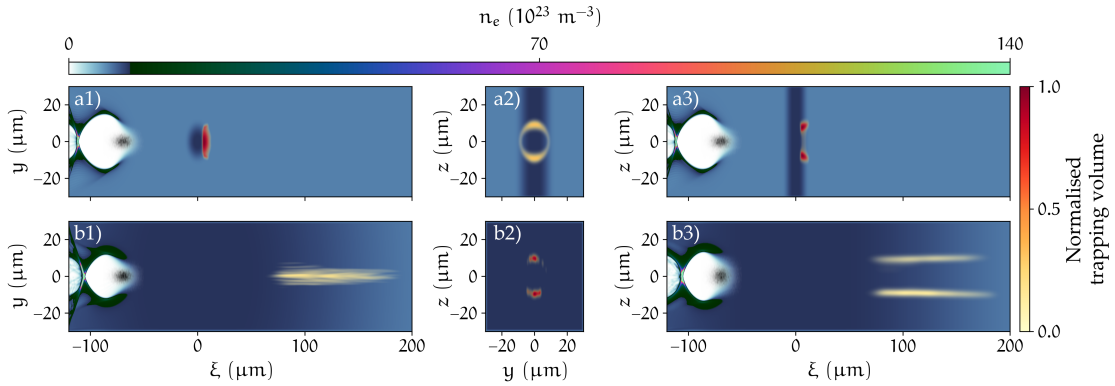

Figure 9.5: Trapping volumes n_{trap} from asymmetric interactions: a), narrow plasma torch composed of $r_{flat} = 2.5\,\mu m$ and $l_{ramp} = 10\,\mu m$. b), wide plasma torch with $r_{flat} = 40\,\mu m$ and $l_{ramp} = 200\,\mu m$ interacting with asymmetric blowout excited by a drive beam with $\sigma_z = 1.5 \times \sigma_y$. Visualisation as in Fig. 9.2. This figure is adapted from [175].

shown by the orange dots. Again, larger $l_{ramp} > 200\,\mu m$ systematically overestimate the charge values due to the transition to the adiabatic regime of injection.

The asymmetric injection further influences the r.m.s. length σ_x of the injected beams as illustrated in Fig. 9.4 c2). Similar to the charge values, $l_{ramp} > 40\,\mu m$ produces beam lengths that converge towards those generated by wide plasma torches. However, the region $l_{ramp} < 40\,\mu m$ deviates from typical downramp behaviour [117] and leads to reduced σ_x. This may be attributed to lower space charge forces during injection (cf. discussion of Fig. 9.1 c2)) resulting from lower witness charges due to the asymmetric interaction.

The structure of the phenomenological model also suggests asymmetric interactions for asymmetric wakefields. These may be the result of inhomogeneous plasma channel distributions together with symmetric drivers, or can originate from asymmetric drive beam distributions. The latter is common in electron beams from linacs, due to compression and focusing techniques, as well as for LWFAs [46, 109], due to effects of the drive laser polarisation. Electron beams from both types of accelerators therefore typically exhibit larger extent of the charge density in one transverse plane than the other. Employing such electron beams as drivers for plasma torch injection may influence injection dynamics and the produced witness beam characteristics significantly. Therefore, the simulation of $r_{flat} = 40\,\mu m$ and $l_{ramp} = 200\,\mu m$ is repeated with the transversely asymmetric drive beam $\sigma_z = 1.5 \times \sigma_y$ resulting in blowout radii $r_{b,z} \approx 1.1 \times r_{b,y}$. This small blowout asymmetry changes the trapping volume considerably as illustrated in Fig. 9.5 b). Now, the trapping filaments are bound to the ξz-plane and only resemble a subsection of the ring structure obtained from the symmetric interaction visualised in Fig. 9.5 b2). In fact, this trapping volume exhibits two populations even more confined than the cropped ring in Fig. 9.5 a). The injected charge observed in the PIC simulation increases by approximately 6 % (Q_M increases by 6 %) compared to the symmetric case. This suggests

that this trapping volume results not only from re-arranging of the distribution in Fig. 9.2 b), but also from the enhanced efficacy of the asymmetric wave breaking process, which only occurs in well-defined regions along the plane of the wakes larger extent (cf. Fig. 9.5 b1) and b3)). Injection from the same asymmetrically excited blowouts has additionally been studied for a plasma torch composed of $r_{flat} = 40\,\mu m$ and $l_{ramp} = 10\,\mu m$. Here, the ring shape is no longer axially symmetric, but increases in the plane of the larger blowout by approximately 20 % and reduces in the perpendicular direction by the same amount [175]. The trapped charge reduces by 10 % (Q_M reduces by 5 %). As expressed by the trapping volume, the initial conditions of this beam only change minimally due to the asymmetric wakefield. The rapid injection regime is therefore more resilient to asymmetric blowouts than the adiabatic regime, which is more sensitive to small variations in the wakefields. Short density downramps may therefore stabilise the output of PWFAs driven by jittering electron beams, e.g. for L2PWFAs.

The trapping volume crystallises the various initial conditions created by the drive beam and the plasma density profile generated by the torch laser. As shown in this section, these can be manipulated, e.g. by breaking the axial symmetry. Breaking this symmetry by asymmetric density distributions is unique to the plasma torch injector and further fosters prospects for imprinting exceptional properties onto the electron beam as discussed in the next section.

9.3 WITNESS BUNCHLETS FROM ASYMMETRIC INJECTION

Injection from narrow plasma torches, or asymmetric wakefields produce trapping volumes n_{trap} with injection via a preferential plane determined by the system's asymmetry as shown in Fig. 9.5. Since n_{trap} defines the initial conditions for witness beam generation, asymmetric electron formations are expected from these configurations. Resulting populations are therefore investigated in greater detail.

Figure 9.6 illustrates properties of the witness beam generated from a narrow plasma torch with $r_{flat} = 2.5\,\mu m$, $l_{ramp} = 10\,\mu m$ corresponding to the trapping volume in Fig. 9.5 a). Here, Fig. 9.6 a) to c) shows one simulation snapshot at a moment where the produced witness beam has been accelerated to a mean energy slightly above 100 MeV. Figure 9.6 a) and b) display two planes of the real space and the transverse trace space, whereas blue and red colouring correspond to particles originating from $z > 0$ and $z < 0$ (cf. Fig. 9.5 a2)), respectively. Both components overlap in the ξy-plane of the real space such that only one is visible in this representation and thus resembles the beam injected by a wide torch as shown in Fig. 9.3 a1). In the ξz-plane, however, large parts of both components are separated indicating the formation of two bunchlet populations, both of which originate from opposing blowout sheaths. The pale part at the back of the beam originates from the transversally cropped region $z \approx 0$ of the trapping volume in Fig. 9.5 a2) and may be eliminated by further reducing r_{flat} and/or l_{ramp}. The

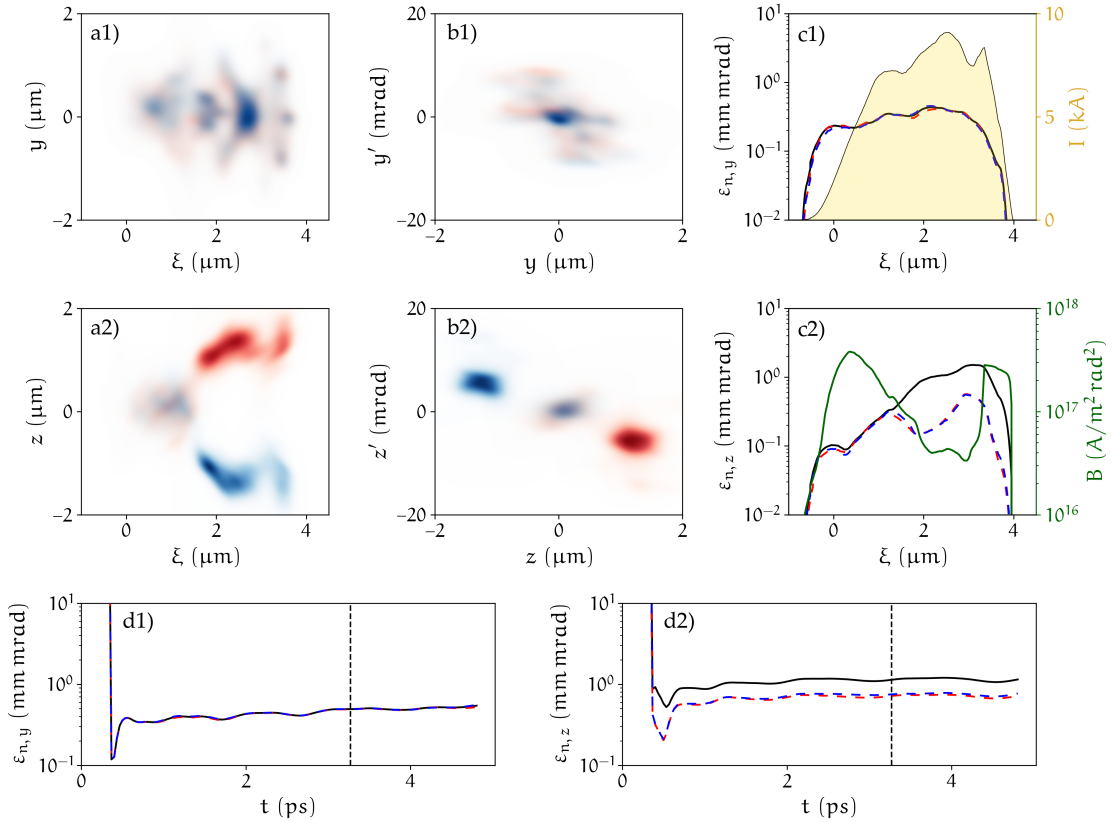

Figure 9.6: Properties of the electron beam generated by a narrow plasma torch injector with $r_{flat} = 2.5\,\mu m$ and $l_{ramp} = 10\,\mu m$. In all panels, red and blue colours denote quantities of beamlets originating from positions $z > 0$ (upper beamlet) and $z < 0$ (lower beamlet), respectively. a), real space representation of the projected witness beam density. b), projected transverse trace space density. c) slice properties of the beam. c1), slice emittance values of the full beam (black), upper beamlet (red) and lower beamlet (blue) and slice currents of the full beam (yellow shade, right axis). c2), slice emittance values as in c1) and brightness of the full beam (green, right axis). d), temporal emittance evolution of both planes for the full beam (black lines) and both beamlets (dashed lines with respective colours). The dashed lines indicate extraction points of a) to c). This figure is adapted from [175].

corresponding trace space in Fig. 9.6 b) reflects the same symmetries. The yy'-plane depicts one distribution where the dense centre populates a small area, surrounded by a scarcely populated region. Conversely, the zz'-plane is occupied by multiple distributions matching those identified in Fig. 9.6 a2). This has consequences as regards the beam's real space and trace space evolution. In terms of the former, Fig. 9.6 b2) describes two electron beamlets that counter-oscillate around each other in the ξz-plane, while oscillations are suppressed in ξy.

In the trace space, both beamlets occupy the same volume in yy' such that in this plane the normalised emittance values of each bunchlet equals that of the full beam $\varepsilon_{n,y} \approx 0.5\,mm\,mrad$. This is further confirmed by the slice emittance values shown in Fig. 9.6 c1), where the emittance of the upper beamlet $\varepsilon_{n,y,1}$ and the lower beamlet $\varepsilon_{n,y,2}$ equal the emittance of the full witness beam $\varepsilon_{n,y}$. These beams are of high

quality, which can be attributed to the cropping of the trapping volume in y and the resulting reduction of initial position spread in this direction. Conversely, in zz' each beamlet approximately occupies a separate trace space volume with emittances $\varepsilon_{n,z,1} \approx 0.7\,\mathrm{mm\,mrad}$ and $\varepsilon_{n,z,2} \approx 0.7\,\mathrm{mm\,mrad}$, respectively, with a total beam emittance of $\varepsilon_{n,z,tot} \approx \sqrt{2}\varepsilon_{n,z,1} \approx \sqrt{2}\varepsilon_{n,z,2} \approx 1.1\,\mathrm{mm\,mrad}$. This configuration is preserved during acceleration as illustrated by the emittance evolution in Fig. 9.6 d). Figure 9.6 c2) further displays the longitudinal distribution of the slice emittance, which shows that these values deviate when comparing the beamlets and the total beam. Separation of the beamlets can therefore result in two beams with further reduced emittance values in the z plane. Combining the emittance values in both planes with the beam's slice current (cf. Fig. 9.6 c1)) results in exceptional slice brightness values of the order of $10^{17}\,\mathrm{A^2/m^2\,rad^2}$ as displayed in Fig. 9.6 c1), which exceeds values of conventional linacs such as the LCLS-II with $B \approx 3 \times 10^{16}\,\mathrm{A/m^2\,rad^2}$ [163].

Slice properties of the witness beam generated by a wide, adiabatic torch injector with $r_{flat} = 40\,\mu\mathrm{m}$, $l_{ramp} = 200\,\mu\mathrm{m}$ in addition to the asymmetric drive beam with $\sigma_z = 1.5 \times \sigma_y$ (cf. Fig. 9.5 b2)) are illustrated in Fig. 9.7. This scenario displays similar symmetries compared to the previously discussed electron population from a narrow plasma torch. However, this beam features inhomogeneities visible in the real space illustrated in Fig. 9.7 a2). These may originate from the filaments in the trapping volume occurring at various initial positions x_i in the laboratory frame. Similar to the symmetrically driven case shown in Fig. 9.3 b), x_i maps approximately linearly to final positions ξ within the beam (cf. Fig. 9.7 a2)). Injection filaments starting at different x_i hence deposit their charge predominantly at discrete positions within the beam forming modulated density patterns. Similar to Fig. 9.6, a minuscule fraction of charge is still injected from $z \approx 0$ (cf. Fig. 9.5 b2)) and can be seen as pale colours in Fig. 9.7 a2). In contrast to the beam from the narrow torch, however, here this feature occurs at the beam's front.

Similar to the narrow plasma torch, the trace space yy' of both beamlets overlaps. This results in approximately equal projected emittance of the bunchlets and the full beam $\varepsilon_{n,y,1} \approx \varepsilon_{n,y,2} \approx \varepsilon_{n,y,tot} \approx 1.1\,\mathrm{mm\,mrad}$ and is conserved throughout acceleration (see Fig. 9.7 d1)). Furthermore, the slice emittance distributions equal for the beamlets and the full beam in this plane as shown in Fig. 9.7 c1). As opposed to the cropped case, re-arranging the trapping volume results in increased trace space volume. However, much smaller emittance values result from the zz' trace space as illustrated in Fig. 9.7 b2). Here, the full beam features $\varepsilon_{n,z,tot} \approx 0.6\,\mathrm{mm\,mrad}$, while the single beamlets yield $\varepsilon_{n,z,1} \approx 0.5\,\mathrm{mm\,mrad}$ and $\varepsilon_{n,z,2} \approx 0.4\,\mathrm{mm\,mrad}$. The asymmetry of the beamlets' emittance values is also reflected in the different distributions in Fig. 9.7 b2) (cf. red and blue distributions) caused by the asymmetric trapping volume and may originate from the irregular trapping filaments. The asymmetry of the bunchlets is further visible in the slice emittances $\varepsilon_{n,z}$ in Fig. 9.7 c2). Notwithstanding the above, this beam exhibits particularly

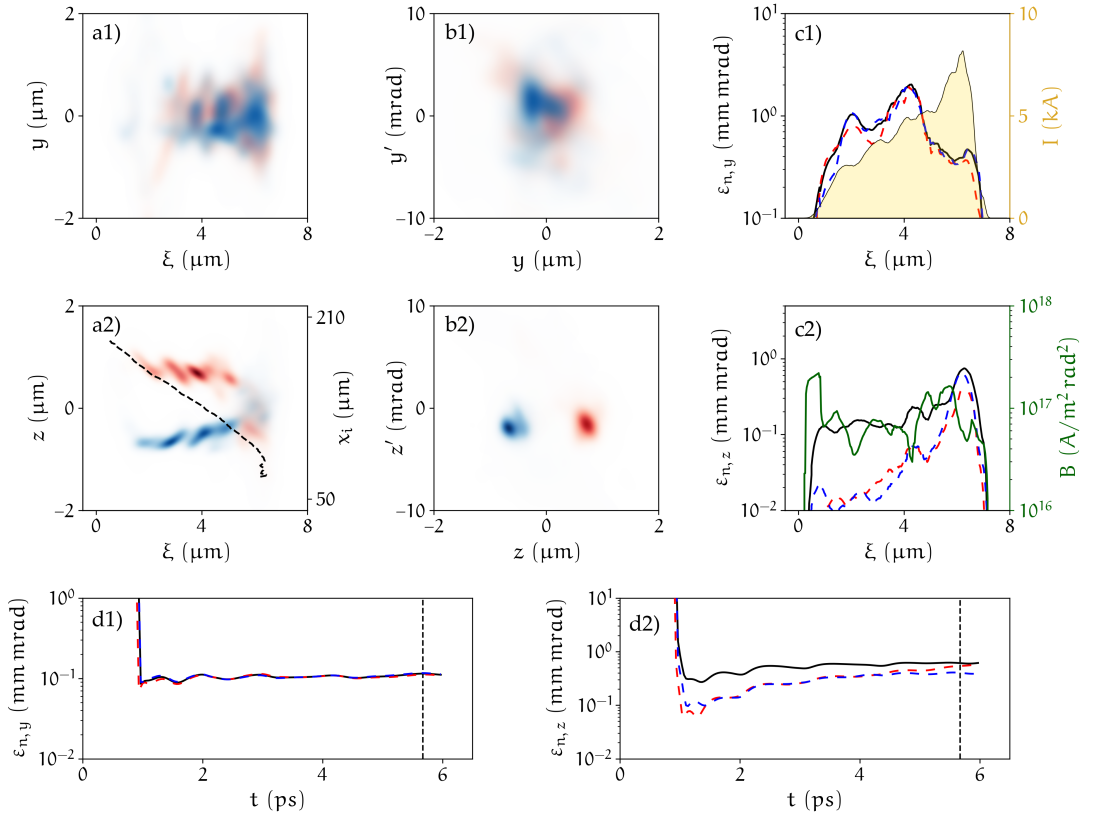

Figure 9.7: Properties of the electron beam generated by a wide plasma torch injector $r_{flat} = 40\,\mu m$, $l_{ramp} = 200\,\mu m$ and asymmetric drive beam with $\sigma_z = 1.5 \times \sigma_y$. In all panels, red and blue colours denote quantities for beamlets originating from $z > 0$ (upper beamlet) and $z < 0$ (lower beamlet), respectively. a), real space representation of the projected witness beam density. a2) further shows the mapping of the initial position x_i onto the final position within the formed electron distribution (black dashed line, right axis). b), projected transverse trace space density. c), slice properties of the beam. c1), slice emittance values of the full beam (black), upper beamlet (red) and lower beamlet (blue) and slice currents of the full beam (yellow shade, right axis). c2), slice emittance values as in c1) and brightness of the full beam (green, right axis). d), temporal emittance evolution of both planes for the full beam (black lines) and both beamlets (dashed lines with respective colours). The dashed lines indicate extraction points of a) to c). This figure is adapted from [175].

low-emittance slices with $\varepsilon_{n,z} < 50\,nm\,rad$ concomitant with slice brightness values of approximately $10^{17}\,A/m^2\,rad^2$. Each beamlet individually would further increase this value and therefore compete with state-of-the-art LINACS [163].

Based on the findings above, we can formulate some qualitative conditions for producing twin-beamlets with narrow plasma torch injectors. Firstly, the density downramp has to be sufficiently strong to trigger injection. Secondly, the transverse extent of the plasma torch must be smaller than the maximum wake radius $r_{flat} + l_{ramp} > r_b$ in order to confine the trapping volume to the desired plane. The planarity of the witness population can be controlled by the volumetric overlap between the wakefields and the plasma torch as indicated by the model Eq. (8.9). In case of twin-beamlets from adiabatic, wide plasma torches, the previous first criterion must still be met. The second requirement

regards the asymmetry of the blowout, which has to facilitate the re-distribution of the trapping volume. Here, smaller l_{ramp}require larger asymmetries. Determining more precise, quantitative conditions for producing twin-beamlets remains the subject of future investigations.

The scenarios illustrated in Fig. 9.6 and Fig. 9.7 both exhibit excellent properties for the generation of betatron radiation, which could produce bright x-rays [33]. In particular, the planar motion of the bunchlets is expected to result in radiation which is polarised parallel to their plane of oscillation similar to [46, 155]. Not only can the degree of polarisation of the beamlet oscillation be tuned, but the plane itself can also be rotated by rotating the orientation of the torch laser pulse. An asymmetry of the driver beam density profile can also, or additionally, be exploited to induce polarisation of the injected beamlet oscillation. The trapping volumes further reveal pathways towards higher degrees of polarisation, e.g. by further increasing the transverse cropping compared to the present cases in Fig. 9.5 a2), or by increasing the asymmetry of the drive beam in case of Fig. 9.5 b2).

Further theoretical, numerical and experimental work is required to study the counter-oscillating twin-beamlets. For instance, dedicated simulations need to address whether inter-beamlet effects compromise the integrity of the separate populations throughout longer acceleration. First experimental evidence of the beamlets may be obtained at the upcoming E-311 campaign at SLAC FACET II, which is dedicated to the plasma torch injector. Properties of the betatron radiation of the twin-beamlets can be obtained from an analysis of the trajectories from simulations [134, 150].

9.4 PLASMA TORCH DENSITY SCAN

The peak density $n_{T,0}$ (cf. Eq. (8.3)) of the plasma torch resembles another crucial property of the injector. It determines the density gradient of the plasma torch and hence controls the characteristics of injected electron formations. In experiments, $n_{T,0}$ can be varied by adapting the partial pressures of different gas components. This can result in a high degree of tunability similar to unlocking additional ionisation levels by varying the torch laser energy as observed in Fig. 8.6. As discussed in Section 6.4, this tunability generally arises from the decoupling of the torch from the medium that serves the wake excitation. Even in the current baseline case, where the plasma component for wake excitation (H^+, He^+) is coupled to the torch medium (He^{2+}) to avoid the production of dark current, the plasma torch peak density can be designed in a wide range. Denoting the gas densities of neutral hydrogen n_H and neutral helium n_{He}, the plasma channel density equals $n_{ch} = n_H + n_{He}$ and the peak density of the plasma torch is $n_{T,0} = n_{He}$. Consequently, $n_{T,0}/n_{ch} = 1 - n_H/n_{ch}$ such that the torch density can be varied from 0 to n_{ch} by changing the gas mix at constant plasma channel density.

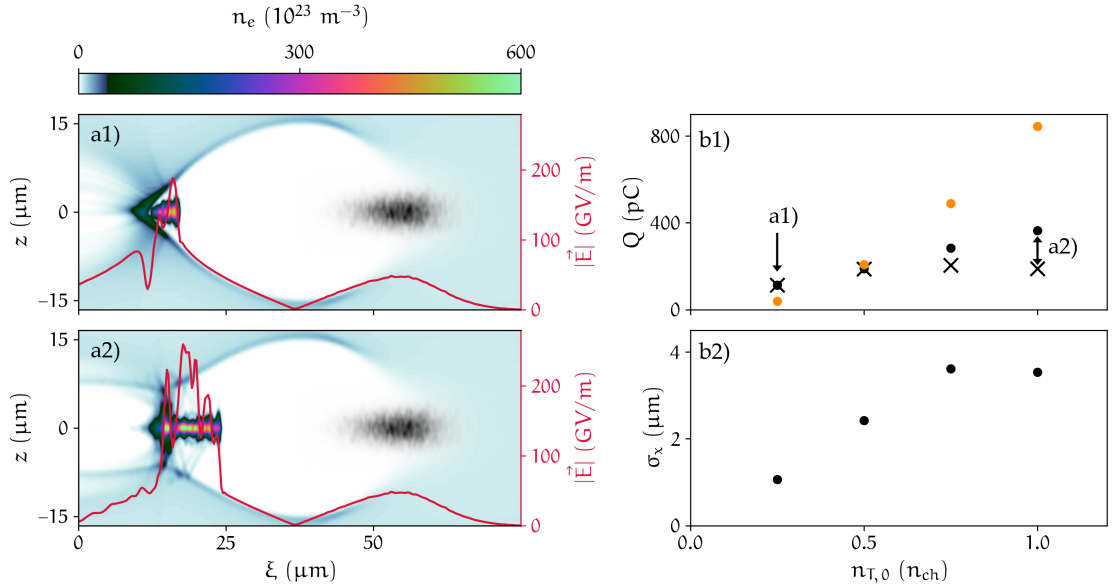

Figure 9.8: Injectors of varying peak density $n_{T,0}$. a), PWFA after injection for $n_{T,0} = 0.25 \times n_{ch}$ (a1) and $n_{T,0} = n_{ch}$ (a2). b1), injected witness charge Q as function of the plasma torch peak density $n_{T,0}$. Displayed are the total witness charge (black dots), the torch-generated charge component (black crosses) and results from the phenomenological trapping model (orange). b2), r.m.s. length σ_x of the full witness beam dependent on the peak density of the plasma torch $n_{T,0}$.

The influence of $n_{T,0}/n_{ch}$ is studied using the previous PIC setup with constant $n_{ch} = 6 \times 10^{23}$ m^{-3}, the drive beam parameters as in Table 9.1 and the torch parameters $r_{flat} = 2.5\,\mu m$ and $l_{ramp} = 40\,\mu m$. The PIC snapshots in Fig. 9.8 a1) and a2) display the two extreme cases with $n_{T,0} = 0.25 \times n_{ch}$ and $n_{T,0} = n_{ch}$ approximately 1.5 mm after injection. The first case produces a high-quality witness beam of $\varepsilon_{n,y} \approx \varepsilon_{n,y} \approx 0.8$ mm mrad and charge $Q \approx 113$ pC and moderate electron densities as visualised by the colour scale in Fig. 9.8 a). The resulting absolute values of the wakefield $|\vec{E}|$ remain below 200 GV/m. The high-density case, however, injects $Q \approx 189$ pC leading to much higher witness beam densities. The corresponding absolute values of the electric field exceed 200 GV/m at the rear of the blowout and therefore trigger tunnelling ionisation of additional He^{2+} electrons, which are then trapped into the first period of the wake and add to the torch-injected witness beam. Including the population from ionisation injection, the total beam features a charge as high as $Q \approx 364$ pC and normalised emittance values exceeding 5 mm mrad.

Large plasma torch densities therefore allow for an additional mode of injection, where the torch-generated population is superimposed by an "inception" beam [5] from ionisation injection. Figure 9.8 b1) summarises results of the full density scan for the torch-injected charge (black crosses) and the full witness charge including the "inception" beam (black dots). With the current set of parameters, pure torch injection occurs for $n_{T,0}/n_{ch} \leqslant 0.5$, whereas the increased witness charge from torch-injection with $n_{T,0}/n_{ch} > 0.5$ triggers additional beam generation from ionisation injection. Note,

that the charge from pure torch injection saturates for $n_{T,0}/n_{ch} \geqslant 0.75$ and therefore contrasts with other results for torch injection in PWFA [186] and hydrodynamic downramp injection in LWFA [50, 72], which predict approximately linear relationships. This can be explained by examining the simulation of $n_{T,0}/n_{ch} = 1$ in more detail. It reveals that the violent injection process leads to strong space charge forces that repel fractions of the witness beam, which then slip back into the second wake period such that witness charge is lost. Moreover, the charge saturation may indicate influences on the injection dynamics that originate from comparable driver beam density $n_{b,0} \approx 3.5 \times 10^{24}\ m^{-3}$ and peak plasma density $n_{T,0} + n_{ch} \approx 1.2 \times 10^{24}\ m^{-3}$, such that interactions approach the borderline of the underdense regime. The phenomenological model through Eq. (8.9) has been evaluated for the density scan and is illustrated as orange dots in Fig. 9.8 b1). Due to its scaling $Q_M \propto (1 - (1 + n_{T,0}/n_{ch})^{-1/2})^3$, the model exhibits large deviations for $n_{T,0}/n_{ch} \neq 0.5$, which may originate from different sources. First, increased peak densities $n_{T,0}/n_{ch} \approx 1$ may no longer be treated as perturbation. In the current case, such torch densities lead to the borderline case of underdense interactions, which additionally violates the assumption associated with the blowout regime. Second, the distribution function $\eta(n_T)$ was chosen based on physical arguments and other choices may be more accurate for a wider parameter range. Further theoretical investigations and a derivation from first principles are therefore required to include the density dependence of the model.

Figure 9.8 a1) and a2) further reveals typical downramp scalings that were indicated before in Fig. 8.6 and outlined in [171]: the length of the injected beam correlates to the densities as $\propto \lambda_p(n_{ch}) - \lambda_p(n_{ch} + n_{T,0})$, i.e. can be controlled via $n_{T,0}$. Although the "inception" beam complicates to disentangle the relationships for pure plasma torch injection in the current study, the torch component is injected prior to the "inception" beam and therefore defines the length of the full beam. The r.m.s. length σ_x of the full witness beam from the density scan is illustrated in Fig. 9.8 b2) and demonstrates that σ_x can be varied from approximately 1.1 µm to 3.6 µm in this density range and gives additional control over the generated electron beam.

The properties of the "inception" beam can in principle be controlled by varying the coupled helium density and propagation distance after the plasma torch. Production of this witness beam component after the torch-generated witness population implies that both occupy different energetic ranges, thus enabling the generation of multi-colour beams [177]. Moreover, both electron populations are inherently synchronised and ultra-short as shown in Fig. 9.8 b2) such that the generation of multi-colour x-rays [136, 182], or γ-rays [85] would be a possible application of such beam ensembles. This may fuel a variety of scientific disciplines that necessitate resolution of ultra-fast dynamics in pump-probe experiments, such as time resolved investigations of molecular dynamics [104, 110].

However, the "inception" beam exhibits a broadband spectrum due to the non-localised ionisation injection. This is undesired for demanding applications that require low energy spreads and further problematic for the beam transport, which commonly relies on chromatic components. The generation of the "inception" component further couples to the properties of the torch-injected beam, which limits their tunability and translates small fluctuations of the first injector into variations of the resulting beam ensemble in experiments. A more flexible and controllable means for generating multi-colour beams is therefore discussed in the next section.

9.5 BEAM ENSEMBLES FROM SUBSEQUENT PLASMA TORCH INJECTORS

Controlled and flexible generation of multi-colour beams can be achieved when producing beam ensembles from multiple subsequent plasma torch injectors. The localisation of the laser-generated plasma spikes additionally allows for seamless spacing of the injectors via different focus positions, which controls the energetic composition of these beams. Experimentally, the implementation of a second plasma torch injector in PWFA laboratories is straightforward due to the moderate laser properties that are required. It can be achieved by splitting the torch laser, or by introducing an independent laser which does not require demanding synchronisation (cf. discussion in Section 8.7). Furthermore, the density distribution of each plasma torch can be designed by the appropriate choice of laser parameters or focusing. Experiments with multiple injectors may particularly profit from the inherent stability and versatility as outlined in previous chapters.

The controlled and stable production of beam compositions may also find application in the acceleration of single high-quality electron beams in PWFAs. After injection, such beams accumulate a negative energy chirp due to the slope of the accelerating wakefield, which impairs the beam's quality. However, this chirp can be compensated by introducing a second, high-charge beam in addition to the witness beam [107]. The resulting, de-chirped electron beams feature ultra-high brightness suitable for next generation light sources such as FELs [71, 108].

To take advantage of the resilience with respect to experimental misalignments (see Section 8.9), the generation of high-charge beam ensembles is investigated based on the wide torch configurations with $r_{flat} > r_b$ discussed in Section 9.1. The ramp lengths l_{ramp} are chosen such that fully loading the wake is avoided based on the ramp scan in Fig. 9.1 ensuring that a second injection event can be achieved. The spatial separation of both injectors is set to approximately 2 mm, such that the high-energy component (denoted with the subset 1) exceeds the mean energy of 100 MeV before generation of the low-energy component (denoted with the subset 2) from the second plasma torch. In addition to the energetic spacing, the correlation of the r.m.s. length of generated witness beams in Fig. 9.1 b) and Fig. 9.8 b) is exploited to tune the longitudinal overlap of both populations.

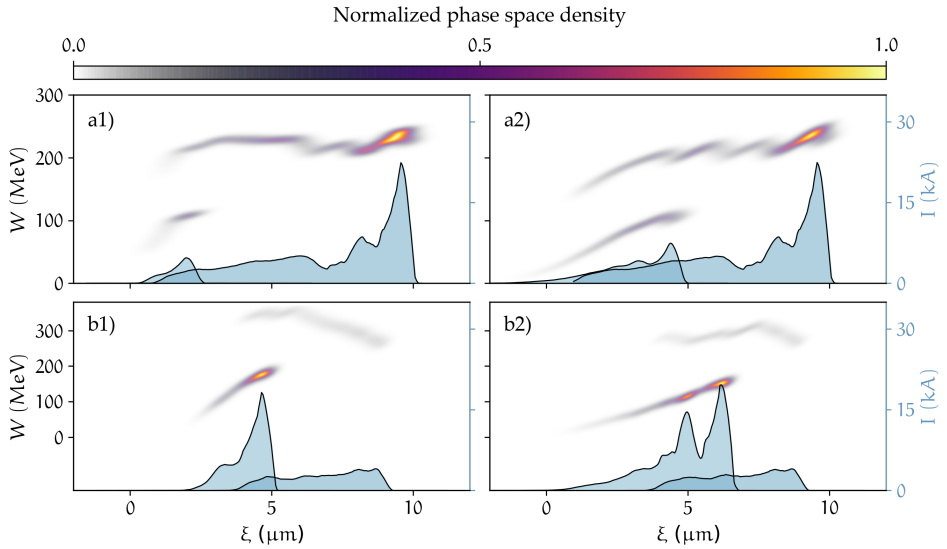

Figure 9.9: Beam ensembles from subsequent plasma torch injectors. Shown are resulting longitudinal phase space densities (left axis and colour map) and slice currents (coloured blue, right axes, 50 nm bin size) of beams from both plasma torches. Four combinations are studied. a), the first torch is comprised of $r_{flat,1} = 40\,\mu m$, $l_{ramp,1} = 80\,\mu m$ and the peak density $n_{T,1} = 0.5 \times n_{ch}$ followed by the second torch with $r_{flat,2} = 40\,\mu m$, $l_{ramp,2} = 10\,\mu m$ and $n_{T,2} = 0.3 \times n_{ch}$ (a1) and $n_{T,2} = 0.5 \times n_{ch}$ (a2). b), the first torch is formed of $r_{flat,1} = 40\,\mu m$, $l_{ramp,1} = 300\,\mu m$ and the peak density $n_{T,1} = 0.5 \times n_{ch}$ followed by the second torch with $r_{flat,2} = 40\,\mu m$, $l_{ramp,2} = 10\,\mu m$ and $n_{T,2} = 0.3 \times n_{ch}$ (b1) and $n_{T,2} = 0.5 \times n_{ch}$ (b2).

The first case shown in Fig. 9.9 a) examines the generation of a high-charge high-energy component by utilising $r_{flat,1} = 40\,\mu m$, $l_{ramp,1} = 80\,\mu m$ and the peak density $n_{T,1} = 0.5 \times n_{ch}$. The resulting electron beam contains approximately 160 pC charge distributed over $\sigma_x \approx 2.5\,\mu m$ sampled by more than 3.1×10^5 macro particles. It displays peak currents as large as 22.4 kA and gained approximately 100 MeV when approaching the second injector, which is formed of $r_{flat,2} = 40\,\mu m$, $l_{ramp,2} = 10\,\mu m$. Figure 9.9 a1) visualises the longitudinal phase space density and the slice current distribution of the resulting beam ensemble for $n_{T,2} = 0.3 \times n_{ch}$. Both components clearly occupy separate energy ranges as designed by the positioning of the second injector. The resulting low-energy component features $Q \approx 16\,pC$, $\sigma_x \approx 0.5\,\mu m$ (4.1×10^4 macro particles) and displays peak currents of approximately 4.7 kA. Figure 9.9 a2) shows the results for the same parameters as in a1), but with increased $n_{T,2} = 0.5 \times n_{ch}$. Consequently, the second component contains a larger charge $Q \approx 49\,pC$ (1.1×10^5 macro particles) and r.m.s. length $\sigma_x \approx 1.3\,\mu m$. This is further reflected by the increased peak current of 7.5 kA. Interestingly, the low-energy component in Fig. 9.9 a2) features only 20 % of the injected charge compared to the single torch injector with the same parameters (cf. Fig. 9.1). The presence of the high-energy component therefore reduces the efficacy of the second injector and hence indicates a dependency of the low-energy component's properties on the beam that is injected first.

The second case visualised in Fig. 9.9 b) employs a different set of injector parameters to obtain a low-charge high-energy component using $r_{flat,1} = 40\,\mu m$, $l_{ramp,1} = 300\,\mu m$ and the peak density $n_{T,1} = 0.5 \times n_{ch}$. This produces a high-energy component with $Q \approx 46\,pC$, $\sigma_x \approx 1.4\,\mu m$ sampled by more than 9.6×10^4 macro particles. The corresponding peak current amounts to approximately 4.0 kA. The subsequent injector is formed of $r_{flat,2} = 40\,\mu m$, $l_{ramp,2} = 10\,\mu m$. Figure 9.9 b1) illustrates the beam ensembles longitudinal phase space density for $n_{T,2} = 0.3 \times n_{ch}$ generating a low-energy component with 65 pC (1.6×10^5 macro particles) and $\sigma_x \approx 0.6\,\mu m$. In this injector configuration, the second electron population features high peak currents of approximately 18.2 kA. Results of the same setup, but with $n_{T,2} = 0.5 \times n_{ch}$ are visualised in Fig. 9.9 b2). Here, the low-energy component exhibits 119 pC (2.6×10^5 macro particles) and $\sigma_x \approx 1.3\,\mu m$. Again, the peak currents of the first beam surpass these of the second and amount to 19.6 kA.

Although the second plasma torch equals in the columns of Fig. 9.9, more charge is generated in b1) and b2), i.e. for smaller charges of the high-energy component. Once more, this emphasises the dependence of the second injector on the pre-loaded wake, which has to be considered for designing beam ensembles for experiments.

Thoroughly designing multiple beam populations thus requires the exploration of the first injector as well as the injection into the loaded wake, which resembles a multi-dimensional parameter space. PIC studies of this parameter space may be computationally costly, such that further expansion of the phenomenological model through Eq. (8.9) may be a powerful tool to identify optimum working points.

9.6 SUMMARY

This chapter systematically investigated various parameters of the plasma torch injector. The plasma torch principle allows to tune the shape, density gradient and the orientation of the produced plasma spike. The first case concerned plasma spikes much wider than the blowout, such that injection occurs approximately axially symmetric with respect to the driver orbit. It is found that this configuration can mimic the dynamics of typical downramp injectors. For instance, rapid injection was identified where electrons break transversally off the wake sheath, if the density gradient is shorter than the plasma period λ_p. In contrast to this regime, adiabatic injection was observed, which occurs for density ramps longer than λ_p. Here, electrons break approximately on-axis at the wake vertex. The concept of the trapping volume n_{trap}, which was introduced in the previous chapter in Section 8.8, was further employed to characterise the trapping process. It represents the witness beam's initial conditions and determines its evolution throughout the injection and acceleration process. In the case of wide plasma torches, the trapping volume assumes an annular shape that is characteristic for the injection via the maximum blowout radius of the plasma wave. These witness beams are of high quality and exhibit

slices of outstanding 5D brightness in excess of $10^{17}\,A/m^2rad^2$. However, adiabatically injected witness beams are sensitive to small variations of the wakefield, which may be a result of the fragile injection process that is characterised by filamented trapping volumina.

The second geometric extreme case comprised injectors that lead to asymmetric witness formations. Uniquely to plasma torch injectors, this can be achieved by reducing the plasma torch extent in one plane and produces a cropped version of the previously described annular trapping volume. Electrons are therefore injected predominantly in one plane via opposing wake sheaths leading to two beamlet populations that perform phase-shifted betatron oscillations. The separation of both formations is clearly visible in their trace space and is conserved throughout acceleration. A second method to generate such beamlets was studied by employing asymmetric blowouts in combination with wide and adiabatic plasma torch injectors. In this case, the beamlet structure arises most likely from re-distribution of the trapping volume due to enhanced wave breaking.

The trapping model derived in the previous chapter in Section 8.5 was further validated and resulted in good agreement with the geometric plasma torch scans for ramp lengths smaller than $200\,\mu m$. For $l_{ramp} > 200\,\mu m$, the model systematically overestimated injected charge values, which may be resolved by adapting the distribution function $\eta(n_T)$ to account for adiabatic injection. It reproduced trends comparing symmetric and asymmetric blowouts. The dependency on the plasma torch peak density $n_{T,0}$, however, was not recovered, which may be due to the breaking of the model's assumptions, or due to the choice of an unsuitable distribution function $\eta(n_T)$. Yet, the excellent agreement of the other scans shows potential for further theoretical and numerical development of this approach.

The localisation of the plasma torch injector further facilitates multiple, subsequent injection events, similar to recent demonstrations in LWFA [182]. The resulting beams may be employed for multi-colour radiation generation, or de-chirping schemes in PWFAs. First PIC simulations were conducted demonstrating the proof of concept and revealed that the beam from the first injector affects the properties of the second witness component. A promising path for further investigation with reduced computational costs may be to extend the phenomenological model introduced in Section 8.5 to include pre-loaded wakefield distributions. This would enable the efficient exploration of the large plasma torch parameter space.

Part IV

RÉSUMÉ

10

SUMMARY AND OUTLOOK

The plasma torch injector has been studied by extensive theoretical and numerical investigations. In contrast to hydrodynamic downramp schemes that re-distribute gas volumes and lead to global density variations, the plasma torch scheme relies on the superposition of an existing plasma component with a laser-generated density spike. This enables the controlled production of μm-length and highly localised density gradients. Both arise from the exponential behaviour of the underlying tunnelling ionisation rates in addition to the focusing of the injector laser, and promote electron trapping in PWFA. Almost 20 years after its inception [23, 166], the plasma torch approach has facilitated the first density downramp injection in beam-driven plasma wakefield experiments, achieved at SLAC FACET. This proof of concept experiment has been studied by PIC simulations in the current thesis, and elucidated experimental shortcomings causing the measurement of fluctuating witness beam properties.

The underlying plasma source sustaining the plasma wave has been identified as one major jitter source. The limited energy budget of the pre-ionisation laser and the additional constraint to avoid ionisation of helium by this means imposed the choice of the axilens setup resulting in a tapering bead chain formation of the plasma channel. The transverse extent of this channel limited the choice of the employed plasma density at the same time, as it had to fully facilitate the blowout. As a consequence, elevated plasma densities were required and caused unfavourable effects. First, the driver beam was mismatched to the plasma channel density resulting in strong beam evolution. Second, the varying plasma channel distribution induced unstable conditions for the plasma accelerator. Both promoted the generation of dark current and additionally destabilised the injector, which triggered fluctuating properties of the witness beam and non-uniform acceleration. The impact of a fluctuating channel generation at SLAC FACET produced up to 25 % of charge variation.

Future PWFA experiments, e.g. at SLAC FACET II, therefore demand for the stabilising properties of wide plasma sources. Such plasma channels could facilitate lower densities for wake excitation, concomitant with larger blowouts dimensions, which require for less challenging spatial alignment. Lower plasma densities further promote the driver beam matching. At the same time, blowouts could be excited by less dense driver beams, which is particularly advantageous for low-current electron beams, e.g. at FLASHForward [40]. However, producing wide and long plasma channels remains a complex topic in its own right, whereas recent progress in the design of various axicon-lens configurations [41, 68, 79], or heated expansion of plasma channels [120, 157] are encouraging.

The localisation of the plasma torch requires the stable alignment of the injector laser with respect to the propagation axis of the plasma wave. This caused charge fluctuations

of the order of 26 % in the experiments at SLAC FACET and was the second major source of jitter. Yet, this sensitivity can be readily eliminated by different approaches. Increased pointing stability may be obtained by advanced laser technology, or by utilising a separate, more stable mJ-class laser system. The latter takes advantage of the undemanding timing requirements of torch injection and may benefit from shorter laser beam transport. Another approach to mitigate pointing instabilities includes the production of plasma spikes that are much wider than the blowout. For instance, this can be achieved by large spot sizes for Gaussian focussing, or by employing cylindrical optics to generate wide plasma slabs.

Regardless of the adverse boundary conditions of the plasma torch experiments at SLAC FACET, the measured charge stability of 18 % exceeds the state-of-the-art shock front injection in LWFA of approximately 33 % [182], a process that has been optimised for over a decade. Implementing the proposed strategies for stabilisation, plasma torch injectors are anticipated to yield reliable, tunable and high-quality electron beams in future implementations.

One major outcome of the present thesis was the derivation of a phenomenological model for plasma torch injection. To the knowledge of the author, this description represents the first quantitative model of density downramp injection for plasma wakefield accelerators. The results agree with measurements and the PIC modelling of the experiments at SLAC FACET and further guided the exploration of the capabilities arising from the plasma torch method. The structure of the model predicts the control over trapped beams by manipulating the density distribution of the density spike n_T, which can in principle be achieved by the 4D shaping of n_T via the injector laser. Such shaping was studied in simulations for torch formations wider than the blowout and narrower than the blowout. Common density downramp dynamics were recovered for the former, including the well-known rapid and the adiabatic regime of particle trapping. The latter, however, exhibits a behaviour not yet observed in density downramp injectors. For instance, injected witness charge typically increases for shorter downramps [167] as confirmed in simulations and the derived trapping model. However, injected charge deviates from this scaling for narrow torch distributions, which originates from the cropping of the trapping volume n_{trap}, which characterises the initial conditions of the to-be-formed electron population and thus determines the trapping as well as the acceleration of the witness beam. Such n_{trap} result in particle trapping occurring predominantly in one plane via opposing wake sheaths. Similarly, this can be triggered by adiabatic torch injectors and asymmetric blowouts. In both cases, the witness beam is formed of two beamlets that perform phase-shifted betatron oscillations – an excellent prerequisite for controlled generation of polarised x-rays [33]. The control over the large-amplitude oscillations and the properties of the resultant radiation needs to be addressed in future theoretical and numerical investigations as well as in upcoming experiments at SLAC FACET II.

Some parametric dependencies of the plasma torch injector could not be recovered by the phenomenological model. For instance, systematic deviations were observed for the ultra-adiabatic regime of injection where $l_{ramp} \gg \lambda_p$, and the torch density scan led to large deviations compared to PIC results. This may be amended by implementing another distribution function $\eta(n_T)$ and requires new investigations. Further development of this model may additionally predict charges from multiple plasma torch injectors, or other witness beam properties, such as the beam length or the trapping volume n_{trap}.

The success of plasma torch injection in the E-210 campaign at SLAC FACET has led to approved experiments at international research facilities. In fact, Knetsch et al. have meanwhile demonstrated plasma torch injection for PWFAs driven by low-current electron beams at FLASHForward, DESY [92]. Other upcoming experiments include the E-311 campaign at SLAC FACET II with improved stability compared to its predecessor. It aims for studying the novel capabilities from 3D shaping of the plasma spike and increased densities for higher witness qualities as presented in this thesis.

Other plasma torch experiments are planned at LWFA facilities, e.g. at the Helmholtz-Zentrum Dresden-Rossendorf and the Centre for Advanced Laser Applications in Munich, which develop staged laser-to-particle-driven plasma wakefield accelerators known as L2PWFA [95, 115]. Here, the witness beam of a LWFA is coupled into a second target to drive a PWFA. The second stage may particularly benefit from the torch injector in case of low-current beams originating from the laser-driven accelerator and takes advantage of already available laser infrastructure. This would eliminate the need for large and highly expensive linacs and therefore paves the way towards a new era for the generation and application of high-quality electron beams in university-scale facilities.

BIBLIOGRAPHY

[1] A. Knetsch. "Acceleration of laser-injected electron beams in an electron-beam driven plasma wakefield accelerator." PhD thesis. Universität Hamburg, 2017. URL: http://bib-pubdb1.desy.de/record/401447/files/Dissertation.pdf.

[2] E. Adli et al. "Acceleration of electrons in the plasma wakefield of a proton bunch." In: Nature 561.7723 (2018), pp. 363–367. ISSN: 14764687. DOI: 10.1038/s41586-018-0485-4.

[3] A. Akhiezer et al. "Theory of Wave Motion of an Electron Plasma." In: Sov. Phys. JETP Vol: 3 (1956).

[4] M. V. Ammosov et al. "Tunnel Ionization Of Complex Atoms And Atomic Ions In Electromagnetic Field." In: High Intensity Laser Process. 0664.6 (1986), p. 138. ISSN: 1996756X. DOI: 10.1117/12.938695.

[5] L. D. Amorim et al. "Ionization injection of 'inception' beams in plasma wakefield accelerators." In: Plasma Phys. Control. Fusion 61.10 (2019). ISSN: 13616587. DOI: 10.1088/1361-6587/ab4005.

[6] S. G. Anderson et al. "Space-charge effects in high brightness electron beam emittance measurements." In: Phys. Rev. Spec. Top. - Accel. Beams 5.1 (2002), pp. 12–23. ISSN: 10984402. DOI: 10.1103/PhysRevSTAB.5.014201.

[7] P. Antici et al. "Laser-driven electron beamlines generated by coupling laser-plasma sources with conventional transport systems." In: J. Appl. Phys. 112.4 (2012). ISSN: 00218979. DOI: 10.1063/1.4740456.

[8] J. Bakos et al. "Light intensity dependence of the multiphoton ionization probability in the resonance case." In: Phys. Lett. A 41.2 (1972), pp. 163–164. ISSN: 03759601. DOI: 10.1016/0375-9601(72)91095-X.

[9] O. Barbalat. Applications of particle accelerators. Tech. rep. CERN, 1994.

[10] S. K. Barber et al. "Measured Emittance Dependence on the Injection Method in Laser Plasma Accelerators." In: Phys. Rev. Lett. 119.10 (2017), pp. 1–5. ISSN: 10797114. DOI: 10.1103/PhysRevLett.119.104801.

[11] D. Bauer. "Ejection energy of photoelectrons in strong-field ionization." In: Phys. Rev. A - At. Mol. Opt. Phys. 55.3 (1997), pp. 2180–2185. ISSN: 10941622. DOI: 10.1103/PhysRevA.55.2180.

[12] D. Bauer et al. "Exact field ionization rates in the barrier-suppression regime from numerical time-dependent Schrödinger-equation calculations." In: Phys. Rev. A - At. Mol. Opt. Phys. 59.1 (1999), pp. 569–577. ISSN: 10941622. DOI: 10.1103/PhysRevA.59.569.

[13] M. A. Biondi et al. "Measurements of Ambipolar Diffusion in Helium." In: Phys. Rev. 75 (11 1949), pp. 1700–1705. DOI: 10.1103/PhysRev.75.1700.

[14] I. Blumenfeld et al. "Energy doubling of 42 GeV electrons in a metre-scale plasma wakefield accelerator." In: Nature 445.7129 (2007), pp. 741–744. ISSN: 14764687. DOI: 10.1038/nature05538.

[15] P. Brijesh et al. "Tuning the electron energy by controlling the density perturbation position in laser plasma accelerators." In: Phys. Plasmas 19.6 (2012), pp. 1–7. ISSN: 1070664X. DOI: 10.1063/1.4725421.

[16] D. L. Bruhwiler et al. "Particle-in-cell simulations of tunneling ionization effects in plasma-based accelerators." In: Phys. Plasmas 10.5 II (2003), pp. 2022–2030. ISSN: 1070664X. DOI: 10.1063/1.1566027.

[17] E. Brunetti et al. "Low emittance, high brilliance relativistic electron beams from a laser-plasma accelerator." In: Phys. Rev. Lett. 105.21 (2010), p. 215007. ISSN: 00319007. DOI: 10.1103/PhysRevLett.105.215007.

[18] A. Buck. "Advanced characterization and control of laser wakefield acceleration." PhD thesis. LMU München, 2011, p. 144. URL: https://edoc.ub.uni-muenchen.de/13461/.

[19] A. Buck et al. "Shock-front injector for high-quality laser-plasma acceleration." In: Phys. Rev. Lett. 110.18 (2013), pp. 1–5. ISSN: 00319007. DOI: 10.1103/PhysRevLett.110.185006.

[20] S. V. Bulanov et al. "Two-dimensional regimes of self-focusing, wake field generation, and induced focusing of a short intense laser pulse in an underdense plasma." In: Phys. Rev. Lett. 74.5 (1995), pp. 710–713. ISSN: 00319007. DOI: 10.1103/PhysRevLett.74.710.

[21] S. V. Bulanov et al. "Transverse-wake wave breaking." In: Phys. Rev. Lett. 78.22 (1997), pp. 4205–4208. ISSN: 10797114. DOI: 10.1103/PhysRevLett.78.4205.

[22] S. V. Bulanov et al. "Electron bunch acceleration in the wake wave breaking regime." In: Plasma Phys. Reports 32.4 (2006), pp. 263–281. ISSN: 1063780X. DOI: 10.1134/S1063780X06040015.

[23] S. Bulanov et al. "Particle injection into the wave acceleration phase due to nonlinear wake wave breaking." In: Phys. Rev. E - Stat. Physics, Plasmas, Fluids, Relat. Interdiscip. Top. 58.5 (1998). ISSN: 1063651X. DOI: 10.1103/PhysRevE.58.R5257.

[24] N. H. Burnett et al. "Cold-plasma production for recombination extreme-ultraviolet lasers by optical-field-induced ionization." In: J. Opt. Soc. Am. B 6.6 (1989), p. 1195. ISSN: 0740-3224. DOI: 10.1364/josab.6.001195.

[25] M. Burza et al. "Laser wakefield acceleration using wire produced double density ramps." In: Phys. Rev. Spec. Top. - Accel. Beams 16.1 (2013), pp. 3–7. ISSN: 10984402. DOI: 10.1103/PhysRevSTAB.16.011301.

[26] CMS Collaboration. "Observation of an Excess of Events in the Search for the Standard Model Higgs boson with the ATLAS detector at the LHC." In: Cms-Pas-Hig-12-020 716.1 (2012), pp. 1–29. URL: http://cds.cern.ch/record/1460439.

[27] F. F. Chen. Introduction to plasma physics and controlled fusion. Vol. 1. Springer, 1984. DOI: 10.1007/978-3-319-22309-4.

[28] M. Chen et al. "Numerical modeling of laser tunneling ionization in explicit particle-in-cell codes." In: J. Comput. Phys. 236.1 (2013), pp. 220–228. ISSN: 10902716. DOI: 10.1016/j.jcp.2012.11.029.

[29] P. Chen et al. "Energy transfer in the plasma wake-field accelerator." In: Phys. Rev. Lett. 56.12 (1986), pp. 1252–1255. ISSN: 00319007. DOI: 10.1103/PhysRevLett.56.1252.

[30] T. Y. Chien et al. "Spatially localized self-injection of electrons in a self-modulated laser-wakefield accelerator by using a laser-induced transient density ramp." In: Phys. Rev. Lett. 94.11 (2005), pp. 1–4. ISSN: 00319007. DOI: 10.1103/PhysRevLett.94.115003.

[31] T. R. Clark et al. "Time- and space-resolved density evolution of the plasma waveguide." In: Phys. Rev. Lett. 78.12 (1997), pp. 2373–2376. ISSN: 10797114. DOI: 10.1103/PhysRevLett.78.2373.

[32] T. P. Coffey. "Breaking of large amplitude plasma oscillations." In: Phys. Fluids 14.7 (1971), pp. 1402–1406. ISSN: 10706631. DOI: 10.1063/1.1693620.

[33] S. Corde et al. "Femtosecond x rays from laser-plasma accelerators." In: Rev. Mod. Phys. 85.1 (2013). ISSN: 00346861. DOI: 10.1103/RevModPhys.85.1.

[34] S. Corde et al. "Observation of longitudinal and transverse self-injections in laser-plasma accelerators." In: Nat. Commun. 4.1 (2013), pp. 1–7. ISSN: 20411723. DOI: 10.1038/ncomms2528.

[35] S. Corde et al. "Multi-gigaelectronvolt acceleration of positrons in a self-loaded plasma wakefield." In: Nature 524.7566 (2015), pp. 442–445. ISSN: 14764687. DOI: 10.1038/nature14890.

[36] P. B. Corkum et al. "Above-threshold ionization in the long-wavelength limit." In: Phys. Rev. Lett. 62.11 (1989), pp. 1259–1262. ISSN: 00319007. DOI: 10.1103/PhysRevLett.62.1259.

[37] Tech-X Corporation. VSim User Guide. Version Release 10.1.0-r2780. URL: https://txcorp.com/images/docs/vsim/latest/VSimUserGuide.pdf.

[38] B. M. Cowan et al. "Characteristics of an envelope model for laser-plasma accelerator simulation." In: J. Comput. Phys. 230.1 (2011), pp. 61–86. ISSN: 10902716. DOI: 10.1016/j.jcp.2010.09.009.

[39] B. M. Cowan et al. "Generalized algorithm for control of numerical dispersion in explicit time-domain electromagnetic simulations." In: Phys. Rev. ST Accel. Beams 16 (4 2013), p. 041303. DOI: 10.1103/PhysRevSTAB.16.041303.

[40] R. D'Arcy et al. "FLASHForward: Plasma wakefield accelerator science for high-average-power applications." In: Philos. Trans. R. Soc. A Math. Phys. Eng. Sci. 377.2151 (2019), pp. 0–2. ISSN: 1364503X. DOI: 10.1098/rsta.2018.0392.

[41] N. Davidson et al. "Holographic axilens: high resolution and long focal depth." In: Opt. Lett. 16.7 (1991), p. 523. ISSN: 0146-9592. DOI: 10.1364/ol.16.000523.

[42] J. M. Dawson. "Nonlinear electron oscillations in a cold plasma." In: Phys. Rev. 113.2 (1959), pp. 383–387. ISSN: 0031899X. DOI: 10.1103/PhysRev.113.383.

[43] N. B. Delone et al. "Tunneling and barrier-supression ionization of atoms and ions in a laser radiation field." In: Uspekhi Fiz. Nauk 168.5 (1998), pp. 548–549. ISSN: 00421294. DOI: 10.3367/ufnr.0168.199805c.0531.

[44] A. Deng et al. "Generation and acceleration of electron bunches from a plasma photocathode." In: Nat. Phys. 15.11 (2019), pp. 1156–1160. ISSN: 17452481. DOI: 10.1038/s41567-019-0610-9.

[45] J. C. Diels et al. Ultrashort Laser Pulse Phenomena. Elsevier, 2006. ISBN: 9780122154935. DOI: 10.1016/B978-0-12-215493-5.X5000-9.

[46] A. Döpp et al. "Stable femtosecond X-rays with tunable polarization from a laser-driven accelerator." In: Light Sci. Appl. 6.11 (2017), e17086–e17086. ISSN: 2047-7538. DOI: 10.1038/lsa.2017.86.

[47] C. G. Durfee et al. "Light pipe for high intensity laser pulses." In: Phys. Rev. Lett. 71.15 (1993), pp. 2409–2412. ISSN: 00319007. DOI: 10.1103/PhysRevLett.71.2409.

[48] A. Einstein. "On a Heuristic Point of View about the Creation and Conversion of Light." In: Old Quantum Theory 17.6 (1967), pp. 91–107. DOI: 10.1016/b978-0-08-012102-4.50014-0.

[49] H. Ekerfelt. "Numerical and Experimental Studies of Wakefield Accelerators." PhD thesis. Lund University, 2019.

[50] H. Ekerfelt et al. "A tunable electron beam source using trapping of electrons in a density down-ramp in laser wakefield acceleration." In: Sci. Rep. 7.1 (2017), pp. 1–9. ISSN: 20452322. DOI: 10.1038/s41598-017-12560-8.

[51] P. Emma et al. "First lasing and operation of an ångstrom-wavelength free-electron laser." In: Nat. Photonics 4.9 (2010), pp. 641–647. ISSN: 17494885. DOI: 10.1038/nphoton.2010.176.

[52] R. J. England et al. "Plasma electron fluid motion and wave breaking near a density transition." In: Phys. Rev. E - Stat. Physics, Plasmas, Fluids, Relat. Interdiscip. Top. 66.1 (2002), pp. 1–8. ISSN: 1063651X. DOI: 10.1103/PhysRevE.66.016501.

[53] L. Fan-Chiang et al. "Gas density structure of supersonic flows impinged on by thin blades for laser-plasma accelerator targets." In: Phys. Fluids 32.6 (2020), p. 66108. ISSN: 10897666. DOI: 10.1063/5.0005888.

[54] J. Faure et al. "Injection and acceleration of quasimonoenergetic relativistic electron beams using density gradients at the edges of a plasma channel." In: Phys. Plasmas 17.8 (2010). ISSN: 1070664X. DOI: 10.1063/1.3469581.

[55] T. Feder. "Accelerator school travels university circuit." In: Phys. Today 63.2 (2010), pp. 20–22. ISSN: 0031-9228. DOI: 10.1063/1.3326981.

[56] H. Fehske et al. Computational many-particle physics. Vol. 739. Springer, 2007. DOI: 10.1007/978-3-540-74686-7.

[57] M. Ferrario et al. "Space charge effects." In: Proc. CAS-CERN Accel. Sch. Adv. Accel. Phys. 009.August 2013 (2013), pp. 331–356. DOI: 10.5170/CERN-2014-009.331.

[58] K. Floettmann. "Some basic features of the beam emittance." In: Phys. Rev. Spec. Top. - Accel. Beams 6.3 (2003), pp. 80–86. ISSN: 10984402. DOI: 10.1103/PhysRevSTAB.6.034202.

[59] C. G. R. Geddes et al. "Plasma-density-gradient injection of low absolute-momentum-spread electron bunches." In: Phys. Rev. Lett. 100.21 (2008), pp. 1–4. ISSN: 00319007. DOI: 10.1103/PhysRevLett.100.215004.

[60] P. Gibbon. Short pulse laser interactions with matter: An introduction. Imperial College Press, 2005, pp. 1–312. ISBN: 9781860949340. DOI: 10.1142/P116.

[61] V. M. Gkortsas et al. "Interplay of mulitphoton and tunneling ionization in short-wavelength- driven high-order harmonic generation." In: Phys. Rev. A - At. Mol. Opt. Phys. 84.1 (2011), pp. 1–6. ISSN: 10502947. DOI: 10.1103/PhysRevA.84.013427.

[62] B. B. Godfrey. "Numerical Cherenkov instabilities in electromagnetic particle codes." In: J. Comput. Phys. 15.4 (1974), pp. 504–521. ISSN: 10902716. DOI: 10.1016/0021-9991(74)90076-X.

[63] A. A. Golovanov et al. "Generalised model of a sheath of a plasma bubble excited by a short laser pulse or by a relativistic electron bunch in transversely inhomogeneous plasma." In: Quantum Electron. 46.4 (2016), pp. 295–298. ISSN: 1063-7818. DOI: 10.1070/qel16040.

[64] A. J. Gonsalves et al. "Tunable laser plasma accelerator based on longitudinal density tailoring." In: Nat. Phys. 7.11 (2011), pp. 862–866. ISSN: 17452473. DOI: 10.1038/nphys2071.

[65] L. M. Gorbunov et al. "Excitation of plasma waves by an electromagnetic wave packet." In: Sov. Phys. JETP 66.2 (1987), pp. 290–294.

[66] S. Gordienko et al. "Scalings for ultrarelativistic laser plasmas and quasimonoenergetic electrons." In: Phys. Plasmas 12.4 (2005), pp. 1–11. ISSN: 1070664X. DOI: 10.1063/1.1884126.

[67] J. Grebenyuk et al. "Beam-driven plasma-based acceleration of electrons with density down-ramp injection at FLASHForward." In: Nucl. Instruments Methods Phys. Res. Sect. A Accel. Spectrometers, Detect. Assoc. Equip. 740 (2014), pp. 246–249. ISSN: 01689002. DOI: 10.1016/j.nima.2013.10.054.

[68] S. Z. Green et al. "Laser ionized preformed plasma at FACET." In: Plasma Phys. Control. Fusion 56.8 (2014). ISSN: 13616587. DOI: 10.1088/0741-3335/56/8/084011.

[69] A. D. Greenwood et al. "On the elimination of numerical Cerenkov radiation in PIC simulations." In: J. Comput. Phys. 201.2 (2004), pp. 665–684. ISSN: 00219991. DOI: 10.1016/j.jcp.2004.06.021.

[70] A. Grudiev et al. "A new local field quantity describing the high gradient limit of accelerating structures." In: Proc. 24th Linear Accel. Conf. LINAC 2008 12.10 (2009), pp. 936–938. ISSN: 1098-4402. DOI: 10.1103/physrevstab.12.102001.

[71] A. F. Habib et al. "Plasma accelerator-based ultrabright x-ray beams from ultrabright electron beams." In: 44.141 (2019), p. 9. ISSN: 1996-756X. DOI: 10.1117/12.2530976.

[72] M. Hansson et al. "Down-ramp injection and independently controlled acceleration of electrons in a tailored laser wakefield accelerator." In: Phys. Rev. Spec. Top. - Accel. Beams 18.7 (2015), pp. 1–7. ISSN: 10984402. DOI: 10.1103/PhysRevSTAB.18.071303.

[73] E. F. Haussecker et al. "The influence of accelerator science on physics research." In: Phys. Perspect. 13.2 (2011), pp. 146–160. ISSN: 14226944. DOI: 10.1007/s00016-010-0049-y.

[74] B. Hidding et al. "Ultracold electron bunch generation via plasma photocathode emission and acceleration in a beam-driven plasma blowout." In: Phys. Rev. Lett. 108.3 (2012), pp. 1–5. ISSN: 00319007. DOI: 10.1103/PhysRevLett.108.035001.

[75] B. Hidding et al. "Ultrahigh brightness bunches from hybrid plasma accelerators as drivers of 5th generation light sources." In: J. Phys. B At. Mol. Opt. Phys. 47.23 (2014). ISSN: 13616455. DOI: 10.1088/0953-4075/47/23/234010.

[76] B. Hidding et al. "Fundamentals and applications of hybrid LWFA-PWFA." In: Appl. Sci. 9.13 (2019). ISSN: 20763417. DOI: 10.3390/app9132626.

[77] I.I. Hirschman et al. The Convolution Transform. Dover Books on Mathematics. Dover Publications, 2012. ISBN: 9780486154565.

[78] M. J. Hogan et al. "Plasma wakefield acceleration experiments at FACET." In: New J. Phys. 12 (2010). ISSN: 13672630. DOI: 10.1088/1367-2630/12/5/055030.

[79] M. Honkanen et al. "Tandem systems for efficient generation of uniform-axial-intensity Bessel fields." In: Opt. Commun. 154.5-6 (1998), pp. 368–375. ISSN: 00304018. DOI: 10.1016/S0030-4018(98)00288-0.

[80] S. Humphries et al. Principles of Charged Particle Acceleration. Vol. 41. 5. Courier Corporation, 1988, pp. 98–99. DOI: 10.1063/1.2811424.

[81] J. Hyman. "Free expansion of an isolated plasma column." In: J. Appl. Phys. 39.10 (1968), pp. 4568–4573. ISSN: 00218979. DOI: 10.1063/1.1655802.

[82] J. D. Jackson. Classical electrodynamics. 3rd ed.. New York: Wiley, 1999. ISBN: 047130932X.

[83] C. Joshi et al. "High energy density plasma science with an ultrarelativistic electron beam." In: Phys. Plasmas 9.5 (2002), pp. 1845–1855. ISSN: 1070664X. DOI: 10.1063/1.1455003.

[84] E. Kallos et al. "High-gradient plasma-wakefield acceleration with two subpicosecond electron bunches." In: Phys. Rev. Lett. 100.7 (2008), p. 74802. ISSN: 00319007. DOI: 10.1103/PhysRevLett.100.074802.

[85] S. Y. Kalmykov et al. "Multi-color γ-rays from comb-like electron beams driven by incoherent stacks of laser pulses." In: AIP Conf. Proc. 1812.March (2017). ISSN: 15517616. DOI: 10.1063/1.4975899.

[86] S. Kalmykov et al. "Electron self-injection and trapping into an evolving plasma bubble." In: Phys. Rev. Lett. 103.13 (2009), pp. 1–4. ISSN: 00319007. DOI: 10.1103/PhysRevLett.103.135004.

[87] O. S. Karger. "Pathways towards Ultra-high brightness electron beams." PhD thesis. Universität Hamburg, 2020.

[88] T. Katsouleas. "Physical mechanisms in the plasma wake-field accelerator." In: Phys. Rev. A 33.3 (1986), pp. 2056–2064. ISSN: 10502947. DOI: 10.1103/PhysRevA.33.2056.

[89] T. Katsouleas et al. "Wave-breaking amplitude of relativistic oscillations in a thermal plasma." In: Phys. Rev. Lett. 61.1 (1988), pp. 90–93. ISSN: 00319007. DOI: 10.1103/PhysRevLett.61.90.

[90] L. V. Keldysh. "Ionization in the field of a strong electromagnetic wave." In: Sov. Phys. JETP 20.5 (1965), pp. 1307–1314.

[91] N. A. Kirby. "Properties of Trapped Electron Bunches in a Plasma Wakefield Accelerator." PhD thesis. Queensland University of Technology, 2009.

[92] A. Knetsch et al. "Controlled density-Downramp injection in a beam-driven plasma wakefield accelerator." In: arXiv (2020), pp. 1–11. arXiv: 2007.12639.

[93] I. Kostyukov et al. "Phenomenological theory of laser-plasma interaction in "bubble" regime." In: Phys. Plasmas 11.11 (2004), pp. 5256–5264. ISSN: 1070664X. DOI: 10.1063/1.1799371.

[94] I. Kostyukov et al. "Electron self-Injection in multidimensional relativistic-plasma wake fields." In: Phys. Rev. Lett. 103.17 (2009), pp. 1–4. ISSN: 00319007. DOI: 10.1103/PhysRevLett.103.175003.

[95] T. Kurz et al. Demonstration of a compact plasma accelerator powered by laser-accelerated electron beams. 2019. arXiv: 1909.06676 [physics.acc-ph].

[96] R. Lehe et al. "Numerical growth of emittance in simulations of laser-wakefield acceleration." In: Phys. Rev. Spec. Top. - Accel. Beams 16.2 (2013), pp. 1–8. ISSN: 10984402. DOI: 10.1103/PhysRevSTAB.16.021301.

[97] N. Lemos et al. "Effects of laser polarization in the expansion of plasma waveguides." In: Phys. Plasmas 20.10 (2013), p. 103109. ISSN: 1070664X. DOI: 10.1063/1.4825228.

[98] N. Lemos et al. "Plasma expansion into a waveguide created by a linearly polarized femtosecond laser pulse." In: Phys. Plasmas 20.6 (2013). ISSN: 1070664X. DOI: 10.1063/1.4810797.

[99] M. Litos et al. "High-efficiency acceleration of an electron beam in a plasma wakefield accelerator." In: Nature 515.7525 (2014), pp. 92–95. ISSN: 14764687. DOI: 10.1038/nature13882.

[100] K. V. Lotov. "Blowout regimes of plasma wakefield acceleration." In: Phys. Rev. E - Stat. Physics, Plasmas, Fluids, Relat. Interdiscip. Top. 69.4 (2004), p. 13. ISSN: 1063651X. DOI: 10.1103/PhysRevE.69.046405.

[101] W. Lu. "Nonlinear Plasma Wakefield Theory and Optimum Scaling for Laser Wakefield Accelerator (LWFA) in the Blowout Regime." PhD thesis. University of California, Los Angeles, 2006.

[102] W. Lu et al. "Nonlinear theory for relativistic plasma wakefields in the blowout regime." In: Phys. Rev. Lett. 96.16 (2006), p. 165002. ISSN: 00319007. DOI: 10.1103/PhysRevLett.96.165002.

[103] W. Lu et al. "Generating multi-GeV electron bunches using single stage laser wakefield acceleration in a 3D nonlinear regime." In: Phys. Rev. Spec. Top. - Accel. Beams 10.6 (2007), p. 61301. ISSN: 10984402. DOI: 10.1103/PhysRevSTAB.10.061301.

[104] A. A. Lutman et al. "Experimental demonstration of femtosecond two-color X-ray free-electron lasers." In: Phys. Rev. Lett. 110.13 (2013), p. 134801. ISSN: 00319007. DOI: 10.1103/PhysRevLett.110.134801.

[105] P. Maine et al. "Generation of Ultrahigh Peak Power Pulses by Chirped Pulse Amplification." In: IEEE J. Quantum Electron. 24.2 (1988), pp. 398–403. ISSN: 15581713. DOI: 10.1109/3.137.

[106] G. G. Manahan et al. "Hot spots and dark current in advanced plasma wakefield accelerators." In: Phys. Rev. Accel. Beams 19.1 (2016), pp. 1–9. ISSN: 24699888. DOI: 10.1103/PhysRevAccelBeams.19.011303.

[107] G. G. Manahan et al. "Single-stage plasma-based correlated energy spread compensation for ultrahigh 6D brightness electron beams." In: Nat. Commun. 8 (2017), pp. 1–9. ISSN: 20411723. DOI: 10.1038/ncomms15705.

[108] G. G. Manahan et al. "Advanced schemes for underdense plasma photocathode wakefield accelerators: Pathways towards ultrahigh brightness electron beams." In: Philos. Trans. R. Soc. A Math. Phys. Eng. Sci. 377.2151 (2019), p. 20180182. ISSN: 1364503X. DOI: 10.1098/rsta.2018.0182.

[109] S. P. D. Mangles et al. "Laser-wakefield acceleration of monoenergetic electron beams in the first plasma-wave period." In: Phys. Rev. Lett. 96.21 (2006), p. 215001. ISSN: 00319007. DOI: 10.1103/PhysRevLett.96.215001.

[110] A. Marinelli et al. "High-intensity double-pulse X-ray free-electron laser." In: Nat. Commun. 6 (2015), pp. 1–6. ISSN: 20411723. DOI: 10.1038/ncomms7369.

[111] K. A. Marsh et al. "Beam matching to a plasma wake field accelerator using a ramped density profile at the plasma boundary." In: Proc. IEEE Part. Accel. Conf. 2005 (2005), pp. 2702–2704. DOI: 10.1109/PAC.2005.1591234.

[112] A. Martinez De La Ossa et al. "High-quality electron beams from beam-driven plasma accelerators by wakefield-induced ionization injection." In: Phys. Rev. Lett. 111.24 (2013), p. 245003. ISSN: 00319007. DOI: 10.1103/PhysRevLett.111.245003.

[113] A. Martinez De La Ossa et al. "Wakefield-induced ionization injection in beam-driven plasma accelerators." In: Phys. Plasmas 22.9 (2015), p. 93107. ISSN: 10897674. DOI: 10.1063/1.4929921.

[114] A. Martinez De La Ossa et al. "Optimizing density down-ramp injection for beam-driven plasma wakefield accelerators." In: Phys. Rev. Accel. Beams 20.9 (2017), p. 91301. ISSN: 24699888. DOI: 10.1103/PhysRevAccelBeams.20.091301.

[115] A. Martinez De La Ossa et al. "Hybrid LWFA PWFA staging as a beam energy and brightness transformer: conceptual design and simulations." In: Philosophical Transactions of the Royal Society A: Mathematical, Physical and Engineering Sciences 377.2151 (2019), p. 20180175. DOI: 10.1098/rsta.2018.0175.

[116] A. E. Martirosyan et al. "Time evolution of plasma afterglow produced by femtosecond laser pulses." In: J. Appl. Phys. 96.10 (2004), pp. 5450–5455. ISSN: 00218979. DOI: 10.1063/1.1803920.

[117] F. Massimo et al. "Numerical study of laser energy effects on density transition injection in laser wakefield acceleration." In: Plasma Phys. Control. Fusion 60.3 (2018), p. 85004. ISSN: 13616587. DOI: 10.1088/1361-6587/aaa336.

[118] T. J. Mehrling. "Theoretical and Numerical Studies on the Transport of Transverse Beam Quality in Plasma-Based Accelerators." PhD thesis. Universität Hamburg, 2014, p. 221.

[119] T. J Mehrling et al. "Mitigation of the Hose Instability in Plasma-Wakefield Accelerators." In: Phys. Rev. Lett. 118.17 (2017), pp. 174801–174801. ISSN: 0031-9007. DOI: 10.1103/PhysRevLett.118.174801.

[120] B. Miao et al. "Optical Guiding in Meter-Scale Plasma Waveguides." In: Phys. Rev. Lett. 125.7 (2020), p. 74801. ISSN: 10797114. DOI: 10.1103/PhysRevLett.125.074801.

[121] M. Mitsumori et al. "Initial clinical results of linac-based stereotactic radiosurgery and stereotactic radiotherapy for pituitary adenomas." In: Int. J. Radiat. Oncol. Biol. Phys. 42.3 (1998), pp. 573–580. ISSN: 03603016. DOI: 10.1016/S0360-3016(98)00256-9.

[122] P. Mora et al. "Kinetic modeling of intense, short laser pulses propagating in tenuous plasmas." In: Phys. Plasmas 4.1 (1997), pp. 217–229. ISSN: 1070664X. DOI: 10.1063/1.872134.

[123] W. B. Mori et al. "Wavebreaking of longitudinal plasma oscillations." In: Phys. Scr. 1990.T30 (1990), pp. 127–133. ISSN: 14024896. DOI: 10.1088/0031-8949/1990/T30/018.

[124] P. Mulser et al. High Power Laser-Matter Interaction. Springer Tracts in Modern Physics. Springer Berlin Heidelberg, 2010. ISBN: 9783540460657. DOI: 10.1007/978-3-540-46065-7_1.

[125] U. Niedermayer et al. "Beam dynamics analysis of dielectric laser acceleration using a fast 6D tracking scheme." In: Phys. Rev. Accel. Beams 20.11 (2017), pp. 1–15. ISSN: 24699888. DOI: 10.1103/PhysRevAccelBeams.20.111302.

[126] C. Nieter et al. "VORPAL: A versatile plasma simulation code." In: J. Comput. Phys. 196.2 (2004), pp. 448–473. ISSN: 00219991. DOI: 10.1016/j.jcp.2003.11.004.

[127] A. Nikishov et al. "Ionization of Systems Bound by Short-range Forces by the Field of an Electromagnetic Wave." In: Sov. J. Exp. Theor. Phys. 23.1 (1966), p. 168. ISSN: 1063-7761.

[128] A. Nikishov et al. "Ionization of Atoms by an Electromagnetic-Wave Field." In: Sov. J. Exp. Theor. Phys. 25.1 (1967), p. 145. ISSN: 1063-7761.

[129] E. Oz et al. "Ionization-induced electron trapping in ultrarelativistic plasma wakes." In: Phys. Rev. Lett. 98.8 (2007), pp. 1–4. ISSN: 00319007. DOI: 10.1103/PhysRevLett.98.084801.

[130] A. Pak et al. "Injection and trapping of tunnel-ionized electrons into laser-produced wakes." In: Phys. Rev. Lett. 104.2 (2010), pp. 1–4. ISSN: 00319007. DOI: 10.1103/PhysRevLett.104.025003.

[131] W. K. H. Panofsky et al. "Some considerations concerning the transverse deflection of charged particles in radio-frequency fields." In: Rev. Sci. Instrum. 27.11 (1956), p. 967. ISSN: 00346748. DOI: 10.1063/1.1715427.

[132] E. Parzen. "On Estimation of a Probability Density Function and Mode." In: Ann. Math. Stat. 33.3 (1962), pp. 1065–1076. ISSN: 0003-4851. DOI: 10.1214/aoms/1177704472.

[133] S. Paul et al. "Rapid measurement of charged particle beam profiles using a current flux grating." In: Rev. Sci. Instrum. 86.2 (2015). ISSN: 10897623. DOI: 10.1063/1.4907346.

[134] R. Pausch et al. "Quantitatively consistent computation of coherent and incoherent radiation in particle-in-cell codes—A general form factor formalism for macro-particles." In: Nucl. Instruments Methods Phys. Res. Sect. A Accel. Spectrometers, Detect. Assoc. Equip. 909 (2018), pp. 419–422. ISSN: 01689002. DOI: 10.1016/j.nima.2018.02.020.

[135] A. Perelomov et al. "Ionization of Atoms in an Alternating Electric Field." In: Sov. J. Exp. Theor. Phys. 23.2 (1966), p. 924. ISSN: 1063-7761.

[136] V. Petrillo et al. "Dual color x rays from Thomson or Compton sources." In: Phys. Rev. Spec. Top. - Accel. Beams 17.2 (2014), p. 20706. ISSN: 10984402. DOI: 10.1103/PhysRevSTAB.17.020706.

[137] G. R. Plateau et al. "Low-emittance electron bunches from a laser-plasma accelerator measured using single-shot x-ray spectroscopy." In: Phys. Rev. Lett. 109.6 (2012), p. 064802. DOI: 10.1103/PhysRevLett.109.064802.

[138] V. S. Popov. "Tunnel and multiphoton ionization of atoms and ions in a strong laser field (Keldysh theory)." In: Physics-Uspekhi 47.9 (2004), pp. 855–885. ISSN: 1063-7869. DOI: 10.1070/pu2004v047n09abeh001812.

[139] A. Pukhov. "Particle-in-cell codes for plasma-based particle acceleration." In: CAS-CERN Accel. Sch. Plasma Wake Accel. 2014, Proc. (2014), pp. 181–206. DOI: 10.5170/CERN-2016-001.181.

[140] A. Pukhov et al. "Laser wake field acceleration: The highly non-linear broken-wave regime." In: Appl. Phys. B Lasers Opt. 74.4-5 (2002), pp. 355–361. ISSN: 09462171. DOI: 10.1007/s003400200795.

[141] S. C. Rae et al. "Possible production of cold plasmas through optical-field-induced ionization." In: Phys. Rev. A 46.4 (1992), pp. 2077–2083. ISSN: 10502947. DOI: 10.1103/PhysRevA.46.2077.

[142] M. Reiser et al. Theory and Design of Charged Particle Beams. Vol. 48. 6. 1995, pp. 59–59. DOI: 10.1063/1.2808068.

[143] J. B. Rosenzweig. "Trapping, thermal effects, and wave breaking in the nonlinear plasma wake-field accelerator." In: Phys. Rev. A 38.7 (1988), pp. 3634–3642. ISSN: 10502947. DOI: 10.1103/PhysRevA.38.3634.

[144] J. B. Rosenzweig. "Multiple-fluid models for plasma wake-field phenomena." In: Phys. Rev. A 40.9 (1989), pp. 5249–5255. ISSN: 10502947. DOI: 10.1103/PhysRevA.40.5249.

[145] J. B. Rosenzweig. Fundamentals of Beam Physics. Oxford University Press Oxford, 2010. DOI: 10.1093/acprof:oso/9780198525547.001.0001.

[146] J. B. Rosenzweig et al. "Experimental observation of plasma wake-field acceleration." In: Phys. Rev. Lett. 61.1 (1988), pp. 98–101. ISSN: 00319007. DOI: 10.1103/PhysRevLett.61.98.

[147] J. B. Rosenzweig et al. "Acceleration and focusing of electrons in two-dimensional nonlinear plasma wake fields." In: Phys. Rev. A 44.10 (1991). ISSN: 10502947. DOI: 10.1103/PhysRevA.44.R6189.

[148] J. B. Rosenzweig et al. "Energy loss of a high charge bunched electron beam in plasma: Simulations, scaling, and accelerating wakefields." In: Phys. Rev. Spec. Top. - Accel. Beams 7.6 (2004), pp. 71–81. ISSN: 10984402. DOI: 10.1103/PhysRevSTAB.7.061302.

[149] J. Rosenzweig. "Nonlinear plasma dynamics in the plasma wakefield accelerator." In: IEEE Trans. Plasma Sci. 15.2 (1987), pp. 186–191. ISSN: 19399375. DOI: 10.1109/TPS.1987.4316683.

[150] S. G. Rykovanov et al. "Virtual detector of synchrotron radiation (VDSR) - A C++ parallel code for particle tracking and radiation calculation." In: AIP Conf. Proc. 1507.December 2012 (2012), pp. 399–403. ISSN: 0094243X. DOI: 10.1063/1.4773729.

[151] P. San Miguel Claveria et al. "Betatron radiation and emittance growth in plasma wakefield accelerators." In: Philos. Trans. A. Math. Phys. Eng. Sci. 377.2151 (2019), p. 20180173. ISSN: 14712962. DOI: 10.1098/rsta.2018.0173.

[152] P. Scherkl. "High-brightness plasma-based Compton backscattering source for high energy physics." PhD thesis. University of Strathclyde, 2020.

[153] P. Scherkl et al. "Plasma-photonic spatiotemporal synchronization of relativistic electron and laser beams." In: arXiv (2019). arXiv: 1908.09263.

[154] K. Schmid et al. "Density-transition based electron injector for laser driven wakefield accelerators." In: Phys. Rev. Spec. Top. - Accel. Beams 13.9 (2010), pp. 1–5. ISSN: 10984402. DOI: 10.1103/PhysRevSTAB.13.091301.

[155] M. Schnell et al. "Optical control of hard X-ray polarization by electron injection in a laser wakefield accelerator." In: Nat. Commun. 4 (2013), pp. 8–13. ISSN: 20411723. DOI: 10.1038/ncomms3421.

[156] C. B. Schroeder et al. "Warm wave breaking of nonlinear plasma waves with arbitrary phase velocities." In: Phys. Rev. E - Stat. Nonlinear, Soft Matter Phys. 72.5 (2005), pp. 3–6. ISSN: 15393755. DOI: 10.1103/PhysRevE.72.055401.

[157] R. J. Shalloo et al. "Hydrodynamic optical-field-ionized plasma channels." In: Phys. Rev. E 97.5 (2018), pp. 1–9. ISSN: 24700053. DOI: 10.1103/PhysRevE.97.053203.

[158] Z. M. Sheng et al. "Relativistic wave breaking in warm plasmas." In: Phys. Plasmas 4.2 (1997), pp. 493–495. ISSN: 1070664X. DOI: 10.1063/1.872116.

[159] K. Shigemori et al. "Developing a Radiative Shock Experiment Relevant to Astrophysics." In: Astrophys. J. 533.2 (2000), pp. L159–L162. ISSN: 0004637X. DOI: 10.1086/312621.

[160] Z. Shimony et al. "Time-dependent ambipolar diffusion waves." In: Phys. Fluids 8.9 (1965), pp. 1704–1707. ISSN: 10706631. DOI: 10.1063/1.1761485.

[161] L. Spitzer et al. Physics of Fully Ionized Gases. Vol. 31. 11. Courier Corporation, 1963, pp. 890–891. DOI: 10.1119/1.1969155.

[162] P. Sprangle et al. "Nonlinear theory of intense laser-plasma interactions." In: Phys. Rev. Lett. 64.17 (1990), pp. 2011–2014. ISSN: 00319007. DOI: 10.1103/PhysRevLett.64.2011.

[163] J. Stohr. Linac coherent light source II (LCLS-II) conceptual design report. Tech. rep. SLAC National Accelerator Lab., Menlo Park, CA (United States), 2011. URL: https://www.osti.gov/servlets/purl/1029479/.

[164] D. Strickland et al. "Compression of amplified chirped optical pulses." In: Opt. Commun. 56.3 (1985), pp. 219–221. ISSN: 00304018. DOI: 10.1016/0030-4018(85)90120-8.

[165] G. Stupakov. "Short-range wakefields generated in the blowout regime of plasma-wakefield acceleration." In: Phys. Rev. Accel. beams 21.4 (2018), p. 041301. ISSN: 2469-9888. DOI: 10.1103/PhysRevAccelBeams.21.041301.

[166] H. Suk et al. "Plasma electron trapping and acceleration in a plasma wake field using a density transition." In: Phys. Rev. Lett. 86.6 (2001), pp. 1011–1014. ISSN: 00319007. DOI: 10.1103/PhysRevLett.86.1011.

[167] H. Suk et al. "Method of trapping accelerating electrons in plasma." In: US patent No. US7049736B2 (2003).

[168] O. Svelto. Principles of Lasers. 1998. ISBN: 9781441913012. DOI: 10.1007/978-1-4757-6266-2.

[169] K. K. Swanson et al. "Control of tunable, monoenergetic laser-plasma-accelerated electron beams using a shock-induced density downramp injector." In: Phys. Rev. Accel. Beams 20.5 (2017), pp. 1–6. ISSN: 24699888. DOI: 10.1103/PhysRevAccelBeams.20.051301.

[170] J. Thomas et al. "Non-linear theory of a cavitated plasma wake in a plasma channel for special applications and control." In: Phys. Plasmas 23.5 (2016). ISSN: 10897674. DOI: 10.1063/1.4948712.

[171] M. C. Thompson et al. "Plasma density transition trapping as a possible high-brightness electron beam source." In: Phys. Rev. Spec. Top. - Accel. Beams 7.1 (2004), pp. 7–16. ISSN: 10984402. DOI: 10.1103/PhysRevSTAB.7.011301.

[172] J. J. Thomson. " XL. Cathode Rays." In: London, Edinburgh, Dublin Philos. Mag. J. Sci. 44.269 (1897), pp. 293–316. ISSN: 1941-5982. DOI: 10.1080/14786449708621070.

[173] H. E. Tsai et al. "Control of quasi-monoenergetic electron beams from laser-plasma accelerators with adjustable shock density profile." In: Phys. Plasmas 25.4 (2018), p. 43107. ISSN: 10897674. DOI: 10.1063/1.5023694.

[174] M. Tzoufras et al. "Beam loading in the nonlinear regime of plasma-based acceleration." In: Phys. Rev. Lett. 101.14 (2008). ISSN: 00319007. DOI: 10.1103/PhysRevLett.101.145002.

[175] D. Ullmann et al. "All-optical density downramp injection in Electron-driven plasma wakefield accelerators." In: arXiv (2020). arXiv: 2007.12634.

[176] N. Vafaei-Najafabadi et al. "Beam loading by distributed injection of electrons in a plasma wakefield accelerator." In: Phys. Rev. Lett. 112.2 (2014), pp. 1–5. ISSN: 00319007. DOI: 10.1103/PhysRevLett.112.025001.

[177] N. Vafaei-Najafabadi et al. "Producing multi-coloured bunches through beam-induced ionization injection in plasma wakefield accelerator." In: Philos. Trans. R. Soc. A Math. Phys. Eng. Sci. 377.2151 (2019). ISSN: 1364503X. DOI: 10.1098/rsta.2018.0184.

[178] J. L. Vay. "Simulation of plasma accelerators with the particle-in-cell method." In: arXiv (2020), pp. 14–16. arXiv: 2008.07300.

[179] C. Wang et al. "Shock-wave-based density down ramp for electron injection." In: Phys. Rev. Spec. Top. - Accel. Beams 15.2 (2012), p. 20401. ISSN: 10984402. DOI: 10.1103/PhysRevSTAB.15.020401.

[180] A. M. Weiner. Ultrafast Optics. Wiley series in pure and applied optics. Hoboken, N.J.: Wiley, 2009, pp. 1–580. ISBN: 9780471415398. DOI: 10.1002/9780470473467.

[181] J. Wenz et al. "Physics of Laser-Wakefield Accelerators (LWFA)." In: arXiv Prepr. arXiv2007.04622 (2020).

[182] J. Wenz et al. "Dual-energy electron beams from a compact laser-driven accelerator." In: Nat. Photonics 13.4 (2019), pp. 263–269. DOI: 10.1038/s41566-019-0356-z.

[183] H. Wiedemann. Particle accelerator physics: Third edition. 3rd. ed. Berlin: Springer, 2007, pp. 1–948. ISBN: 9783540490432. DOI: 10.1007/978-3-540-49045-6.

[184] S. Wilks et al. "Beam Loading Efficiency in Plasma Accelerators." In: Part. Accel. 22 (1987), pp. 81–99.

[185] H. Winick. "Fourth generation light sources." In: Proc. IEEE Part. Accel. Conf. 1 (1998), pp. 37–41.

[186] G. Wittig. "Start to end simulations of hybrid laser- and beam-driven plasma wakefield acceleration and free electron lasers." PhD thesis. Universität Hamburg, 2017.

[187] G. Wittig et al. "Optical plasma torch electron bunch generation in plasma wakefield accelerators." In: Phys. Rev. Spec. Top. - Accel. Beams 18.8 (2015), pp. 1–6. ISSN: 10984402. DOI: 10.1103/PhysRevSTAB.18.081304.

[188] G. Wittig et al. "Electron beam manipulation, injection and acceleration in plasma wakefield accelerators by optically generated plasma density spikes." In: Nucl. Instruments Methods Phys. Res. Sect. A Accel. Spectrometers, Detect. Assoc. Equip. 829 (2016), pp. 83–87. ISSN: 01689002. DOI: 10.1016/j.nima.2016.02.027.

[189] L. Xiang et al. "X-ray acoustic computed tomography with pulsed x-ray beam from a medical linear accelerator." In: Med. Phys. 40.1 (2013), p. 10701. ISSN: 00942405. DOI: 10.1118/1.4771935.

[190] X. L. Xu et al. "High quality electron bunch generation using a longitudinal density-tailored plasma-based accelerator in the three-dimensional blowout regime." In: Phys. Rev. Accel. Beams 20.11 (2017), pp. 1–8. ISSN: 24699888. DOI: 10.1103/PhysRevAccelBeams.20.111303.

[191] V. Yakimenko et al. "FACET-II facility for advanced accelerator experimental tests." In: Phys. Rev. Accel. Beams 22.10 (2019), p. 101301. ISSN: 24699888. DOI: 10.1103/PhysRevAccelBeams.22.101301.

[192] X. Yan et al. "Subpicosecond electro-optic measurement of relativistic electron pulses." In: Phys. Rev. Lett. 85.16 (2000), pp. 3404–3407. ISSN: 00319007. DOI: 10.1103/PhysRevLett.85.3404.

[193] K. S. Yee. "Numerical Solution of Initial Boundary Value Problems Involving Maxwell's Equations in Isotropic Media." In: IEEE Trans. Antennas Propag. 14.3 (1966), pp. 302–307. ISSN: 15582221. DOI: 10.1109/TAP.1966.1138693.

[194] G. L. Yudin et al. "Nonadiabatic tunnel ionization: Looking inside a laser cycle." In: PHYS. REV. A - AT. MOL. OPT. PHYS. 64.1 (2001), p. 4. ISSN: 10941622. DOI: 10.1103/PhysRevA.64.013409.

[195] C. Zhang et al. "Effect of fluctuations in the down ramp plasma source profile on the emittance and current profile of the self-injected beam in a plasma wakefield accelerator." In: PHYS. REV. ACCEL. BEAMS 22.11 (2019), pp. 1–10. ISSN: 24699888. DOI: 10.1103/PhysRevAccelBeams.22.111301.